Lehrstuhl für Umformtechnik und Gießereiwesen
der Technischen Universität München

Improvement in Cold Formability of AZ31 Magnesium Alloy Sheets Processed by Equal Channel Angular Pressing (ECAP)

Joung Sik Suh

Vollständiger Abdruck der von der Fakultät für Maschinenwesen der Technischen Universität München zur Erlangung des akademischen Grades eines

Doktor-Ingenieurs (Dr.-Ing.)

genehmigten Dissertation.

Vorsitzender: Univ.-Prof. Dr.-Ing. Manfred Hajek

Prüfer der Dissertation:

1. Univ.-Prof. Dr.-Ing. Wolfram Volk
2. Univ.-Prof. Dr.-Ing. Dr.-Ing. E.h. A. Erman Tekkaya
   Technische Universität Dortmund

Die Dissertation wurde am 06.07.2015 bei der Technischen Universität München eingereicht und durch die Fakultät für Maschinenwesen am 19.11.2015 angenommen.

Danksagung / Vorwort

Die vorliegende Arbeit entstand während meiner Tätigkeit als wissenschaftlicher Assistent am Lehrstuhl für Umformtechnik und Gießereiwesen der Technischen Universität München.

Meinem Doktorvater Herrn Prof. Dr.-Ing. Wolfram Volk, Ordinarius für Umformtechnik und Gießereiwesen der Technischen Universität München, gilt mein Dank für das mir entgegengebrachte Vertrauen und die mir zugestandene Freiheit bei der Bearbeitung. Herrn Prof. Dr.-Ing. Dr.-Ing. E.h. A. Erman Tekkaya, Ordinarius für Umformtechnik und Leichtbau der Technischen Universität Dortmund, danke ich für die Übernahme des Koreferats. Mein Dank gilt in gleichem Maße Herrn Prof. Dr.-Ing. Manfred Hajek, Ordinarius für Hubschraubertechnologie der Technischen Universität München, für die Übernahme des Prüfungsvorsitzes.

Diese Dissertation basiert auf Ergebnissen des öffentlich geförderten Projektes „Gezielte prozesstechnische Optimierung der Textur zur Verbessrung der umformtechnischen und mechanischen Eigenschaften von Mg-Blechen“. Deutsche Forschungsgemeinschaft (DFG) sei für die finanzielle Unterstützung herzlich gedankt. Weiterhin bedanke ich mich bei den Herren Dr. Jose Victoria-Hernandez und Dr. Dietmar Letzig für die konstruktive und angenehme Zusammenarbeit.

Allen Mitarbeitern und Mitarbeitern des Lehrstuhls und Studenten danke ich für die fruchtbaren Diskussionen und die tatkräftige Unterstützung. Insbesondere seien hier Herr Hyunsuk Jung und Frau Annika Weinschenk genannt.

Mein besonderer Dank gilt meiner Familie, meiner Frau, meinen Kindern und meinen Freunden, deren gewährter Rückhalt entscheidend zur Fertigstellung der vorliegenden Arbeit beigetragen hat. Meinen Kindern ist die Arbeit gewidmet.

Garching, im Dezember 2015 Joung Sik Suh

Abstract (Deutsch)

Die vorliegende Arbeit trägt dazu bei, durch das Verfahren Equal Channel Angular Pressing (ECAP) die Kaltumformbarkeit und damit die Wettbewerbsfähigkeit des Magnesiumbleches AZ31 als Leichtbauwerkstoff zu steigern. Die systematische Parameteruntersuchung des ECAP-Verfahrens führt zu einem grundlegenden Verständnis der Wechselwirkungen zwischen Gefüge- und Texturänderung, Aktivierung der Deformationsmoden und daraus resultierenden mechanischen Eigenschaften von AZ31-Blechen. Auf dieser Basis werden die Grundlagen geschaffen, damit der ECAP-Prozess in Kombination mit konventionellen Walzverfahren zur Herstellung von Mg-Blechen mit verbesserter Kaltumformbarkeit eingesetzt werden kann.

Abstract (English)

The present study contributes to enhance the cold formability and competitiveness of magnesium sheet AZ31 as lightweight material using the process equal channel angular pressing (ECAP). The systematic parameter study of ECAP process leads to a fundamental understanding of the interactions between microstructure and texture evolution, activation of deformation mechanisms and mechanical properties of AZ31 sheets. On this basis, the fundamentals are established in order that ECAP process can be applied for the production of Mg sheets with enhanced cold formability in combination with conventional rolling processes.

Contents

Abbreviation

Symbol	***Unit***	***Description***
45°	*-*	*At the angle of 45° to the rolling direction*
a	*nm*	*Lattice parameter*
Al	*-*	*Aluminum*
ARB	*-*	*Accumulated roll-bonding*
bcc	*-*	*Body-centered cubic*
c	*nm*	*Lattice parameter*
c_p	*J/kgK*	*Specific heat capacity*
CFRP	*-*	*Carbon-fiber-reinforced plastic*
DSR	*-*	*Differential speed rolling*
d	*µm*	*Average grain size*
E	*GPa*	*Young's modulus*
ECAE	*-*	*Equal channel angular extrusion*
ECAP	*-*	*Equal channel angular pressing*
F_c	*N*	*Critical force*
fcc	*-*	*Face-centered cubic*
Fe	*-*	*Iron*
FLC	*-*	*Forming limit curve*
G	*GPa*	*Shear modulus*
h	*mm*	*Forming depth*
h_C	W/m^2K	*Heat transfer coefficient for conduction*
hcp	*-*	*Hexagonal close-packed*
HPT	*-*	*High-pressure torsion*
I	mm^4	*Area moment of inertia*
I_x	mm^4	*Area moment of inertia to the x-direction*
I_y	mm^4	*Area moment of inertia to the y-direction*
IPF	*-*	*Inverse pole figure*
K	*-*	*Effective length factor*
k_y	*MPa*	*Strengthening coefficient*
L_C	*mm*	*Unsupported length of column*
m	*-*	*Schmid factor*

m.r.d.	-	*Multiple random distribution*
Mg	-	*Magnesium*
N	-	*Number of the passes*
n-value	-	*Strain hardening exponent*
n_{RD}	-	*n-value in the rolling direciton*
n_{TD}	-	*n-value in the transverse direciton*
n_{45}		*n-value at the angle of 45° to the rolling direction*
$\bar{n}$	-	*Average n-value*
ND	-	*Normal direction*
P	-	*Pressing*
PD	-	*Pressing direction*
r-value	-	*Plastic anisotropy*
r_{RD}	-	*r-value in the rolling direction*
r_{TD}	-	*r-value in the transverse direction*
r_{10}	-	*r-value at engineering strain of 10%*
r_{45}		*r-value at the angel of 45° to the rolling direction*
$\bar{r}$	-	*Average r-value*
Δr	-	*Planar anisotropy*
RD	-	*Rolling direction*
RE	-	*Rare earth*
SPD	-	*Severe plastic deformation*
T	*°C*	*Processing temperature*
T_B	*°C*	*Boiling temperature*
T_M	*°C*	*Melting temperature*
t_R	*mm*	*Total length of reinforcement bar*
t_S	*mm*	*Thickness of stamp*
TD	-	*Transverse direction*
UTS	*MPa*	*Ultimate tensile strength*
YS	*MPa*	*Yield strength*
w	*mm*	*Measurment width of Nakajima specimen*
w_R	*mm*	*Width of reinforcement*
w_S	*mm*	*Width of stamp*
α	°	*Lattice parameter*

α_L	K^{-1}	*Thermal expansion coefficient*
$ß$	°	*Lattice parameter*
γ	°	*Lattice parameter*
γ_{xz}	-	*Shear strain*
$\bar{\varepsilon}_N$	-	*Effective strain after N passes*
ε_u	%	*Uniform strain*
ε_f	%	*Fracture strain*
ε_1	-	*Major strain*
ε_2	-	*Minor strain*
ζ	°	*Angle between slip direction and force direction*
Θ	MPa	*Work hardening rate*
θ	°	*Angular resolution*
λ	W/mK	*Thermal conductivity*
ν	-	*Poisson's ratio*
ξ	°	*Angle between slip plane and force direction*
ρ	g/cm^3	*Density*
σ	MPa	*Stress*
σ_y	MPa	*Yield stress*
σ_0	MPa	*Resistance of the lattice to dislocation motion*
$\sigma_{0.2}$	MPa	*0.2% proof stress*
τ	MPa	*Resolved shear stress*
Φ	°	*Channel angle*
Ψ	°	*Arc angle*

1 Introduction

1.1 Background and motivation

With increasing demand for lightweight construction, magnesium and its alloys have received renewed attention as the lightest metallic engineering material. The low density of Mg alloys provides high specific mechanical properties such as high specific strengths and buckling resistance compared to aluminum and steel (see Figure 1.1). These outstanding properties are of central importance particularly for applications in car body construction, where Mg alloys have to prevail against lightweight concepts with aluminum alloys (e.g. AA6016) as well as high strength steels (e.g. DP800) [NUER10]. Apart of high specific strength and stiffness, good castability and weldability have made Mg alloys attractive for further applications, e.g. aeronautics, electronics and household application [MORD01]. Another decisive advantage of Mg over carbon-fiber-reinforced plastic (CFRP) is its excellent recyclability. Magnesium can be reproduced and processed in high-purity quality. Recycling process requires only about 5% of the amount of energy for raw material extraction [KAMM00].

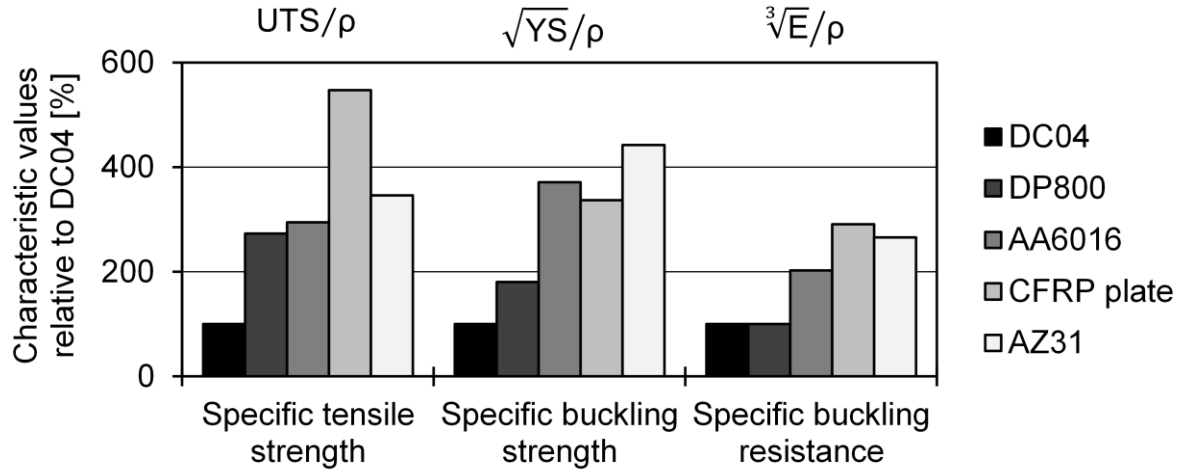

Figure 1.1: Specific characteristic values of aluminum alloy 6016, advanced high strength steel DP800, CFRP plate and magnesium alloy AZ31 in comparison with deep drawing steel DC04 [NUER10] (UTS: ultimate tensile strength, YS: yield strength, E: young's modulus, ρ: density)

Notwithstanding the lightweight potential, wrought Mg alloys play still a subordinate role in industrial application. The further processing to die cast products achieves high annual growth rates, and is therefore one of the main applications of Mg [KLEI02]. All

wrought Mg products still occupy less than 1% of primary Mg market [BENE08]. With special emphasis of Mg sheets, their poor formability, especially at room temperature, is one of the main reasons hindering industrial applications. Because of the limited formability, the forming process of Mg sheets are principally carried out at elevated temperature of above 200 °C. This is due to the hexagonal crystal structure and the limited number of active slip systems at room temperature [ROBE60]. Typical wrought Mg alloys such as Mg-Al-Zn system have a tendency to develop strong crystallographic texture during rolling [STYC04]. This texture is characterized by a preferred orientation of the basal planes in the sheet plane. The pronounced orientation of the basal planes limits the ability of basal <a> slip to accommodate plastic strain in the sheet plane [PART67]. This strong basal texture remains unchanged during the recrystallization annealing [HIRS13]. This results in low ductility and formability, especially at room temperature. Moreover, this pronounced texture leads to mechanical anisotropy.

Texture weakening/randomization and grain refinement can improve the forming characteristics of Mg alloy sheets [YI10]. The principal objective of texture modification in Mg is to attain a favorable alignment of the basal planes along the deformation direction. Grain refinement plays a role in reducing the activity of twinning and promoting additional deformation mechanisms, such as grain boundary sliding [HIRS13]. Consequently, this microstructural development can improve mechanical properties and forming behavior, especially at room temperature. There are some possibilities to influence microstructure development by means of new alloy systems [e.g. BOHL10] and thermo-mechanical treatments [e.g. WATA07].

With respect to thermo-mechanical treatments, equal channel angular pressing (ECAP) offers a distinct possibility to reduce grain size and generate unique textures. As a specimen is pressed through a tilted channel, it is primarily deformed by simple shear along the intersection plane between the entrance and exit channels [AGNE04]. Mukai et al. [MUKA01] showed a remarkably enhanced ductility of AZ31 alloy at room temperature using ECAP Jufu et al. [JUFU10] investigated the effect of processing routes, temperatures and the number of passes on room temperature mechanical properties of AZ91 alloy. Particularly, Lapovok et al. [LAPO08] applied ECAP process to 6111 Al alloy sheet regarding the effect of processing routes. However, the existing

studies on ECAP process with Mg alloys are still limited to bulk materials such as rectangular or circular bars with limited process conditions, e.g. a channel angle of 90°.

1.2 Objectives and tasks

The present study examined the possibility for the application of ECAP process to commercial AZ31 Mg sheets. This Mg sheet is most frequently used in industrial applications. Particularly, this alloy exhibits a distinct basal texture after rolling [STYC04]. For this reason, the effect of ECAP on the microstructural development and correlated mechanical properties can be easily detected and analyzed. The emphasis is on the systematic investigation of the process parameters (processing temperature, channel angle and processing route) and on the analysis of their mutual influences on the microstructure evolution and mechanical properties. These results associate directly with the cold formability of the equal channel angularly pressed (ECAPed) AZ31 sheets. In this respect, this study can provide possibility for industrial applications of Mg sheets with improved cold formability. Based on this, it is possible to apply ECAP process with conventional rolling process for the production of magnesium semi-finished products with enhanced cold formability (see Figure 1.2). Therefore, instead of warm forming, it enables cold forming of Mg sheets at competitive costs.

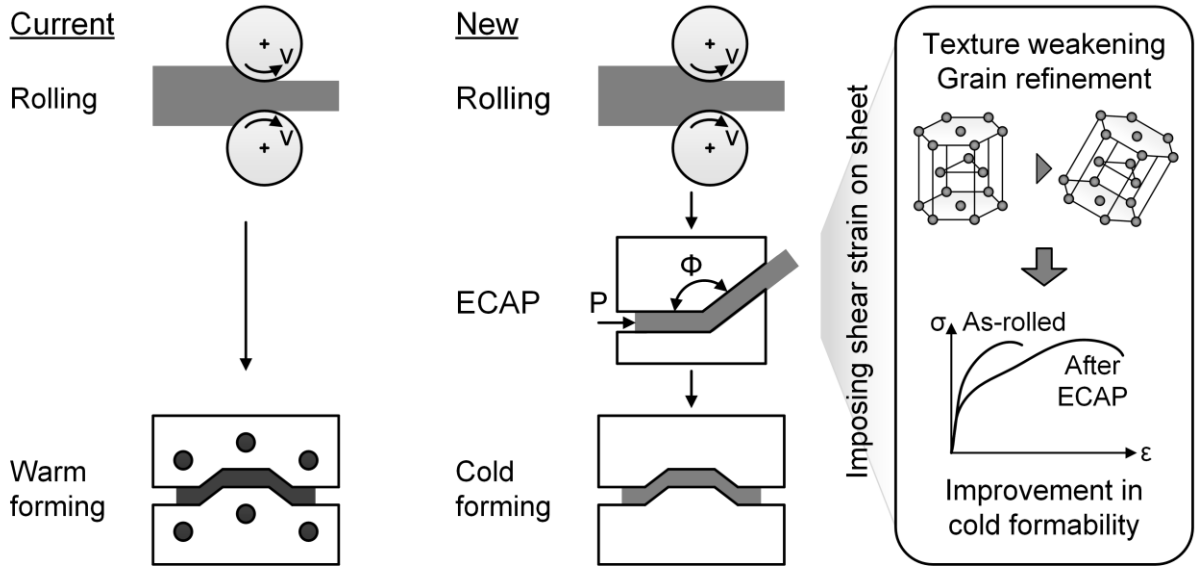

Figure 1.2: Application of ECAP to production of magnesium sheets with enhanced cold formability

The present study contributes to a basic understanding of the application of ECAP process to Mg sheets. The structured approach is schematically described in Figure 1.3. The present work focuses in detail on the following tasks:

- Design and construction of a modular trial tool for application of ECAP to sheet with dimensions of 200 × 200 × 1.8 mm^3 as well as change of channel angle
- Implementation of ECAP with different process parameters: processing temperature, channel angle, processing route
- Implementation of hot straightening for achievement of homogeneous microstructure and fully flat ECAPed AZ31 sheets
- Microstructural stability analysis at hot straightening in terms of annealing temperature and duration
- Microstructure analysis on grain refinement and texture variation using optical microscopy, electron backscatter diffraction (EBSD) and X-ray diffraction (XRD)
- Analysis of mechanical properties at room temperature with uniaxial tensile test regarding ductility and anisotropy
- Analysis of cold forming behavior using forming test of a U-shaped profile as well as using Nakajima test for determination of forming limit curves
- Investigation of Influences of process parameters on microstructure development and cold formability

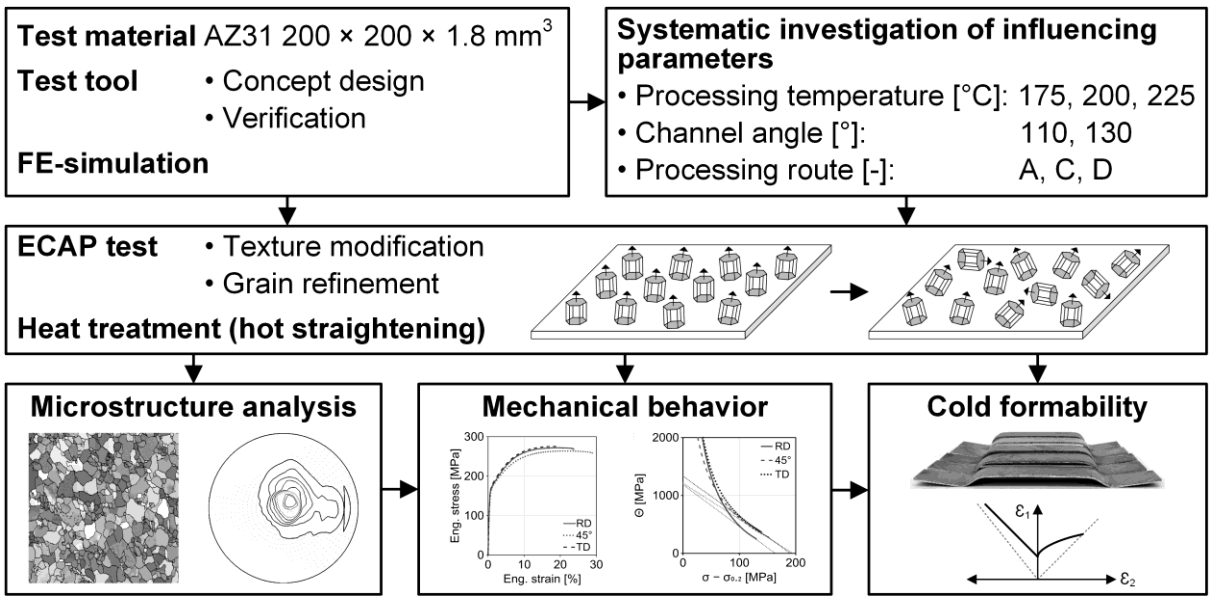

Figure 1.3: Schematic description of structured approach

2 State of the Art

2.1 Characteristics of Mg and its alloys

2.1.1 Magnesium as design material

2.1.1.1 Magnesium

Magnesium and its alloys crystallize in the hexagonal close-packed (hcp) structure as depicted in Figure 2.1. The basal plane forms the base surface of an equilateral hexagon with the edge length a. The hexagonal coordinate system consists of three equal long axes a_1, a_2, a_3 and c-axis, which is perpendicular to the basal plane. In the four-axis coordinate system, the planes are notated by Miller-Bravais index [MILL39, BRAV50]. In this system, crystallographic planes and directions are given by (h k i l) and [u v t w], where i = -(h + k). The unit cell exhibits the c/a ratio of $\sqrt{8/3} \approx 1.633$ with an ideal arrangement of the atoms [GOTT07]. The lattice parameters of pure magnesium at 25 °C are a = 0.32 nm and c = 0.52 nm, $\alpha = \beta = 90°$, $\gamma = 120°$. The c/a ratio of pure Mg (= 1.624) is very close to the ideal value. The c/a ratio is very important for hcp materials, because the activities of potential deformation modes, i.e. slip and twinning, are dependent on this value [YI05]. The influence of the c/a ratio on the activation of the deformation mechanisms is described in section 2.1.2.

Magnesium belongs to alkaline earth metals, which occupy the second main group of the periodic table of elements. Its hcp structure has significant influence on the physical properties, especially on the formability [NUER10]. Table 2.1 summarizes the main physical properties of pure magnesium, aluminum and iron as compared at 20 °C. As the lightest metallic material, the outstanding property of Mg is its low density of 1.74 g/cm^3, which makes an increasing demand for lightweight construction. It amounts less dense than two thirds of aluminum and less dense than one fourth of iron. Apart of the lowest density, the high specific strength and stiffness offer great potential for industrial application [KAMM00].

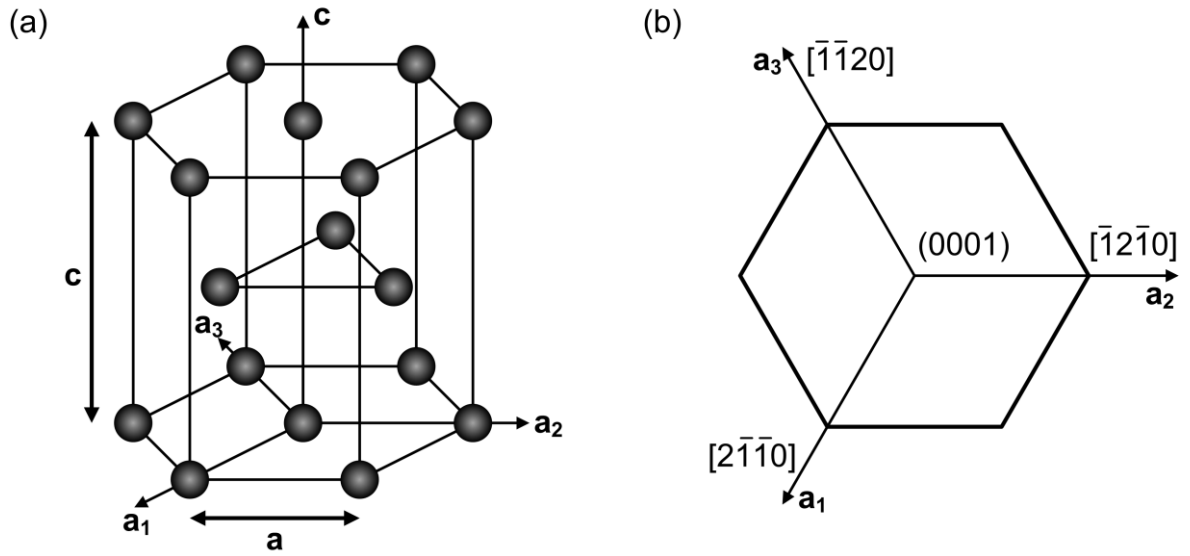

Figure 2.1: a) hexagonal close-packed (hcp) crystal structure; b) description of basal (0001) plane using Miller-Bravais index [STAR98]

	Mg	***Al***	***Fe***	***Unit***
Crystal structure	*hcp*	*fcc*	*bcc*	*-*
Crystal parameter	*a = 0.3203 c = 0.5199*	*a = 0.4047*	*a = 0.2867*	*nm*
Axial ratio c/a	*1.624*	*n.a.*	*n.a.*	*-*
Density ρ	*1.74*	*2.70*	*7.85*	*g/cm³*
Young's modulus E	*44.6*	*66.6*	*211*	*GPa*
Shear modulus G	*16.6*	*25.0*	*82*	*GPa*
Poisson's ratio v	*0.35*	*0.35*	*0.29*	*-*
Melting temperature T_M	*650*	*660*	*1538*	*°C*
Boiling temperature T_B	*1090*	*~2500*	*2862*	*°C*
Specific heat capacity c_p	*1025*	*900*	*449*	*J/kgK*
Thermal conductivity λ	*156*	*235*	*80*	*W/mK*
Thermal expansion coefficient α_L	*25×10^{-6}*	*23.6×10^{-6}*	*11.8×10^{-6}*	*K^{-1}*

Table 2.1: Physical properties of pure magnesium, aluminum and iron at 20 °C [KAMM00, KAMM02, CARD08]

2.1.1.2 Magnesium alloys

Magnesium must be alloyed with other metals for engineering applications [FRIE06]. Magnesium alloys are divided into cast alloys and wrought alloys in terms of the method used for component manufacturing [CZER08]. Both groups have subdivisions

indicating composition and application: where cast alloys are further divided into sand cast, permanent mold cast and die cast. Rolled, extruded and forged alloys belong to wrought alloys. Finally, depending on the service conditions, alloys are classified as general purpose, high ductility and high temperature grades [FRIE06, CZER08].

The amount of alloying element, which can be added to Mg, is controlled by the liquid solubility of the element in the molten state [XIAO13]. Magnesium alloys are normally designated by a four-part letter-number system according to ASTM B275-05. Each alloy is expressed with the two first letters indicating the principal alloying elements and the two next number specifying the rounded-off percentage of each weight (e.g. AZ31, 3% Al and 1% Zn, refer to Table 9.1).

Table 2.2 presents some representative wrought Mg alloys and their key characteristics. Wrought Mg alloys exhibit typically higher yield stress and elongation as compared with cast alloys [KAMM00]. The main alloying elements are aluminum, zinc and manganese. Since AZ31 alloy is the focus in this work, the discussion on the effects of two following elements is limited:

Aluminum

Aluminum is the most commonly used alloying element and forms the basis of the die casting alloys. Aluminum enhances the strength using mixed crystal formation as well as formation of intermetallic phase $Mg_{17}Al_{12}$ at below 120 °C [GEHR04]. Especially, the optimum combination of strength and ductility was observed at ~6% in weight. Nevertheless, one major disadvantage is that the creep resistance is limited due to poor thermal stability of the $Mg_{17}Al_{12}$ phase [FRIE06].

Zinc

Zinc is one of the commonest alloying additions. It is used in conjunction with aluminum, zirconium and rare earths [FRIE06]. Zinc improves also the castability like aluminum and is effective for the grain refinement. However, the addition of over 1.5% increases the tendency for the formation of a hot crack [GEHR04].

Alloy group	*Alloy grade*	*Key characteristics*
Mg-Mn	*M1*	*Wrought products with moderate mechanical properties, not heat treatable, mainly rolling*
Mg-Al-Zn	*AZ31*	*General purpose alloy with moderate strength*
Mg-Zn-Zr	*ZK60*	*Extruded products and press forgings with high strength and good ductility*
Mg-Zn-RE	*ZE10*	*Good strength properties, high temperature creep resistance and thermal stability [LUO95], for rolling*
Mg-Y-RE	*WE43*	*High temperature creep resistance up to 300 °C, long term exposure up to 200 °C*
Mg-Th-Zr	*HK31*	*Sheets and plates with excellent formability and high strength up to 315 °C*

Table 2.2: Classification and characteristics of typical wrought Mg alloys (all values in weight %) [CZER08]

2.1.1.3 Production of semi-finished products of wrought Mg alloys

For the production of plates or sheets of wrought Mg alloys, there are two different methods. In the conventional process chain, the material with the desired alloy composition is first cast in the form of slabs and then further processed. This method results in a poor cast structure and typical grain size is between 200 and 600 µm [ENSS01]. Hot rolling for fine-grained sheet with grain size of about 20 µm is usually carried out in the temperature range between 300 and 480 °C depending on the alloy and the pretreatment of the feedstock material. For example, Mg-Al alloys like AZ31 or AZ61 require an intensive homogenization treatment of up to 24 hours at 400 °C, in order to dissolve low melting intermetallic phases [FRIE06].

Twin-roll casting is an excellent method for the generation of fine-grained feedstock materials that can be subsequently warm rolled to thin sheets. Liquid magnesium solidifies as a thin strip between two water-cooled rollers. The strip exhibits a thickness of 2 to 10 mm [HADA13]. Then, it is rolled in different hot rolling steps to the final product. This method allows a saving of up to two thirds of the rolling passes, and thus a reduction in the manufacturing costs of up to 60% [WATA04-1].

After the hot rolling, microstructural analyses show a pronounced basal texture, which remains nearly unaffected by further heat treatment. The grain orientation parallel to

the sheet plane is less extensive transversally to the rolling direction and attenuates towards the center of the sheet [ROBE60].

2.1.2 Deformation mechanisms in Mg alloys

Magnesium with a hexagonal structure, contrary to metals with cubic crystal structures, exhibits insufficient independent slip systems [YI05]. Since basal slip provides only two independent systems at room temperature, the activation of non-basal slips and twinning plays an important role in determining ductility and formability [ROBE60]. The activation of non-basal systems is strongly influenced by the texture developed after any thermo-mechanical process, and it is directly related to the mechanical anisotropy [YI05]. In this section, the deformation modes in Mg will be described in detail.

2.1.2.1 Slip systems

The plastic deformation of metallic materials can be realized by the activation of slip systems. One slip system consists of slip plane (densely packed plane) and slip plane (densely packed direction) [HUPP11]. The activation of the slip systems is not directly determined by an applied external stress, but by a resolved shear stress (RSS) acting along slip direction. The activation of a certain slip system depends on the critical resolved shear stress (CRSS) on the slip plane and in the slip direction [GOTT07]. Figure 2.2 describes the relationship between external stress and resolved shear stress. From the geometric relationship, resolved shear stress and Schmid factor are given by

$$\tau = \sigma \cos\zeta \cos\xi = m\sigma \tag{2.1}$$

where τ is the resolved shear stress, σ is the external stress, ζ is the angle between the slip direction and the direction of the applied force, ξ is the angle between the normal of the slip plane and the applied load direction. The Schmid factor m is given by $\cos\zeta \cos\xi$.

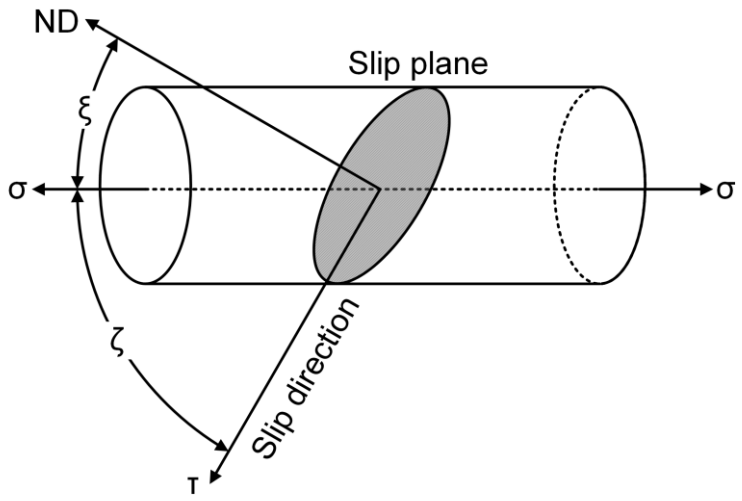

Figure 2.2: Schematic description of the relationship between external stress and resolved shear stress for determination of Schmid factor [GOTT07]

The RSS is dependent on orientation and it is associated to external stress by Schmid factor, chemical composition and deformation conditions [XIAO13]. Crystallographic planes rotate during plastic deformation. Consequently, the Schmid factor and the RSS change continuously. However, the CRSS for a specific slip system keeps constant according to the Schmid's law [SCHM35].

The low formability of Mg alloys at room temperature is due to the limited number of independent slip systems in the hcp crystal structure [ROBE60]. According to the von Mises criterion [MISE28], a polycrystalline material requires at least five independent slip systems for a general homogeneous deformation without cracks. At room temperature, metals with cubic crystal structures contain twelve slip systems of which five are independent. On the other hand, the hcp structure has only three slip systems of which two are independent. Hence, it is much easier to deform aluminum rather than magnesium due to the amount of active slip systems at room temperature [XIAO13]. Table 2.3 summarizes the fundamental slip systems in Mg regarding slip planes and directions. The (0001) plane is known as basal plane. Prismatic planes have the type of {1100} (type Ⅰ) and of {1210} (type Ⅱ). Planes of {hkil}, in case of $l \neq 0$, are known as pyramidal planes, {110l} (type Ⅰ) and {121l} (type Ⅱ) [YI05]. These slip systems are illustrated schematically in Figure 2.3.

			Number of slip systems	
Slip system	**Slip plane**	**Slip direction**	**Total**	**Independent**
Basal <a>	*(0001)*	*<11$\bar{2}$0>*	*3*	*2*
Prismatic <a>	*{10$\bar{1}$0}*	*<11$\bar{2}$0>*	*3*	*2*
Prismatic <c>	*{10$\bar{1}$0}*	*<0001>*	*3*	*2*
Prismatic <c>	*{11$\bar{2}$0}*	*<0001>*	*3*	*2*
Pyramidal <a>	*{10$\bar{1}$1}*	*<11$\bar{2}$0>*	*6*	*4*
Pyramidal <c+a>	*{11$\bar{2}$2}*	*<11$\bar{2}$3>*	*6*	*5*
Twinning <c+a>	*{10$\bar{1}$2}*	*<10$\bar{1}$1>*	*N/A*	*N/A*

Table 2.3: Most frequently encountered slip and twinning systems in Mg [PART67]

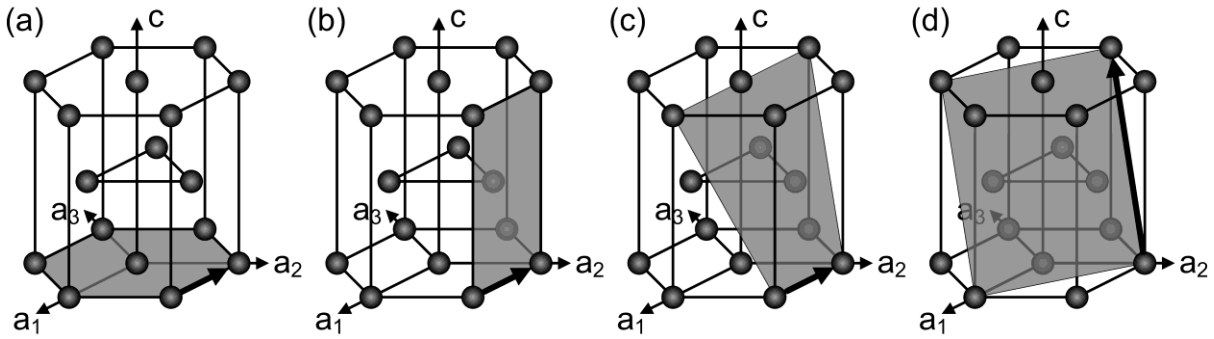

Figure 2.3: Possible slip systems in Mg alloys: (a) basal <a> slip, (b) prismatic <a> slip, (c) pyramidal <a> slip, (d) pyramidal <c+a> slip [PARA67, YOO81]

In general, there are several factors affecting the deformation modes and the operation of the slip systems in Mg: von Mises criterion, Schmid factor, CRSS and temperature dependence of CRSS [PART42]. Basal <a> slip, prismatic <a> slip and pyramidal <a> slip provide only four independent slip systems. Pyramidal <c+a> slip, which provides the additional independent slip systems, is difficult to be activated at room temperature because of its high CRSS [YOO02]. These slip systems do not fulfill the von Mises criterion. From the energetic point of view in perfect dislocations, the <a> dislocations are the most favorable, and the <c+a> dislocations are the most unfavorable with the longest Burgers vector [YI05]. Hence, the dominant slip system of Mg and its alloys at room temperature is slip in the direction <11$\bar{2}$0> or <a> on the basal (0001) plane as depicted in Figure 2.3 (a) [ROBE60]. The CRSS of basal slip in pure Mg is about 0.5 MPa [BURK52].

At elevated temperature, the activation of pyramidal <c+a> slip and other non-basal slip occurs at lower CRSS, reducing flow stress and increasing formability [AGNE05-1]. Figure 2.4 describes the temperature dependency of the CRSS of the main deformation modes in AZ31 Mg alloy. Because of the high CRSS for <c+a> slip, the activation of twinning has been known as the main mechanism for accommodating the deformation along c-axis at low temperature [KOCK67]. Increase in the deformation temperature, decrease in the axial ratio of the hcp structure or ultra-grain refinement for grain boundary sliding enables the activation of non-basal slip and other deformation modes [XIAO13].

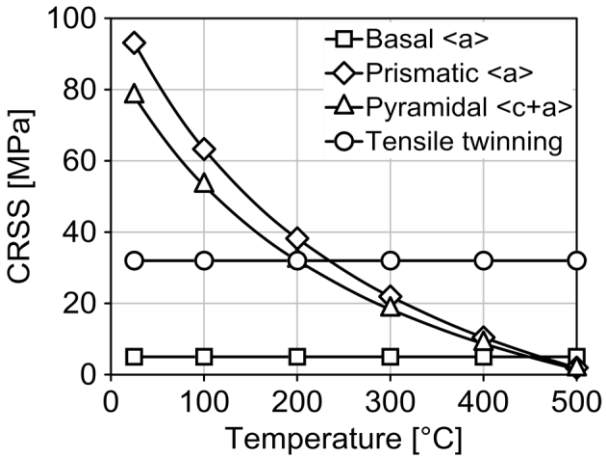

Figure 2.4: CRSS of variable slip systems depending on temperature in an extruded AZ31 alloy according to the model determined from experiments [BARN03]

2.1.2.2 Twinning systems

Magnesium exhibits a strong propensity for mechanical twinning [ROBE60]. At room temperature, twinning can provide an independent deformation mechanism to satisfy the von Mises criterion [KOCK67]. In comparison with dislocation slip, mechanical twinning is characterized as follows [YOO81]:

- Twinning is a polar mechanism, which allows simple shear only in one direction
- The amount of plastic shear by twinning is small and limited
- Twinning causes suddenly large orientation change of crystal, which is different from the gradual orientation change observed in dislocation slip

Although twinning has a limited contribution to plastic shear, twinning plays an important role in the rotation of unfavorably oriented crystals to favorable direction for dislocation slip. In this way, this activated dislocation slip can contribute to further deformation [YI05]. Moreover, twinning can produce atomic movements in a manner such that atoms on one side of a plane are located in symmetry positions of atoms on the other side as illustrated in Figure 2.5 (a). This manner is the typical twinning deformation in Mg [GOTT07]. Table 2.4 summarizes the twinning modes observed frequently in Mg and its alloys. Three types of twins are $\{10\bar{1}2\}\langle 10\bar{1}1\rangle$ tension twin, $\{10\bar{1}1\}\langle 10\bar{1}2\rangle$ compression twin and $\{10\bar{1}1\}$-$\{10\bar{1}2\}$ double twin. In hcp crystals, the twinning systems are strongly correlated with the c/a ratio [PART67]. At an extension along the c-axis in Mg, $\{10\bar{1}2\}$ tension twins can be activated due to $c/a < \sqrt{3}$ [YOO81]. During twinning, the basal plane is reoriented by 86.3° as depicted in Figure 2.5 (b) and (c) [PART67]. This twinning mode is the most common and easily activated twin in Mg and many other hcp metals [ROBE60]. Because of the polar nature of twinning, the shear can occur only in one direction rather than opposite directions [KOCK67]. Therefore, a contraction along the c-axis cannot be accommodated by $\{10\bar{1}2\}$ twin. In Mg, a theoretical maximum extension of 6.4% along the c-axis can be accommodated by complete reorientation of $\{10\bar{1}2\}$ tension twins [KOCK67]. After twinning, the c-axis will reorient to position approximately in the original basal plane [NAVE04].

Rolled AZ31 alloy sheets exhibit very strong basal texture generated by rolling [ROBE60], where the c-axis of hcp lattice is predominantly aligned perpendicular to the sheet plane [YUKU03]. On the one hand, a tension in the sheet normal direction will activate twinning at low stress. On the other hand, a compression normal to the sheet plane does not activate twinning [KOCK67]. Conversely, an in-plane compression activates twinning, but in-plane extension does not [REED60]. Local inhomogeneity from grain-to-grain interactions can activate limited twinning, particularly in view of the limited number of independent slip systems. This enables the rotations of some grains that do not locate in the predominant basal texture [LOU07].

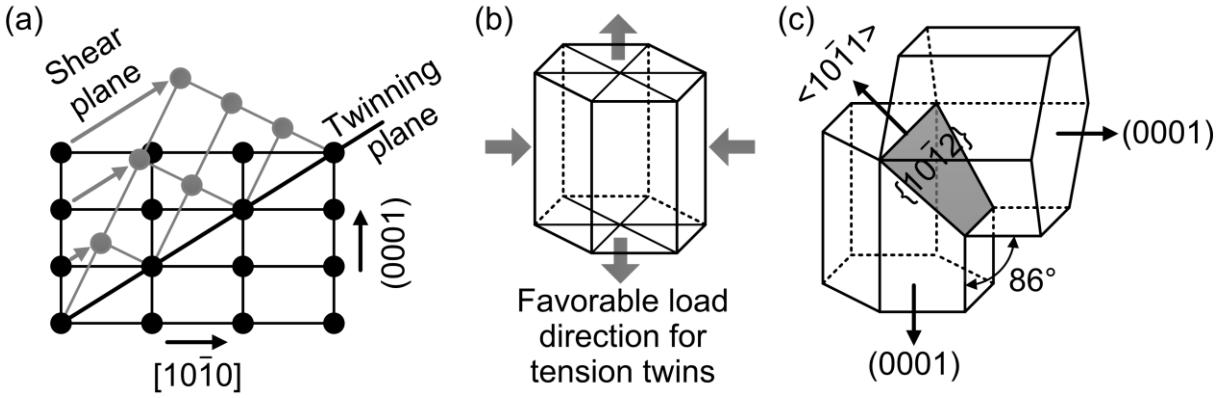

Figure 2.5: *(a) twinning in hexagonal crystal with c/a < $\sqrt{3}$ such as Mg [GOTT07], (b) favorable loading direction with respect to c-axis for activation of {10$\bar{1}$2} <10$\bar{1}$1> tension twins [YOO81], (c) schematic of reorientation of hexagonal unit cell by formation of {10$\bar{1}$2} <10$\bar{1}$1> tension twin [PART67]*

	Twinning plane	***Twinning shear direction***	***Orientation angle***	***Activation load parallel to C-axis***
Tension twin	*{10$\bar{1}$2}*	*<10$\bar{1}$1>*	*86°*	*Tension*
Compression twin	*{10$\bar{1}$1}*	*<10$\bar{1}$2>*	*56°*	*Compression*
Double twin	*{10$\bar{1}$1}-{10$\bar{1}$2}*	*<10$\bar{1}$2>-<10$\bar{1}$1>*	*38°*	*Compression*

Table 2.4: *Commonly observed twinning systems in Mg alloys [YOO81, NAVE04]*

2.1.3 Texture development in Mg and its alloys

2.1.3.1 General description of texture

Metallic materials are polycrystalline consisting of aggregates of single crystals [YI05]. As each single crystal aligns in similar or identical crystallographic orientation, the preferred orientation of crystalline material is referred as texture [WASS62]. A texture can form and change during thermo-mechanical treatments [KAIS05]. A strong texture is one where the crystals are predominantly oriented in one direction. Otherwise, a weak texture is one with crystals oriented in statistically random direction. The material properties such as anisotropy is directly correlated with the preferred alignment of the crystallites in certain sample direction [YI05].

The texture is represented as the orientation distribution of crystallites with respect to a given sample coordinate system. In the sample coordinate system, e.g. normal, roll-

ing and transverse direction (ND, RD and TD) for rolled sheet, the secondary coordinate system is defined in the crystal axes following the crystal symmetry, e.g. (0001), $(2\bar{1}\bar{1}0)$ and $(10\bar{1}1)$ for hexagonal structure. The orientation distribution in the texture is calculated from measured pole density distribution functions. This calculation process is called as the pole figure inversion [YI05].

Figure 2.6 illustrates the basic concept for pole figure, which represents the probability of the distribution of crystals in an arbitrary sample direction. In Figure 2.6 (a), a point on the surface of the reference sphere is connected to the South Pole and defined on the projection plane by the intersection line. This method is called as stereographic projection. If the (0001) planes are oriented parallel to sample normal plane, the (0001) pole figures appear in the center of the pole figure as illustrated in Figure 2.6 (b). The pole density (or intensity) is presented generally as contour lines as shown in Figure 2.6 (c) [YI05]. Pole figures can be measured by various diffraction techniques such as X-ray diffraction (XRD) and electron backscatter diffraction (EBSD).

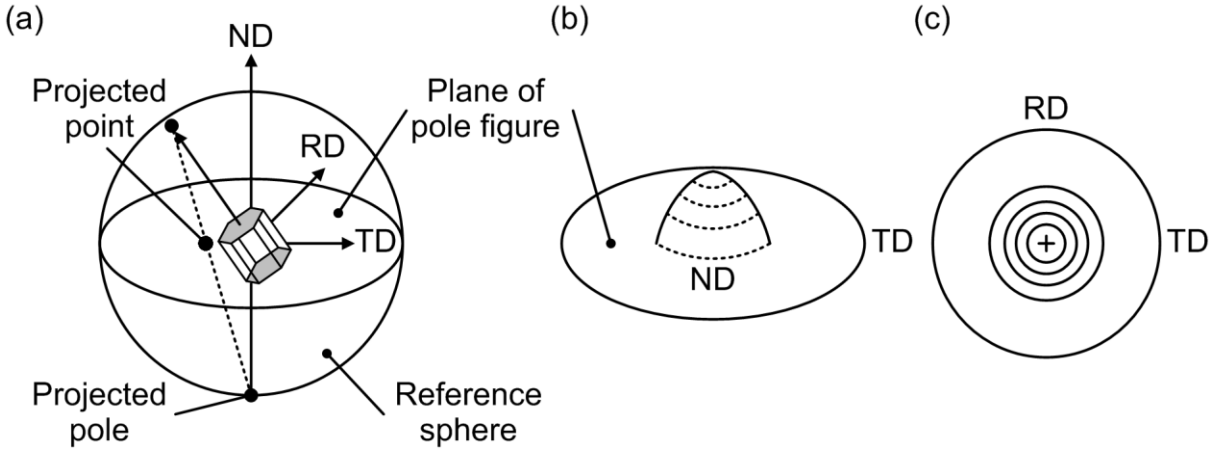

Figure 2.6: Schematic representation of basic concepts for pole figure: (a) principle of stereographic projection [NUER10], (b) pole density (intensity) distribution on the projection plane, (c) its contour plot [YI05]

2.1.3.2 Texture development in Mg

Formation of different types of textures in hexagonal metals, especially Mg, depends on alloying elements, temperature and deformation methods. In case that the c/a ratio is almost equal to the ideal value such as Mg, the textures are developed with a tendency of basal texture as depicted in Figure 2.7 (a). The (0001) pole figure of AZ31

sheet has a maximum pole intensity (I_{max}) of 15, which is much stronger than that of ZE10 sheet with I_{max} = 4. The pole figure of AZ31 sheet shows that most grains align parallel to the ND, which corresponds to a so-called basal type texture [YI10]. In contrast to AZ31, ZE10 sheet shows a broader intensity distribution of the basal poles towards the TD than to the RD. Furthermore, the rotation of the basal poles by 20-30° along the TD is observed, which does not occur in AZ31.

From EBSD measurements of the rolled AZ31 and ZE10 sheets, Figure 2.7 (b) shows the so-called inverse pole figure (IPF) map, in which the colors correspond to the crystal orientations coinciding more or less with the crystallographic axes, (0001), $(2\bar{1}\bar{1}0)$ and $(10\bar{1}1)$. The IPF provides information on how a selected direction is distributed parallel to the crystal axes in the specimen, while pole figure is essentially the projection of crystallographic directions in the sample frame of reference. For this reason, the IPF is referred to as the axis distribution charts, and hence it can help to visualize certain types of textures [SUWA14].

Based on this, Figure 2.7 (b) depicts that most grains have the (0001) axis parallel to the sample normal direction, since most grains show red coinciding with the (0001) axis. In this way, AZ31 sheet exhibits a pronounced basal texture with the strongly preferred orientation. The development of this texture was frequently observed in various Mg alloys, e.g. in AZ31 after hot and cold rolling [STYC04, KAIS05], in AZ61 after hot rolling and annealing [PERE04], in AZ80 after hot extrusion [WAGN03]. On the other hand, the IPF map of ZE10 sheet shows a more randomized texture formation. The existing studies have reported that additions of rare earth (RE) elements to Mg alloys develop weaker and more random texture during hot extrusion [BALL94] and hot rolling [BOHL07].

A new texture component, in which the basal poles align in the RD, appears with increasing the cold rolling degree [PHIL94]. The formation of this texture component is due to the activation of $\{10\bar{1}2\}$ tensile twinning. Furthermore, the splitting of basal poles along the RD in the (0001) pole figure has been observed after hot forming of AZ31 [AGNE03] and AM60 [PERE04].

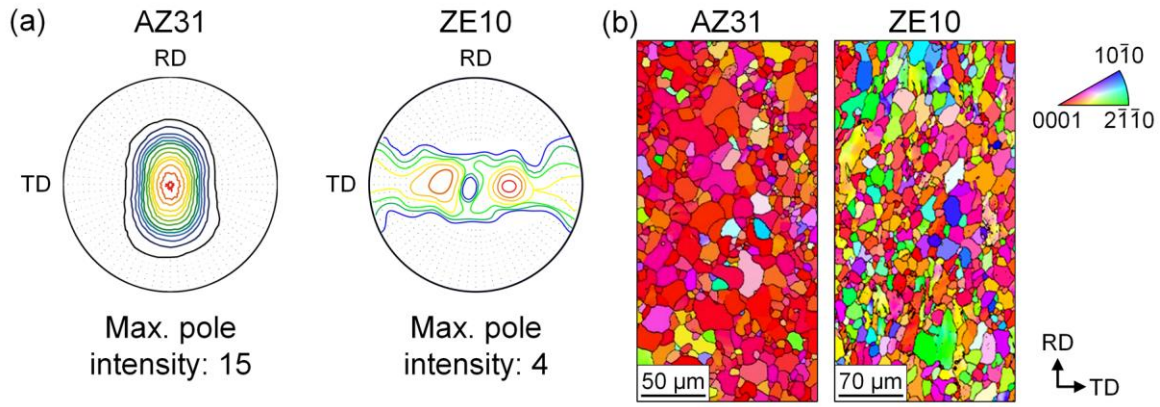

Figure 2.7: Comparison of texture development of AZ31 and ZE10 sheets: (a) (0001) pole figure, (b) inverse pole figure (IPF) map

2.1.4 Factors influencing mechanical and forming behavior

Type and number of active deformation modes relate closely to alloying elements, deformation parameter as well as stress conditions. This has a strong influence on the texture development. With a fundamental understanding of the effect of these parameters, it is possible to obtain desired texture type and mechanical properties [YI05]. In this section, the effects of initial texture, grain size and deformation temperature on mechanical properties are described in detail.

2.1.4.1 Initial texture and anisotropy

The initial texture is one of the most important factors, which has a remarkable effect on the forming properties of Mg alloys. Especially at sheet metals, forming process or grain growth (i.e. recovery and recrystallization) causes the generation and change of a texture [KAIS05]. Typical Mg alloy sheets exhibit strong basal-type textures with grain orientations, where the basal planes are predominantly aligned parallel to the sheet plane [ROBE60]. Basal, prismatic and pyramidal <a> slip systems fail to accommodate any deformation under loading in directions either parallel or perpendicular to the sheet plane [HIRS13]. The reason is that they have a slip direction parallel to the basal plane, and hence the resulting shear strain in all slip systems is almost zero [HIRS13]. In addition, strong basal texture restricts the activation of {10$\bar{1}$2} twinning, because {10$\bar{1}$2} twinning occurs under tension parallel to the c-axis or under compression perpendicular to the c-axis [WU11]. The twinning with its unidirectional feature contributes to the

anisotropic mechanical properties [YI05]. This leads to the low formability at room temperature in Mg alloy sheets.

Figure 2.8 (a) shows the typical pronounced basal texture of AZ31 sheet. Here a broader intensity of the basal poles spreads from the ND to the RD than to the TD [YI10]. This type of texture has been often referred as the typical texture of rolled or tempered Mg alloy sheets [AGNE01]. Such a texture develops during static recrystallization of strain hardened AZ31 sheets [KAIS03]. They show symmetrical splitting of the basal poles along the RD due to high activation of pyramidal <c+a> slip during rolling [AGNE01]. Consequently, this pronounced basal texture leads to a mechanical anisotropy, e.g. a distinct tension-compression asymmetry in stress-strain curves as presented in Figure 2.8 (b).

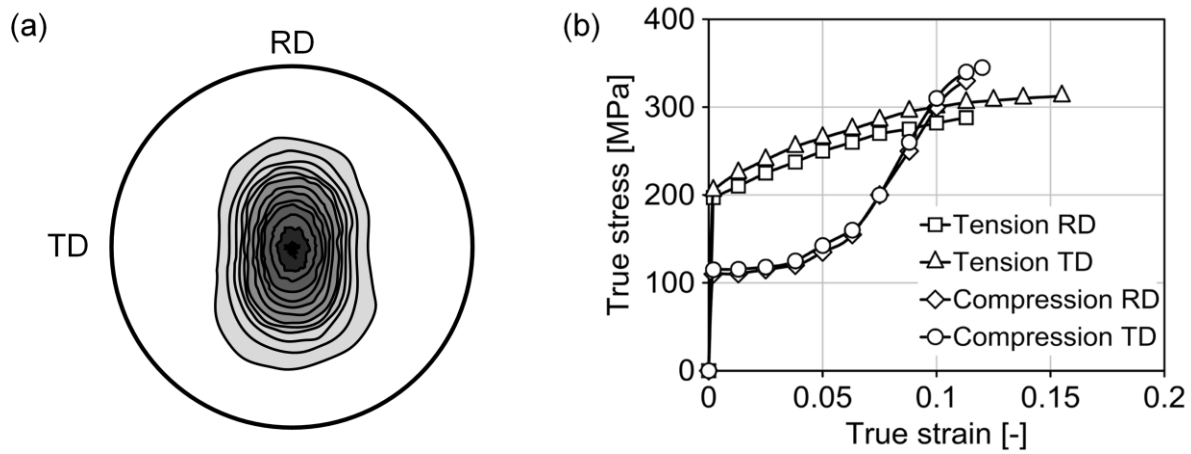

Figure 2.8: *(a) (0001) pole figure of AZ31 sheet [NUER10], (b) tension-compression asymmetry of stress-strain curves of AZ31 sheet [NGUY14]*

Alloy	***Tensile direction***	***YS[MPa]***	***UTS [MPa]***	***ε_f [%]***	***r-value [-]***
AZ31	*RD*	*163*	*263*	*16*	*1.92*
	45°	*175*	*263*	*19*	*2.11*
	TD	*186*	*275*	*17*	*2.92*
ZE10	*RD*	*143*	*228*	*16*	*0.93*
	45°	*120*	*221*	*22*	*1.23*
	TD	*110*	*220*	*18*	*0.85*

Table 2.5: *Tensile properties of AZ31 and ZE10 sheets in different loading directions [YI10]*

AZ31 sheet shows high in-plane mechanical anisotropy regarding yield strength (YS), fracture elongation (ε_f) and plastic strain ratio (r-value) as given in Table 2.5. The YS and r-value of AZ31 sheet increase gradually from the RD to the TD. As described in Figure 2.7 above, a larger tilt angle to the RD facilitates the activation of <a> dislocation slip during loading in this direction compared to the TD [YI10]. By contrast, the texture in ZE10 sheet is beneficial for higher activation of basal slip during loading in the TD than in the RD [BOHL07]. This causes a different mechanical anisotropy compared to conventional Mg alloy. In ZE10 sheet, the YS is highest in the RD and decreases towards the TD. The ε_f is lowest in the RD. The r-value at 45° to the RD (45°) is higher than in the RD and TD. Particularly, the r-values close to 1 indicate an isotropic contraction of the cross-section. The variation of r-value in different loading directions has a strong relationship with the texture [YI10].

For sheet metal forming (e.g. deep drawing and stretch forming), the average r-value ($\bar{r}$) and the planar anisotropy (Δr) are key characteristics. In general, high $\bar{r}$ leads to high limiting drawing ratio. The Δr indicates the strain distribution in the sheet plane and shows a tendency of earing behavior at deep-drawn cups [HOSF07]. If $\Delta r < 0$, the earing formation is predicted at 45° to the RD. If $\Delta r > 0$, earing is formed in the TD [LANG90]. Both factors are commonly expressed as [ISO 10113]:

$$\bar{r} = \frac{(r_{RD} + 2r_{45°} + r_{TD})}{4} \tag{2.2}$$

$$\Delta r = \frac{(r_{RD} - 2r_{45°} + r_{TD})}{2} \tag{2.3}$$

From Table 2.5, the $\bar{r}$ of ZE10 sheet (1.06) is twice lower than that of AZ31 sheet (2.27). However, ZE10 sheet exhibits better drawability at lower temperatures than AZ31 sheet [YI10]. The reason is that thickness strains can be easily accommodated by basal <a> slip. With respect to earing behavior, the Δr for AZ31 and ZE10 sheet is 0.31 and -0.34, respectively. Although the absolute value is comparable, earing formation at 45° is correlated with a negative Δr in ZE10. On the other hand, drawn AZ31 cups show almost negligible earing. Generally, $\bar{r}$ becomes larger, when alloy has

stronger basal pole density. Δr is higher, when alloy exhibits more orthotropic basal texture with an oval or elliptical shaped distribution [SUH14].

Strain hardening (or work hardening) is one of the most important factors, which controls a metal's resistance to plastic instability (and sheet formability) [AGNE05-1]. A higher strain-hardening exponent (n-value) leads to larger deformation without necking [OSTE07]. This effect is especially beneficial for stretch formability in terms of the average n-value ($\bar{n}$), which is calculated similarly to the $\bar{r}$ [DOEG88] (refer to Equation 2.4). Conventional metal sheets with good formability have n-values of 0.2-0.5 at room temperature [AGNE05-1]. On the other hand, the n-values of most Mg alloys are lower than 0.2. For example, the n-value of AZ31 and AM30 alloy sheets is 0.14 and 0.17, respectively [LUO07].

$$\bar{n} = \frac{(n_{RD} + 2n_{45°} + n_{TD})}{4} \tag{2.4}$$

Detailed studies on work hardening behaviors of single crystals of pure Mg were performed before 1980 [HIRS65]. The work hardening behavior is analyzed by the macroscopic work hardening rate Θ:

$$\Theta = \frac{d\sigma}{d\varepsilon_p} \tag{2.5}$$

where σ and ε_p are true stress and true plastic strain, respectively. In hexagonal metals, three work hardening stage are observed as in face-centered cubic (fcc) crystals [SCHM35]. Stage I is an initial transient stage, where Θ decreases rapidly. In stage II, Θ increases to a maximum and then keeps nearly constant with σ. In stage III, Θ decreases linearly with σ due to the onset of dynamic recovery (refer to Figure 2.9 (a)). Since Θ keeps nearly constant with increasing σ at stage II, this linear hardening is responsible for tensile mechanical stabilities and high uniform elongation.

In the case of Mg alloy polycrystals, texture has a great influence on strain hardening [WU12]. Rolled samples with basal texture exhibit a suppression of stage II and a development of a linear stage III from the beginning of deformation by the enforcement

of prismatic <a> slip [VALL06]. Texture also has an influence on dynamic recovery that is related to the slope of the work hardening rate-true stress (Θ-σ) plots during stage III [VALL06]. Figure 2.9 (b) shows the influence of (0001) pole density on the Θ of AZ31 sheets [GUO11]. The amount of the Θ is reduced, as maximal pole density becomes lower. Lower pole density leads to relative slow transition to stage III and lower slope of dynamic recovery at stage III.

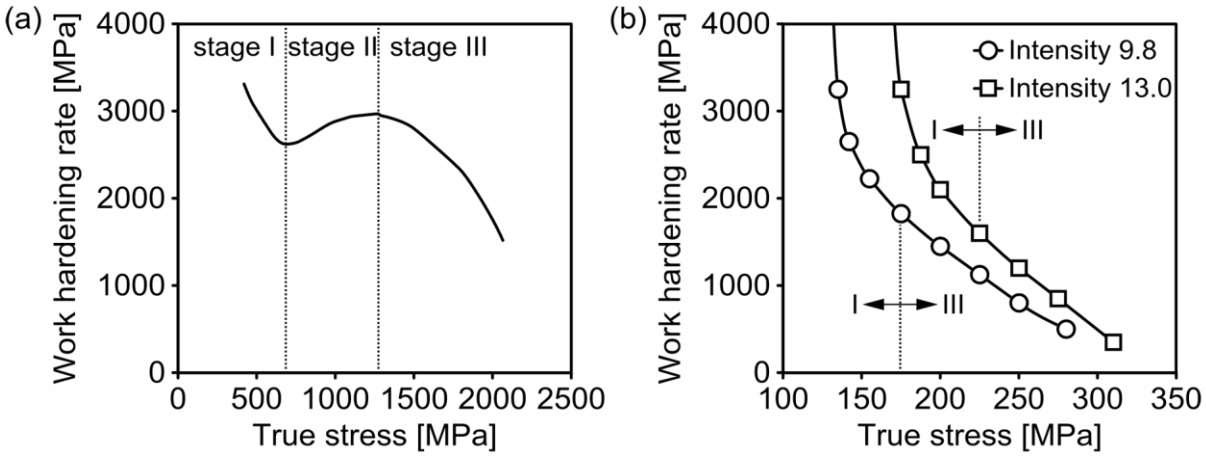

Figure 2.9: *(a) work hardening rate as a function of true stress in TWIP steel [RENA12], (b) influence of basal texture intensity on work hardening behavior of AZ31 alloy sheets [GUO11]*

2.1.4.2 Grain size

The average grain size of the material generally plays a dominant role in determining mechanical properties of all crystalline materials [VALI06]. The CRSS for slip and twinning systems exhibits a dependence of grain size according to the Hall-Petch equation [HALL51, PETC53]. It describes the dependence of the yield stress (σ_y) on the average grain size (d), which is given by

$$\sigma_y = \sigma_0 + k_y d^{-1/2} \tag{2.6}$$

where σ_0 is frictional stress resisting dislocation movement, k_y is the strengthening coefficient. The yielding occurs, when dislocation pile-up exerts sufficient stress at the grain boundary so that the slip band can propagate from one grain to the next [ARMS62]. Table 2.6 lists the Hall-Petch parameters for AZ31, pure Al and mild steel, which were derived by best fit to the experimental data.

Alloy	*d [µm]*	*σ_0 [MPa]*	*k_y [MPa·µm$^{1/2}$]*
Hot rolled AZ31 [ONO03]	*16-35*	*70*	*348*
Hot extruded AZ31 [WANG06]	*2.5-80*	*80*	*303*
ECAPed AZ31 [KIM05]	*2-8*	*30*	*180*
Pure Al [HORN93, EMBU89]	*1.5*	*16*	*65*
Mild steel [LIU03]	*30*	*272*	*237*

Table 2.6: Hall-Petch parameters of several materials in tension at room temperature

The existing studies showed that the constant for slip systems are three times higher than that for twinning [MEYE01, BARN04]. That is, twinning occurs with increasing grain size easier as compared to the dislocation slip. It has been shown that a transition from twinning- to slip-dominated flow occurs in compression tests with decreasing grain size [BARN04]. del Valle et al. [VALL06] studied the effects of the grain size on the ductility of AZ31 alloy processed by ECAP and large strain hot rolling. The grain refinement causes a strong decrease in the hardening rate. The samples with the grain sizes from 7 to 17 µm exhibit higher elongations and have larger hardening rates. On the other hand, the slope of the work hardening rate-true stress plots, which is related to dynamic recovery, is insensitive to the grain size [VALL06].

The grain size effect has led to an increasing interest in fabricating ultrafine-grained materials with extremely small grain sizes less than ~1 µm. For ultrafine-grained materials, there are the additional requirements of homogeneous and reasonably equiaxed microstructures with a majority of grain boundaries having high angles of misorientation. The presence of a high fraction of high angle grain boundaries is important to achieve advanced and unique properties [VALI04].

2.1.4.3 Deformation temperature

As described in section 2.1.2.1, the CRSS for non-basal slip systems decreases with increasing deformation temperature, and hence the activation of such slip systems becomes easier. Consequently, an increase of temperature results in a significant decrease in yield stress and an increase in the fracture elongation as displayed in Figure 2.10 (a). Furthermore, the work hardening decreases with increasing temperature due to thermally activated softening process as well as recovery.

Studies on single crystals of pure Mg show that the hardening rates in stages I and II have strong dependence on temperature [HIRS65]. In the case of AZ31 samples, work hardening rate decreases with increasing temperature, while dynamic recovery increases with test temperature as shown in Figure 2.10 (b). While the dislocation density decreases at the recovery (annihilation) and the dislocation arrangement changes (polygonization), the shape and size of the grains remain constant, but new dislocation-free grains form by means of the recrystallization at T > 220 °C, especially for AZ alloys [DAHL93, REDE09].

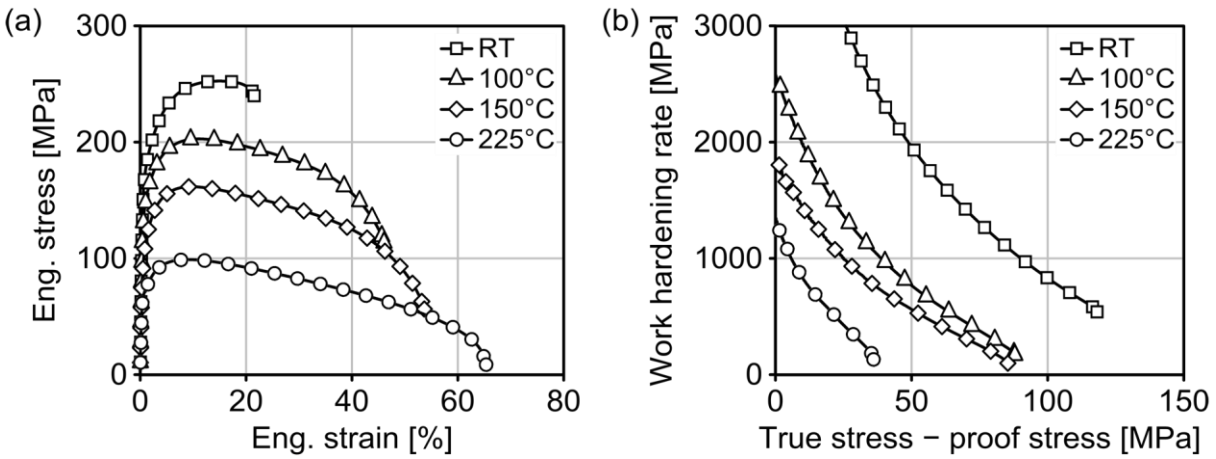

Figure 2.10: (a) temperature dependence of stress-strain curves of AZ31 sheet [NUER10], (b) corresponding work hardening rate as a function of $\sigma - \sigma_{0.2}$

With increasing temperature, the difference between the tensile and compressive yield stresses decreases until a temperature is reached, where two stresses are equivalent [AVED99]. Slip dominates at temperatures higher than this meeting point. Indeed, it has been observed in many metals that a transition from twinning- to slip-dominant deformation occurred with increasing temperature [CHRI95]. In Mg alloys, the transition can be interpreted as the point at which the macroscopic stress for the activation of tensile twinning corresponds to that for the activation of second order pyramidal <c+a> slip [BARN03].

Yi et al. [YI10] reported that the minimum temperature for the successful deep drawing is 150 °C for ZE10 sheet and 200 °C for AZ31 sheet, respectively. The AZ31 drawn cups showed the occurrence of dynamic recrystallization and the formation of $(0001)\langle 10\bar{1}0\rangle$ texture, where $\langle 10\bar{1}0\rangle$ direction is parallel to the drawing direction. This

texture development at 200 °C is mainly due to extensive prismatic <a> slip. With increasing temperature, the volume fraction of dynamically recrystallized grains becomes larger and the intensity of the $(0001)\langle 10\bar{1}0\rangle$ texture decreases. This indicates the activation of other deformation mechanisms and localized deformation in the dynamically recrystallized grains.

Forming limit curve (FLC) is most frequently used for predicting and evaluating the failure behavior in sheet metal forming simulation [VOLK12]. The calculated true strains ε_1 and ε_2 in FE simulations are compared to the theoretically or experimentally determined FLCs in post processing. The determination of FLCs is standardized in ISO 12004-2 by two different experimental methods, Marciniak [MARC67] and Nakajima test [NAKA68]. Figure 2.11 (a) describes the typical forming conditions and the FLC consists of their limit strains. The sheet formability is directly related to the strain states, which are characterized by the ratio between ε_1 and ε_2 [BANA10]. As one of the influencing parameters, the forming temperature has a different influence on the formability of different metallic alloys [BANA10]. For example, the formability of AA 5754 alloy shows a considerable increase in the temperature range from 250 to 350 °C, whereas the temperature variation in the same range has a little influence on the formability of AA 6111-T4 alloy [LI04].

The formability of AZ31 alloy sheets are investigated with respect to the deformation temperature [REDE09, BRUN10], forming speed [REDE09, BRUN10] and specimen orientation [BRUN10]. Figure 2.11 (b) presents the temperature dependent FLCs of AZ31 sheet with thickness of 1.6 mm. As expected, the accessible forming limits increases with the deformation temperature. This is due to the activation of additional slip systems and reduced work hardening. Moreover, the increase in the forming speed leads to the decrease in ε_1 and ε_2 because of the shortened recovery [REDE09]. Bruni et al. [BRUN10] also reported that the formability of AZ31 sheet is improved with increasing the forming temperature and decreasing the strain rate. Additionally, the sheet formability along the RD is higher than that along the TD, even if the FLCs obtained along the TD have a larger extension in the drawing side than the ones along the RD [BRUN10].

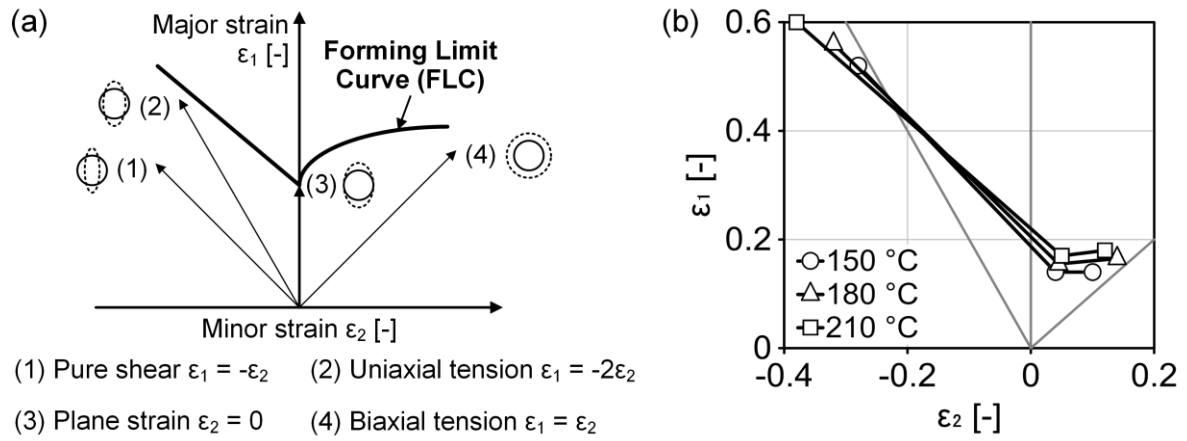

Figure 2.11: (a) schematic description of forming limit curve (FLC) [BANA10] and (b) temperature dependent FLC of AZ31 sheet with thickness of 1.6 mm [REDE09]

2.1.5 Processing techniques for formability enhancement

Previous studies show that there is a strong correlation between texture development during thermo-mechanical processing, slip systems, twinning mechanisms and resulting mechanical properties. In this context, it enables the control of the microstructure (grain size, grain distribution and texture) to improve mechanical and forming behavior at room temperature of wrought Mg alloys. For this reason, the application of severe plastic deformation (SPD) has recently received considerable attentions. This processing is a generic term describing a group of metalworking techniques introducing high shear strain or a complex stress state [WEI04]. Several processing techniques have been investigated and well established: e.g. differential speed rolling (DSR), high-pressure torsion (HPT), accumulative roll-bonding (ARB) and equal channel angular pressing (ECAP).

Differential speed rolling (DSR)

In DSR process, upper and lower rolls are driven with different rotation speeds so that shear deformation can be introduced throughout the sheet thickness. This intense shear strain can result in grain refinement and texture change [HUAN09]. The DSR process improved the tensile elongation primarily by reducing the preferred orientation of the basal (0001) plane with slight incline of the basal poles (by less than 10°) [WATA04-2, HUAN08].

High-pressure torsion (HPT)

HPT process involves compressive pressure of several GPa with concurrent torsional straining [ESTR13]. Hereby the discs are deformed by pure shear between two anvils, while one anvil rotates against the other anvil holding the material [ZHIL08]. A handicap of the method is that only small coin-shaped samples, typically 10-15 mm in diameter and 1 mm in thickness, can be processed [ESTR13]. Another disadvantage is that the processed microstructures are dependent on the applied pressure and the location within the disc [AZUS08].

Accumulative roll bonding (ARB)

In ARB process, stacking of sheets and conventional roll bonding are repeated in the process. Two sheets of the same material are stacked, heated (to below the recrystallization temperature), and joined by rolling. Subsequently, the length of the rolled material is sectioned into two halves, stacked and roll-bonded. The process can be repeated several times. Compared to other SPD processes, ARB has the benefit that it requires no additional specialized equipment or tooling, only a conventional rolling mill. However, joined surfaces must be well cleaned before rolling to ensure good bonding properties [SAIT99].

Equal channel angular pressing (ECAP)

Among others, ECAP process is an especially attractive processing technique for several reasons. First, it can be applied to large billets so that there is the potential for producing materials that may be used in a wide range of structural applications. Second, a relatively simple procedure is easily performed on a wide range of alloys. Third, reasonable homogeneity is attained through most of the as-pressed billet, if the pressings are continued to a sufficiently high strain. [VALI06]

Based on this, the next section describes the principle of the ECAP process, its influencing parameters and the resulting material characteristics in detail.

2.2 Equal Channel Angular Pressing

Processing of metals incorporating the application of SPD leads to changes in the structure of material and specially changes in the grain size and in its distribution [FIGU10-1]. There are numerous well-established techniques for imposing a strain on metallic samples by the standard industrial metal working processes such as rolling or extrusion. However, all of these methods require a change in the physical dimensions of the sample [FURU01]. By contrast, equal channel angular pressing (ECAP) (e.g. [FURU95]) or equal channel angular extrusion (ECAE) (e.g. [SEMI95]) can impose intensive shear strain on a sample without any change in the cross-sectional dimension [AGNE05-2]. Consequently, ECAP offers a possibility of producing semi-finished materials, which have fine grains with enhanced mechanical properties [FIGU10-1]. Historically, ECAP process was developed in the Soviet Union over thirty years ago [SEGA81], but it has received significant attention within the last two decades.

ECAP has been studied to explore fine-grained microstructure development and enhance mechanical properties in a wide range of metals and multi-phase alloys, such as pure aluminum [SUN07], Al alloys (e.g. 2024 [GOOD14], 7075 [SHAE15]), pure copper [HAOU05] and Mg alloys (e.g. AZ61 [KIM03], ZK60 [AGNE05-2]). Particularly, Lapovok et al. [LAPO08] showed a potential of ECAP processing of sheet material, where 6111 Al alloy sheet with a thickness of 2 mm was processed by ECAP and its strength was improved through the grain refinement. Based on these results, the potential of ECAP has recently reattained remarkable attention for improving the forming properties of Mg alloys through grain refinement [JIN05, KANG08] and crystallographic texture changes [AGNE04, SUWA07].

2.2.1 Principle of ECAP

ECAP provides a distinct possibility to reduce the grain size and generate unique textures. As a specimen is pressed through an angularly designed die, it is primarily deformed by simple shear along the intersection plane between the entrance and exit channels [AGNE04]. Because the entrance and exit channels have an identical cross section, this process is called as equal channel angular processing.

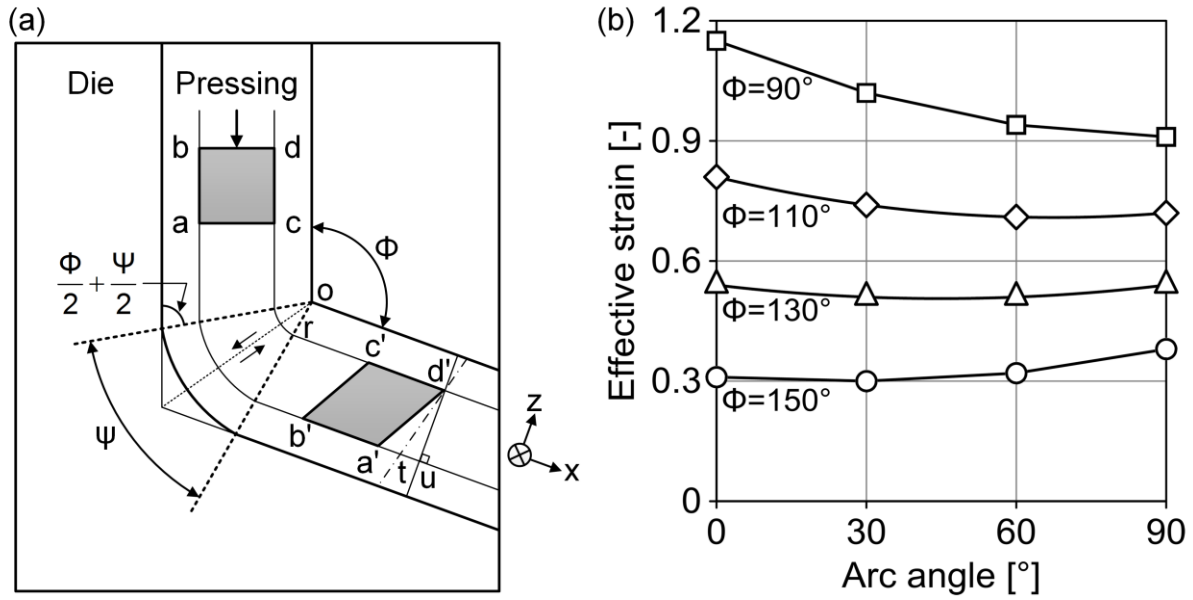

Figure 2.12: *(a) principle of ECAP where Φ is the angle of intersection of the two channels and Ψ is the angle subtended by the arc of curvature at the point of intersection, 0 ≤ Ψ ≤ π-Φ [IWAH96], (b) equivalent plastic strain for a single pass using variable channel and arc angles by Equation 2.8 [LUIS04]*

Figure 2.12 illustrates the principle of ECAP schematically. The sample is pressed through the die, where two channels of equal cross section intersect at an oblique angle Φ. The arc angle (Ψ) is defined as the angle subtended by the arc of curvature at the point of intersection and lies between Ψ = 0° and Ψ = π-Φ [IWAH96]. Shear deformation is imposed at the shear plane between the two adjacent segments as depicted in Figure 2.12 (a). A square element in the entrance channel, labeled abcd, passes through the theoretical shear plane and becomes distorted into the parallelogram labeled a'b'c'd'. The shear strain (γ_{xz}) is given for a general form by [IWAH96]:

$$\gamma_{xz} = 2\cot\left(\frac{\Phi}{2}+\frac{\Psi}{2}\right)+\Psi\,\mathrm{cosec}\left(\frac{\Phi}{2}+\frac{\Psi}{2}\right) \tag{2.7}$$

When the sample passes through the die, the von Mises equivalent strain depends on the channel and arc angles Φ and Ψ. Moreover, the cross-sectional dimensions of the sample remain unchanged with a single pass through the die and the same strain is accumulated in each pass. Finally, the equivalent strain after N passes ($\bar{\varepsilon}_N$) was expressed by the relationship [IWAH96]:

$$\bar{\varepsilon}_N = \frac{N}{\sqrt{3}}\left[2\cot\left(\frac{\Phi}{2}+\frac{\Psi}{2}\right)+\Psi\,\mathrm{cosec}\left(\frac{\Phi}{2}+\frac{\Psi}{2}\right)\right] \tag{2.8}$$

There has been reasonable evidences supporting this relationship from experiments using a specimen with a grid pattern [SHAN99] and from two-dimensional finite element analysis [DELO99]. Furthermore, an alternative relationship was proposed by [GOFO00]:

$$\bar{\varepsilon}_N = \frac{N}{\sqrt{3}}\left[2\cot\left(\frac{\Phi}{2}+\frac{\Psi}{2}\right)+\Psi\right] \tag{2.9}$$

According to the analytical investigation [AIDA01], Equations 2.8 and 2.9 are equivalent at the upper and lower bounds of the arc angle. The deviations of the predicted strains using both equations are lower than 5% under conditions for any channel angle of $\Phi \geq 90°$.

An analysis of the stresses and strains for channel angular pressing was carried out, in which the two channels have different cross-sectional dimensions [LEE00]. Moreover, a finite element analysis was performed, in order to investigate the effect of the corner gap formation between the workpiece and die at the outer arc of curvature, where the channels intersect [KIM00].

Figure 2.12 (b) provides a graphical representation of Equation 2.8 and a simple understanding of the influence of the angles Φ and Ψ. Here the deformation values are obtained, where the Φ ranges from 90 to 150° and the Ψ varies from 0 to 90° for a single pass with N = 1 [LUIS04]. Figure 2.12 (b) represents that the Ψ has a relatively minor effect on the equivalent strain. Exceptionally high strains may be achieved in a single pass by constructing a die with low values of Φ and Ψ [VALI06].

There are four basic processing routes in ECAP. These routes introduce different slip systems during the pressing operation so that they lead to significant differences in the microstructures produced by ECAP [FURU02, JUFU10]. Figure 2.13 describes schematically the four different processing routes. They are termed as A, B_A, B_C and C according to the rotation angle about the longitudinal axis of the sample or pressing

direction (PD) [JUFU10]. On route A, the sample is pressed without rotation between consecutive passes. Routes B_A and B_C refer the processes with rotations of 90° in alternate directions or the same direction between each pass. Finally, the sample is deformed on route C with a rotation of 180° between passes [FURU02].

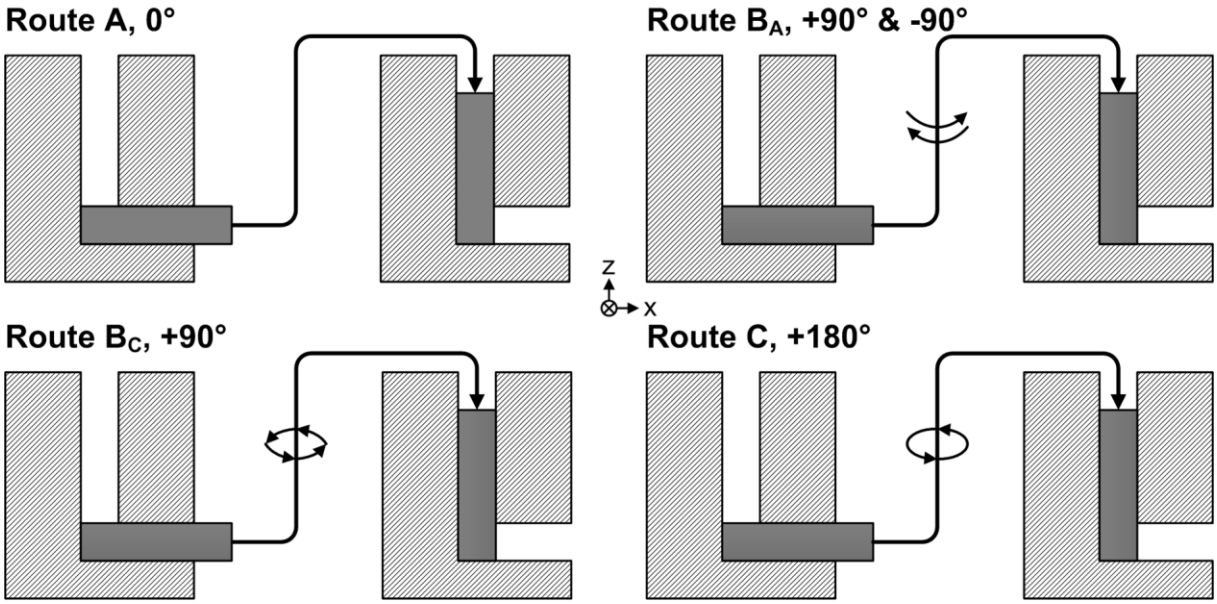

Figure 2.13: Schematic representation of four fundamental processing routes A, B_A, B_C and C in ECAP [FURU01]

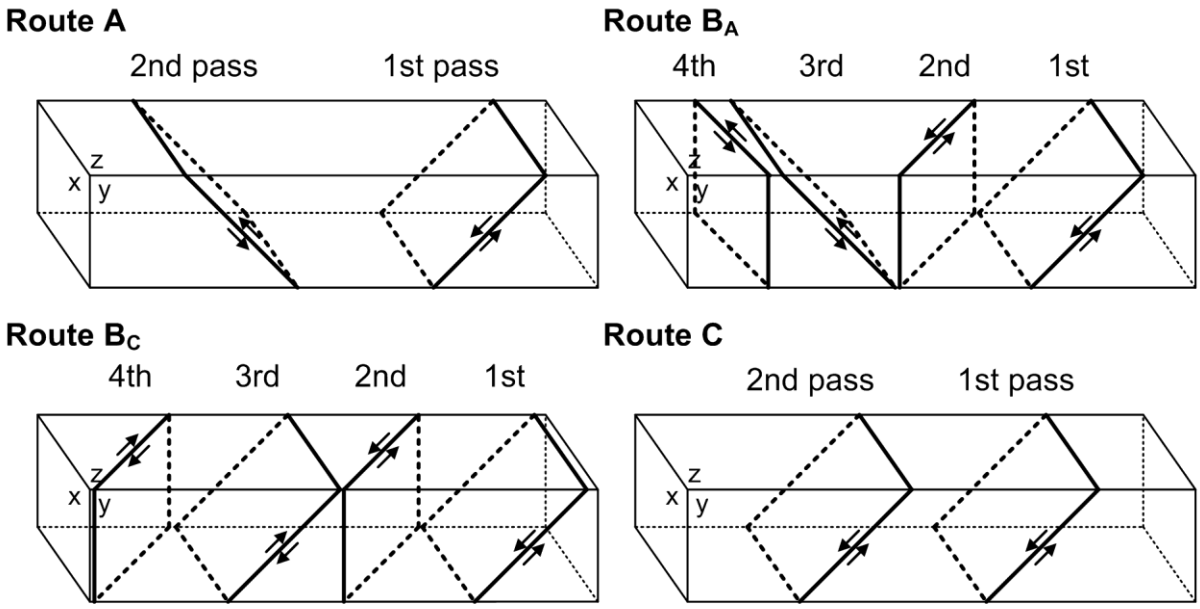

Figure 2.14: Shearing planes associated with consecutive passes using processing routes A, B_A, B_C and C [FURU01]

Figure 2.14 represents schematically the different slip systems associated with four processing routes. The planes x, y and z indicate three orthogonal planes and the planes labelled one through four denote the shearing, which occurs on the first four passes through the die. Processing on route A leads to shearing on two planes intersecting at 90°, processing on route C leads to repetitive shearing on the same plane, and processing through routes B_A and B_C leads to shearing on a set of planes intersecting at 120° [FURU01].

2.2.2 Factors influencing ECAP and material characteristics

As processing by ECAP, several factors influence on the workability and the microstructural characteristics of the ECAPed materials [VALI06]. In order to activate additional slip systems and enhance limited forming properties, it is essential to process Mg and its alloys thermo-mechanically. Especially, Mg alloys should be warm-worked for avoiding premature fracture of workpiece at ECAP. The channel angle, processing route and number of the passes in ECAP have also a considerable effect on the imposed shear strain and the orientation of the shear plane. Both the amount of the shear strain and the orientation of the shear plane depend primarily on the channel angle [FIGU10-2]. Although the multi-pass process is not continuous, the accumulated shear strains lead to different shear orientations depending on the processing routes [FURU02]. Such a plastic deformation process results in a reorientation of the lattice of individual grains and tends to develop a specific texture [SUWA07].

A variety of studies have reported the effect of the process parameters on the microstructural evolution and resulting mechanical properties. This section focuses on three key factors, i.e. processing temperature, channel angle and processing route, for the description of their influences on the microstructural and mechanical characteristics in Mg alloys.

2.2.2.1 Processing temperature

The processing temperature is a key factor in any use of ECAP, since it can be controlled relatively easily [VALI06]. Early studies showed that dynamic recrystallization occurred in Mg alloys, which were deformed in the temperature range from 175 to

325 °C [AGNE05-2]. This corresponds to the temperature range often applied to the processing of Mg alloys by ECAP [FIGU10-1].

In Mg-Al alloys, the resulting microstructures depend on the aluminum content [MUSS06]. In the case of AZ31 alloy, various recrystallized grain sizes were reported depending on processing conditions. As processing temperature at 200 °C, a homogeneous fine structure with grain size of ~1 µm was reported [MUKA01], whereas recrystallized grains with ~5 µm were observed at 270 °C [YUAN04]. For AZ91 alloy, low-temperature superplasticity was obtained after ECAP in a temperature range from 175 to 250 °C, where the grain size was reduced to ~0.5-1 µm [MABU97].

Agnew et al. [AGNE05-2] reported the texture evolution of five Mg alloys in the temperature range from 175 to 325 °C using experiments and simulations. AZ31 and AZ80 alloys tend to exhibit balanced secondary slip of non-basal <a> and <c+a> dislocations, while ZK60 and WE43 tend to favor non-basal <c+a> slip. A binary Mg-Li alloy exhibits a radically distinct texture evolution, which is associated with large-scale strain accommodation by non-basal <a> slip [AGNE05-2]. The composition, grain size and processing temperature will affect the ratio between the basal and non-basal slip activity. In general, higher processing temperatures and smaller grain sizes favor the occurrence of non-basal slip [FIGU10-2].

Jufu et al. [JUFU10] investigated the influence of the processing temperature on the material properties processed by ECAP and Table 2.7 summarizes the room temperature mechanical properties of ECAPed AZ91 alloy for six passes on the route B_C at various processing temperatures. At processing temperature of 225 °C, the room temperature mechanical properties are highest: YS of 209 MPa, UTS of 339 MPa and ε_f of 14.1%. Microstructural analysis showed that average grain size decreases from 10 to 4 µm in the temperature range from 150 to 225 °C. Otherwise, average grain size increases from 4 to 9 µm with temperature from 225 to 300 °C. This is due to double influences of processing temperature on dynamic recrystallization degree and grains coarsening rate of ECAPed materials [JUFU10]. Maximal dynamic recrystallization temperature of AZ91 alloy is about 224.6 °C [CUI96]. Hereby the balanced processing temperature is 225 °C with respect to mechanical properties.

	Processing temperature [°C]						
	150	***175***	***200***	***225***	***250***	***275***	***300***
YS [MPa]	*176*	*185*	*198*	*209*	*183*	*157*	*142*
UTS [MPa]	*266*	*273*	*298*	*339*	*289*	*262*	*245*
ε_f *[%]*	*10*	*11.3*	*12.1*	*14.1*	*12.4*	*11.4*	*9.8*

Table 2.7: Effect of processing temperatures on room temperature mechanical properties of ECAPed AZ91 alloy for six passes [JUFU10]

2.2.2.2 Channel angle

The channel angle Φ is the most significant factor, which has a direct influence on the total strain imposed in each pass and the characteristics of the ECAPed microstructure. Despite the critical importance of this angle, earlier experiments were performed exclusively using ECAP dies with Φ from 90 to 120° [MUKA01, FURU02]. There is generally little attempt to make any significant comparison between the results obtained with different channel angles [VALI06]. It is clear that variations in the channel angle will influence the texture change due both to the different orientations of the shear planes and the different strains imposed in every pass [FIGU10-2].

Figueiredo et al. [FIGU10-2] investigated texture evolution in a ZK60 alloy processed by ECAP with three different channel angles of Φ = 90, 110 and 135° and the textures were predicted using a visco-plastic self-consistent (VPSC) simulation. The strain per pass in dies with Φ = 90, 110 and 135° amounts to ~1.1, 0.8 and 0.5, respectively, as plotted in Figure 2.12 (b). The experimental measurements of ECAPed ZK60 alloy showed only minor changes in the original texture through a single pass at Φ = 110° and essentially no change at Φ = 135°. On the contrary, VPSC simulation predicted that there was significant activity of prismatic <a> slip and pyramidal <a> slip during ECAP in all cases [FIGU10-2].

2.2.2.3 Processing route

The microstructural and mechanical characteristics of ECAPed materials are essentially influenced by different slip systems and shearing patterns associated with the four fundamental processing routes A, B_A, B_C and C. Based on this, numerous studies reported the influences of processing routes on ECAP.

Regarding the microstructure evolution during ECAP with different routes, route B_C is the most effective and route A is the least effective route for the grain refinement [IWAH98]. On route A, the shear directions are only in the y-plane during consecutive passes, and hence the extent of shearing is divided equally between two sets of orthogonal planes as illustrated in Figure 2.14. On route B_A, the billet is deformed on two shear planes between each cycle. This reduces the formation rate of high angle grain boundaries, and hence it slows down the speed of dynamic recrystallization [GHOL00]. On route B_C, the shear strain operates both in the y- and z-planes, because the shearing directions of each pass locate on planes intersecting at 120° and the specimen is rotated in the consecutive passes. Consequently, the subdivision effect is enhanced, representing the most effective grain refinement [TONG10]. On route C, the shear directions are inverted and parallel to each other in the same shear plane during adjacent passes. This might result in a higher dislocation accumulation in the shear bands and enhance dynamic recrystallization [TONG10].

Tong et al. [TONG10] showed the texture evolution in the Mg-Zn-Ca alloy processed by ECAP using different routes. Route A induced a basal texture with most of {0002} planes parallel to pressing and transverse directions. Route B_C led to a texture with the maximum density of {0002} pole figure locating at 36° to the PD and the texture was rotated ~15° around the axis of the shear direction. Route C developed the strongest texture with {0002} plane inclining ~45° to the PD. Jufu et al. [JUFU10] also investigated the Influence of processing routes on room temperature mechanical properties of AZ91 alloy, which was processed by ECAP for six passes at 225 °C. Table 2.8 shows that route B_C, C and A produced the highest, second highest and lowest YS, UTS and ε_f, respectively.

	Processing route			
	A	***B_A***	***B_C***	***C***
YS [MPa]	*180*	*196*	*209*	*199*
UTS [MPa]	*266*	*306*	*339*	*317*
ε_f [%]	*10.8*	*11.2*	*14.1*	*13.1*

Table 2.8: Influence of processing routes on room temperature mechanical properties of ECAPed AZ91 alloy for 6 passes at 225 °C [JUFU10]

3 Testing and Measuring Equipment

3.1 Hydraulic presses

Single acting hydraulic press

To perform ECAP trials, the single acting hydraulic press DXU 320 B manufactured by Dieffenbacher GmbH & Co. KG is available. In this press, the process parameters can be set using the press control and varied over a wide range. For example, the course of the ram speed can be specified during the closing motion of the tool [NUER10]. Table 3.1 presents the selected specifications of the hydraulic press.

Parameter	***Value***	***Unit***
Maximum pressing force	*3500*	*kN*
Maximum drawing cushion force	*1300*	*kN*
Maximum ram speed	*53*	*mm/s*
Usable work surface	*1600 × 1300*	*mm*
Maximum installation height	*900*	*mm*
Maximum stroke	*600*	*mm*

Table 3.1: Technical data of single acting hydraulic press DXU 320 B

Hydraulic drawing press

A hydraulic C-frame Press Typ TEZ 40 B with drawing cushion (Eitel KG Werkzeugmaschinenfabrik) was used for the implementation of the forming tests. The key characteristics of the hydraulic press are listed in Table 3.2

Parameter	***Value***	***Unit***
Maximum pressing force	*400*	*kN*
Maximum drawing cushion force	*220*	*kN*
Maximum ram speed	*40*	*mm/s*
Usable ram surface	*450 × 500*	*mm*
Maximum installation height	*750*	*mm*
Maximum stroke	*500*	*mm*

Table 3.2: Technical data of hydraulic drawing press TEZ 40 B

3.2 ECAP tool

For the application of ECAP process, it is necessary to develop, implement and test an industry-related tool technology for heating and control of channel parts. The tool design and manufacturing drawings are created with the three-dimensional CAD software tool CATIA V5 R19 (Dassault Systèmes).

The following functions and requirements are implemented in the tool for the application of ECAP process to Mg sheets:

- Modular design for the integration of the channel components with various channel angles
- Applicability in the hydraulic press Dieffenbacher
- Selective temperature control of the channel components with a thermal insulation of the basic tool frame
- Constructive prevention of changes in the clearance between the channel components due to the thermal expansion
- Acquisition of the process data by means of suitable sensors

3.2.1 Tool design

An ECAP tool is designed and manufactured for the introduction of shear strain into sheets as described in Figure 3.1. As a constraint in the tool design, it is established for the minimization of energy consumption that there is no pre-heating of the sheet. The process heat should be utilized to the sheet only from a narrow zone along the locally heated channel radii. For this, the tool guide is separated by an insulation of the heated tool active elements, in order to reduce the risk of unfavorable buckling or transverse loading by thermal strain as much as possible [SUH15].

In the basic structure, the tool is quite similar to a three-part cutting tool. It consists of three main assembly modules upper tool, blank holder and lower tool as depicted in Figure 3.1 (a). This experimental tool combines three main parts in the tool frame with dimensions of 996 × 796 × 865 mm^3. For additional stiffening, the tool frame is furnished with four guide pillars with precision-ball cages (FIBRO GmbH). To adjust the

tool closing height in the test press, a flat plate with height of 135 mm is mounted below the base plate of the lower tool at the installation of the ECAP tool in the press.

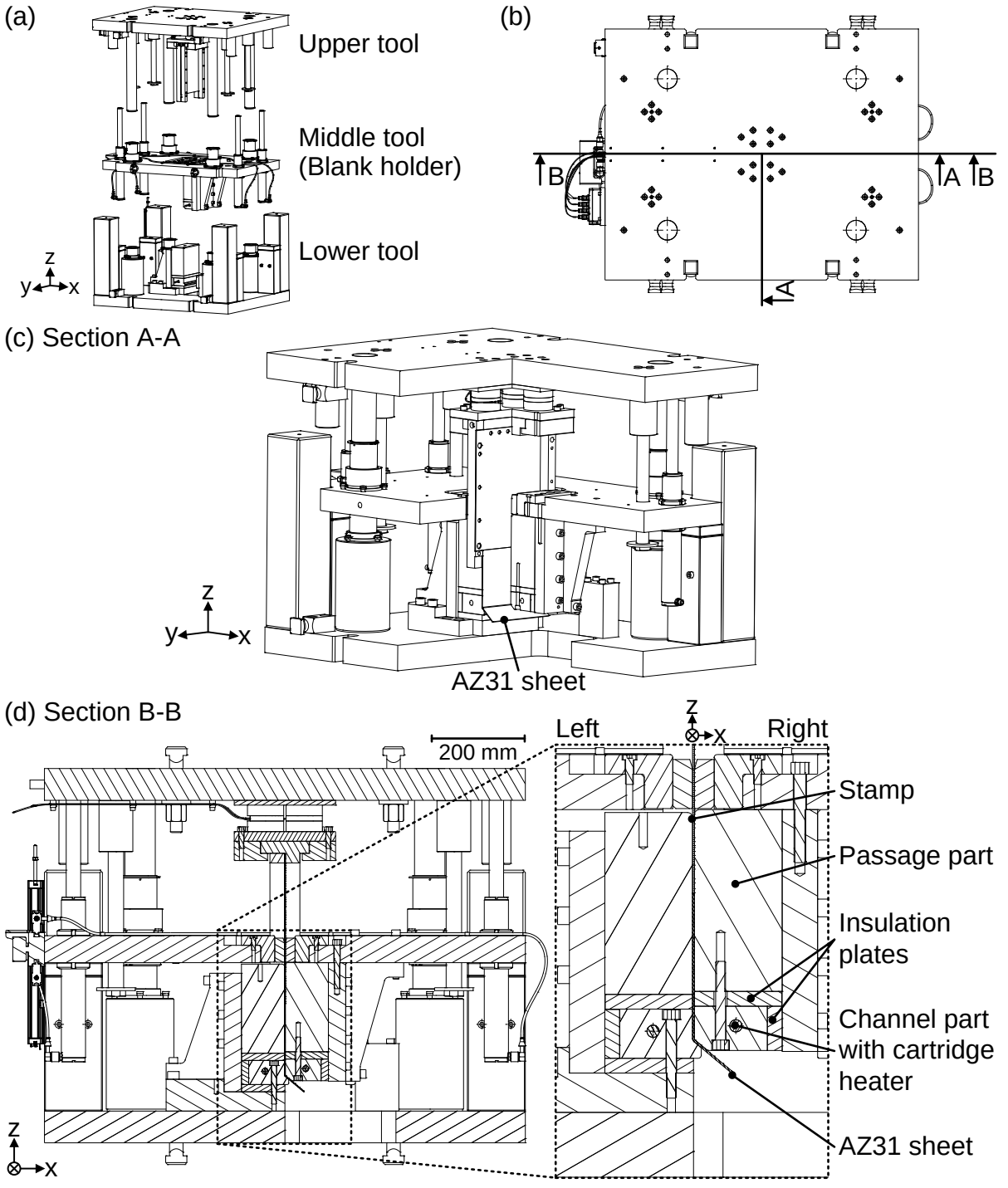

Figure 3.1: Description of developed ECAP tool: (a) main assembly modules of ECAP tool, (b) top view, (c) section A-A, (d) section B-B [SUH15]

In the open position, a sheet with dimensions of 200 × 200 × 1.8 mm^3 is laterally inserted between the right and left tool parts. It stands on the outer radius of the left channel part. Here the right and left radius of the channel components is 2 and 4 mm, respectively. During closing of the blank holder plate including the right tool part, the sheet is locally heated by both channel components, which are pre-heated within a temperature range from 175 to 225 °C using two cartridge heaters. Subsequently, the sheet is pressed through the channel parts with the constant press speed of 5 mm/s. Consequently, the shear strain can be imposed on the sheet [SUH15]. As the upper tool returns to the initial open position at the end of the ECAP process, it is easy to remove the ECAPed sheet from the tool. This is the main reason for the application of the tool concept of a three-part cutting tool.

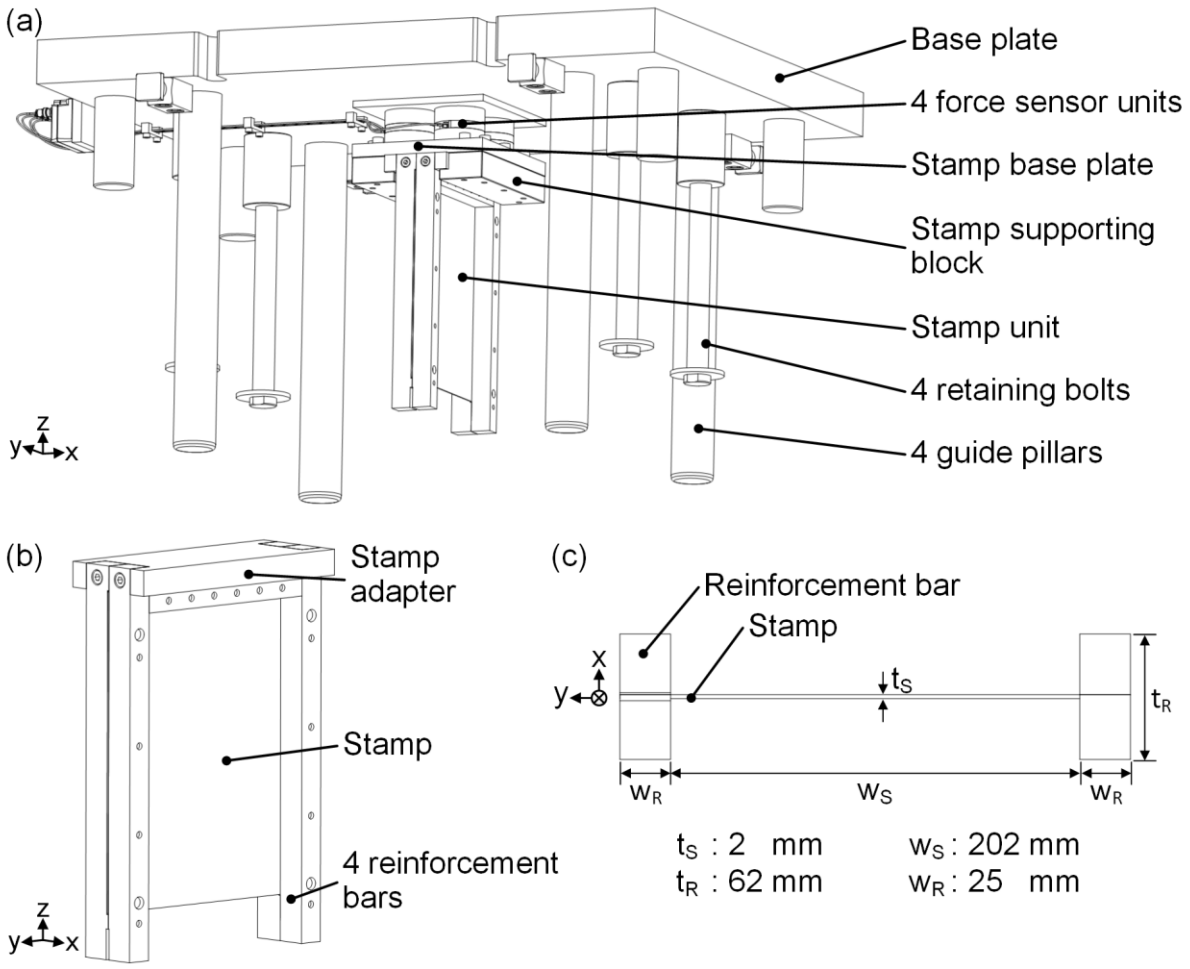

Figure 3.2: Assembly of upper tool: (a) overview of upper tool, (b) stamp unit, (c) stamp, (d) bottom view of stamp unit without stamp adapter

3.2.1.1 Upper tool

The upper tool consists mainly of stamp unit, force sensor units, guide pillars and the retaining bolts for lifting the blank holder plate, which are placed on the base plate with dimensions of 996 × 796 × 66 mm^3 (Figure 3.2). The distribution of four force sensor units is beneficial to the tipping stability of the stamp unit. The double T-shaped stamp unit consists of the flat stamp, four reinforcement bars and two-part stamp adapter as presented in Figure 3.2 (a). It has a clearance fit of 10 µm upwards to the stamp base plate and there is a gap of 1 mm between stamp adapter and stamp supporting blocks to the x-direction. With these clearance fits, the stamp unit is floating-suspended between them. The other reason for the floating-suspension is to dissemble the stamp unit easily, in case of an unexpected jamming with tool active elements and sheet. Figure 3.2 (c) and (d) presents that the four reinforcement bars increase the buckling resistance of the stamp with a high slenderness of 156. In order to estimate risk of buckling, the critical vertical force on the I-beam shaped stamp unit is calculated by the Euler's formula [HIBB00]. This formula gives the maximum axial load on a long, slender and ideal column just before it begins to buckle as follows:

$$F_c = \frac{\pi^2 E I}{(K L_C)^2} \tag{3.1}$$

where F_c is the critical force (vertical load on column), E is the young's modulus, I is area moment of inertia, L_C is the unsupported length of column and K is the effective length factor, whose value depends on the conditions of end support of the column. Here K L_C is the effective length of the column. The case of the presented stamp unit corresponds to the fourth mode (Appendix Figure 9.1). During the ECAP process, both ends of the stamp are fixed by the stamp adapter and AZ31 sheet. At the fixed ends, the dimensionless effective length factor (K) corresponds to 0.5 [HIBB00].

For I-beams, the area moments of inertia to the x- and y-direction, I_x and I_y are given as follows:

$$I_x = \frac{t_S w_S^3}{12} + \frac{t_R w_R^3}{6} + \frac{t_R w_R (w_S + w_R)^2}{2} \tag{3.2}$$

$$I_y = \frac{t_S^3 w_S}{12} + \frac{t_R^3 w_R}{6} \tag{3.3}$$

The parameters for Equations 3.2 and 3.3 are summarized in Figure 3.2 (d). The calculated area moment of inertia in the x- and y-axis is 41.5×10^6 and 0.99×10^6 mm^4, respectively.

In consideration of the young's modulus of the applied steel plate for the stamp (E = 217.6 GPa), the critical buckling load to the x- and y-axis is 3660 and 28 MN, respectively. By comparison, as the load along the z-direction is increased, the stamp unit can be buckled to the y-axis. Regarding the temperature dependent strength of AZ31 sheet, the estimated forming force during ECAP is ~15 kN using finite element (FE) simulation (section 3.2.3). That is, the resulting loading to the z-axis at the stamp unit is much lower than the critical buckling load to the y-axis. Therefore, there is no risk of buckling in both directions at this reinforced stamp unit during ECAP. At the blank holder plate, the thin stamp and four reinforcement bars are additionally guided by the sliding pads of bronze with non-liquid lubricant (FIBRO GmbH) for reducing any risk of buckling.

3.2.1.2 Middle tool (blank holder)

Figure 3.3 shows the assembly of the middle tool, which consists of the blank holder plate with dimensions of 996 × 646 × 56 mm^3, the tool active elements on the right side, gas cylinders and guide elements. For the stability and sheet removal, the blank holder plate is integrated in the middle tool. Since the active elements on the right side are assembled under the blank holder plate, it is easy to remove the ECAPed sheet from the tool. Here the gap between the channel components on the right and left sides is defined as the entrance and exit heights of the sheet. The blank holder plate presses against the stop washers using four nitrogen gas cylinders HF 1000-250-A-N (MICRONORM Woronka GmbH), ensuring a constant exit height during the process. This gas spring has the spring displacement of 250 mm and the initial force of 10.6 kN at 150 bar and 20 °C. At the maximum displacement, the spring force reaches ~21 kN. Each gas cylinder is mounted on the blank holder plate using two shaft nuts.

The positioning of the tool active elements on the right side is carried out using four guide bushes with the precision-ball cages in the blank holder plate. The active elements below the blank holder plate are segmented to ensure the positional accuracy under temperature changes. The right channel component is heated by a cartridge heater hotrod® Typs 4052047 (Hotset Heizpatronen und Zubehör GmbH). This heating element is one of high power cartridge heaters with a diameter of 12.5 mm and a length of 200 mm, providing a surface heat load of 14.0 W/cm^2. The heated channel component is thermally insulated by a 15 mm thick heat protection plate KV® 3 (Brandenburger Isoliertechnik GmbH). This insulation plate exhibits excellent thermal properties (maximal long-term temperature resistance of 250 °C and thermal conductivity at 200 °C of 0.30 W/mK) with high stiffness (compressive strength at 200 °C of 450 MPa and bending resistance of 350 MPa).

In terms of the tolerance between the stamp unit and sliding pads in the blank holder plate, there is a clearance between the stamp and sliding pads with a range from 0 to 60 µm, which corresponds to a transition fit. For the reinforcement bars there is also a transition fit with a tolerance range between 0 and 120 µm. These transition fits between the stamp unit and middle tool are compensated by the floating-suspension the stamp unit in the upper tool [JUNG13].

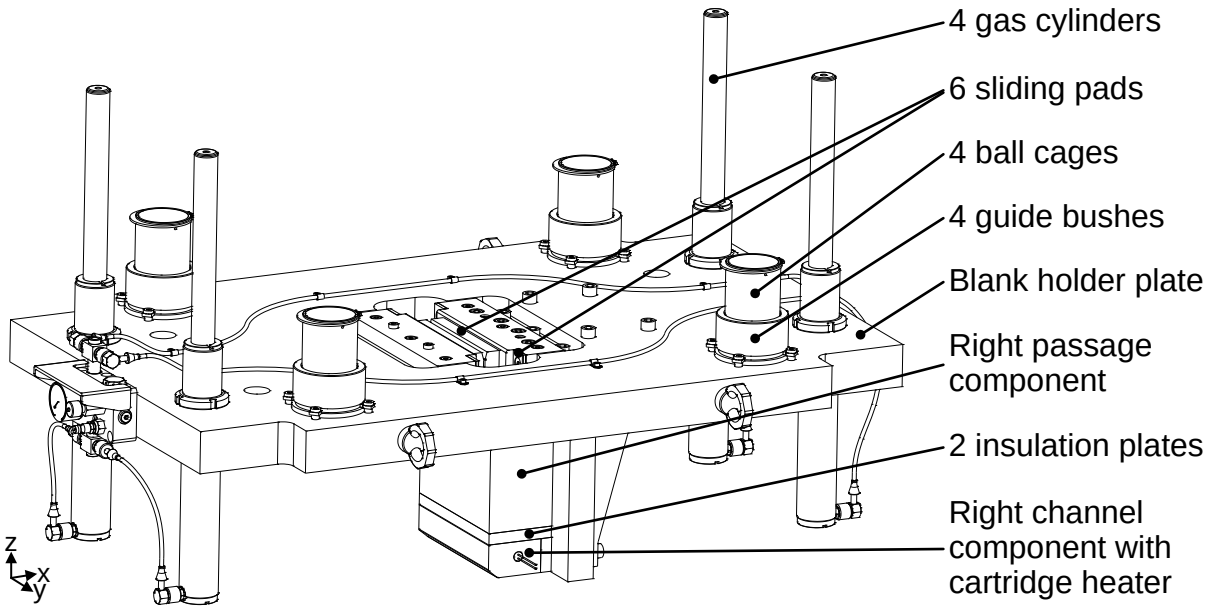

Figure 3.3: Assembly of middle tool

3.2.1.3 Lower tool

In Figure 3.4, the tool active elements on the left side, the stop blocks for the upper and middle tools as well as the receiving columns for the guide pillars are located on the base plate with dimensions of 996 × 796 × 66 mm^3. Similar to the middle tool, the heating on the left channel component is localized by the insulation plates. Hereby the guide elements are thermally decoupled, and hence the tool frame is protected against heating. Therefore, the tool guide is separated and the guide elements align three main assembly modules without unfavorable thermal effect.

The angular assembly unit fastens the left tool active elements to the base plate with the cylinder head screws. It is positioned with two cylinder pins and fixed with the cylinder head screws. As a result, the reaction forces in x- and y-axis are absorbed in a force-locking manner with cylinder bolts and in a form-locking manner with the cylinder pins [JUNG13].

The base plate has an empty space in the center for the exit of ECAPed sheets. At the corners of the plate, four stop blocks for the upper tool stand, with which the bottom dead center is defined. Furthermore, four stop washers with differential heights are mounted on the stop blocks for the middle tool, and thus enable the variation of the exit height.

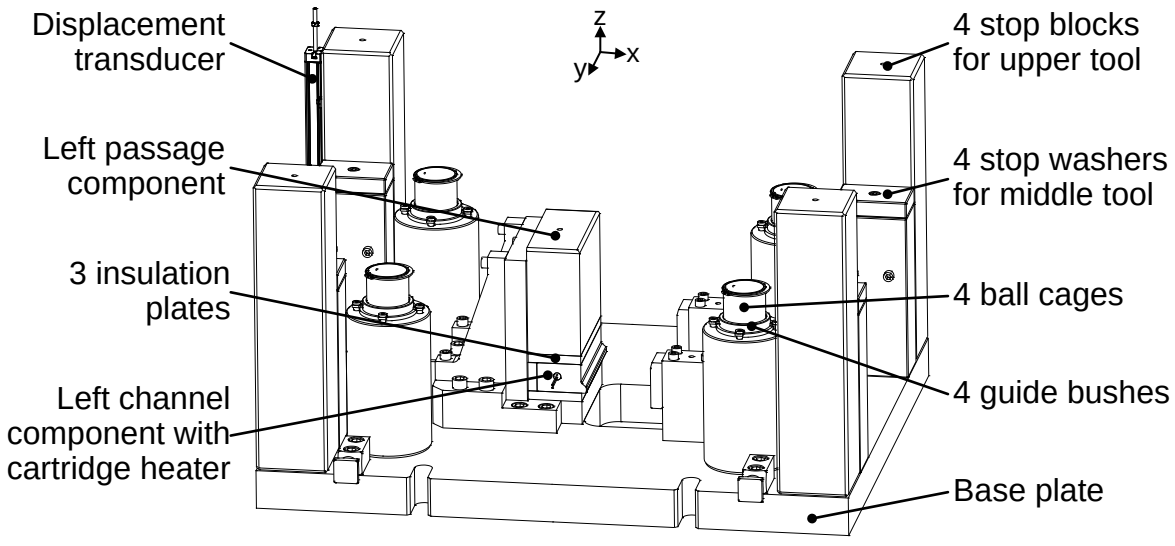

Figure 3.4: Assembly of lower tool

3.2.1.4 Kinematics of ECAP tool

The kinematics of the presented ECAP tool is described in detail in Figure 3.5.

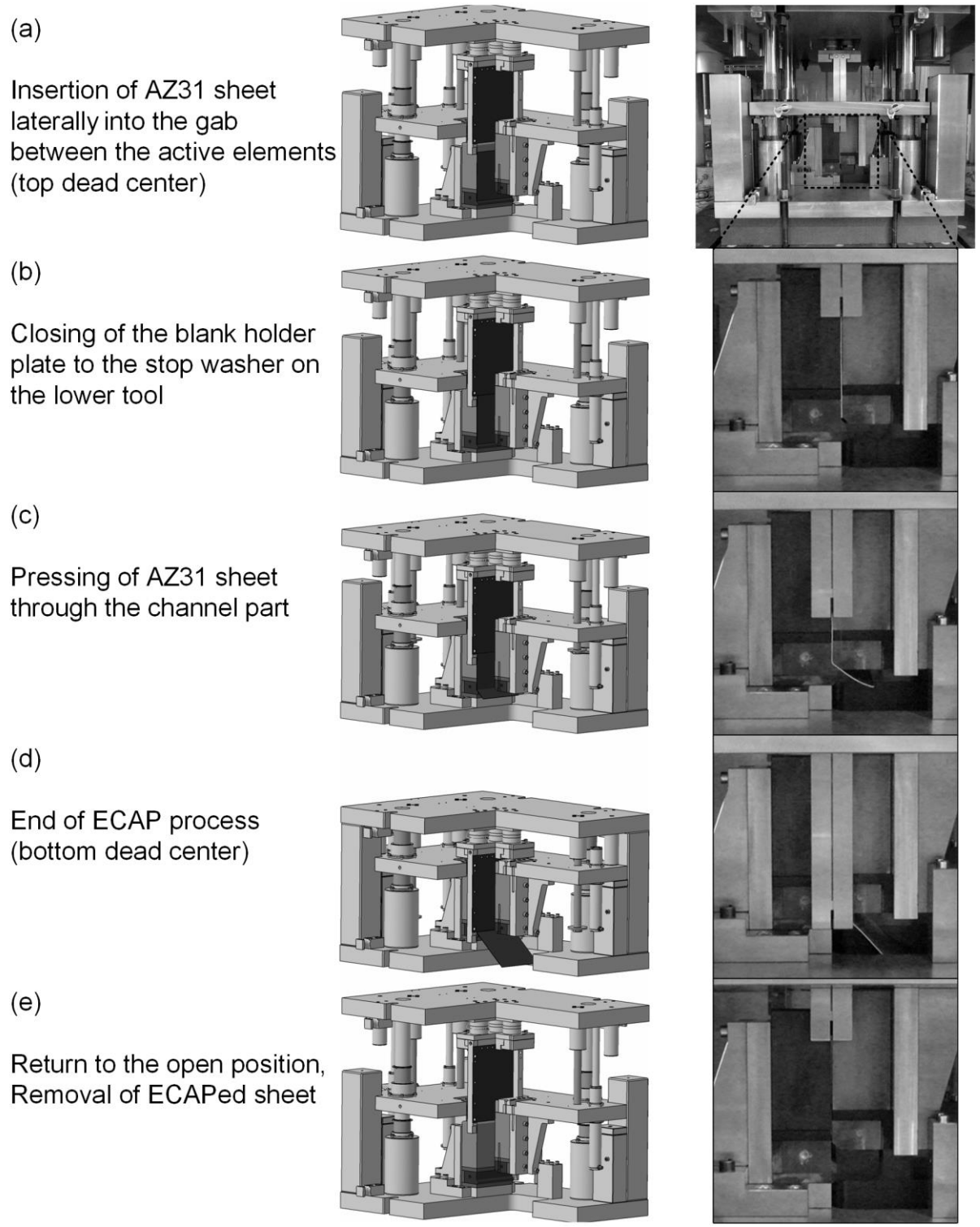

Figure 3.5: Kinematics of ECAP tool: (a) top dead center, (b) closing of blank holder plate, (c) pressing, (d) bottom dead center, (e) tool open for sheet removal

3.2.1.5 Tool materials and coating

The tool active elements with sheet contact such as stamp, passage part and channel part are subject to high intensive wear and compression at elevated temperatures during the ECAP process. Because of the high slenderness ratio of the stamp, high buckling resistance and toughness are essential for manufacturing the stamp. On the other hand, the right and left channel parts require high compression strength and excellent wear resistance against abrasion and adhesion.

Stamp

The flat stamp consists of a powder metallurgy cold work tool steel BÖHLER K890 MICROCLEAN® with 58 ± 1 HRC (BÖHLER Edelstahl GmbH & Co KG). This material exhibits highest ductility and fatigue strength as well as good compressive strength and thermal stability. Hence, it is suitable for forming process at lower temperatures under extremely high plastic loading [BOEH11]. A diamond-like carbon (DLC) coating SUCASLIDE® (Eifeler Werkzeuge GmbH) is applied to the stamp. The metal-containing amorphous carbon layer is deposited by the PVD process (physical vapor deposition) and is characterized by an extremely low friction coefficient [EIFE14-1]. This coating is beneficial for the relative movement of the stamp between the passage and channel parts.

Passage part

A common cold work steel 1.2379 with 60 ± 1 HRC is used for the passage part because of the functional simplicity and geometric shape. No extra coating is employed on its surface.

Channel part

In the channel part, which is the actual die component, Mg sheets are sheared along the channel radii at a certain angle. The highest degree of wear is expected to occur at the inner radius of the right channel component. For this reason, both channel components are made from a powder metallurgy cold work tool steel BÖHLER K390

MICROCLEAN® with 62 ± 1 HRC (BÖHLER Edelstahl GmbH & Co KG). The key features of this tool material are extremely high wear resistance, excellent toughness and very high compressive strength [BOEH14]. They are coated by the combination of CrCN (chromium carbon-nitride) and SUCASLIDE® of Eifeler Werkzeuge GmbH. Especially, chromium-carbon nitride layer offers high hardness and adhesive strength and is suitable for the forming of non-ferrous metals [EIFE14-2].

3.2.2 Process data acquisition

In order to monitor the process and the interpretation of test results, force, temperature and displacement sensors are integrated in the test tool.

3.2.2.1 Force sensor

The force measurement is performed in the direct connection of the main load with the stamp unit. The processing force is measured by means of four piezoelectric load washers Type 9031A (Kistler Instrumente GmbH). This 1-component force sensor measures the compression force F_z with a range up to 60 kN. The stiff, preloaded and piezoelectric force sensors generate electric charge proportional to the resulting force. The four force sensors are connected by four connecting cables (Type 1983AD, Kistler Instrumente GmbH) to a charge amplifier (ICAM Type 5073A411, Kistler Instrumente GmbH), which converts the incoming charge into analog voltage signals. This charge amplifier has a 15-pin D-sub connector for further communication with the data acquisition system (see section 3.2.2.4).

3.2.2.2 Thermocouple temperature sensor

For the monitoring of the processing temperatures, four mineral insulated thermocouples Typ K with diameter of 1.5 mm (TC Mess- & Regeltechnik GmbH) are available for both channel components. These thermocouples are connected to the hotcontrol® temperature multiple controller (RR 600, hotset Heizpatronen und Zubehör GmbH) for the temperature control of two cartridge heaters. The tips of thermocouples are located at 3 mm away from the effective surface of both channel components as depicted in Figure 3.6.

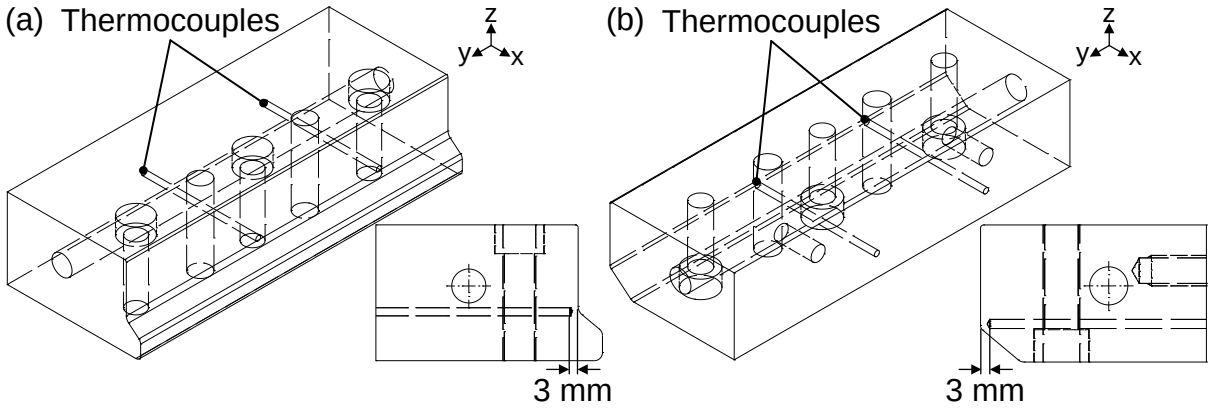

Figure 3.6: Arrangement of thermocouples in the channel part: (a) left channel component, (b) right channel component

3.2.2.3 Displacement transducer

A linear potentiometer type LRW-M-300-P (WayCon Positionsmesstechnik GmbH), measures the distance between the lower and upper tool with a measuring range of 300 mm. Its maximal linearity amounts to ± 0.05% and the displacement speed is lower than 10 m/s. The resolution depends on the signal quality of the reference voltage [WAYC14].

3.2.2.4 Data acquisition and evaluation

The process data are recorded with the aid of an eight-slot NI CompactDAQ chassis (NI cDAQ-9172, National Instruments Corporation). For the scanning of force signals, the C-module NI 9215 (National Instruments Corporation) is used with four simultaneously sampled analog inputs of 100 kS/s and a 16-bit resolution. The additional module NI 9215 records the incremental signals of displacement transducer. Finally, a 4-channel, 24-bit thermocouple input device (NI 9211, National Instruments Corporation) is utilized for the measurement of temperature changes. As data acquisition and evaluation software, the software package NI LabVIEW 2011 SP1 of National Instruments Corporation is available coupled with the recording system.

3.2.3 Thermal design and functional certification

For a reliable processing of the developed test tool, it is necessary to achieve sufficient thermal decoupling of the heated active elements from the tool frame. In this regard,

the previous study of Nürnberg [NUER10] showed the availability of insulation plate in detail.

The thermo-mechanical simulation of the ECAP tool is performed with the commercial FE Program Abaqus v6.12 (Dassault Systèmes Simulia Corp.). To simplify the discretization of the FE model and reduce the number of elements, all holes and attachments are not considered, which have indirect influence on the heat flows. The 2D simulation of the tool active elements is performed under plane strain conditions. The physical characteristics of the materials are based on the data sheets of the suppliers and literatures (Appendix Table 9.2 and Equation 9.1).

In Figure 3.7 (a), the temperature of the channel parts reaches 225 °C after 1.5 h as a stationary state. This shows that the thermal decoupling of the tool is sufficiently ensured by the insulation plates with a thickness of 15 mm. The process heat is concentrated exclusively on heating the channel part. Consequently, this locally intensive heating results in the displacement of both channel elements in the opposite direction of the x-axis due to the thermal expansion as described in Figure 3.7 (b). Based on the simulation result and analytical calculation, the initial dimension of the channel part is downsized, particularly in the x-direction.

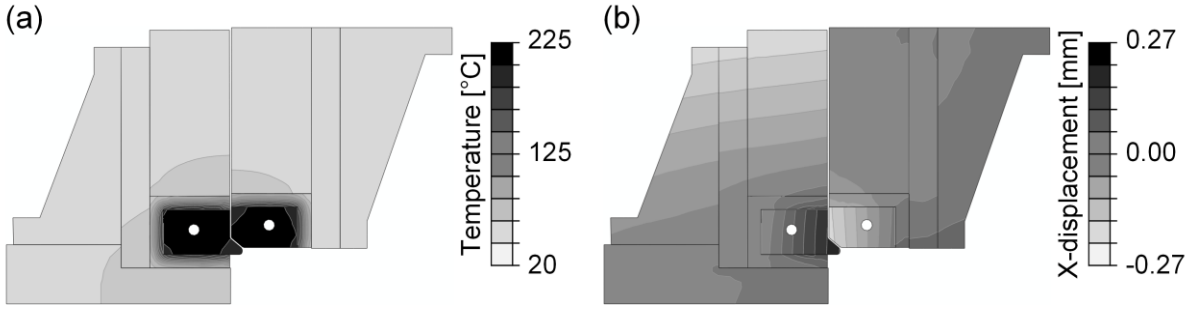

Figure 3.7: Simulation results at processing temperature of 225 °C after 1.5 h in cross section of tool active elements: (a) Temperature distribution, (b) Displacement in x-direction due to thermal expansion

The functionality of the developed concept is demonstrated by the simulation model. The experimental measurements confirm these simulation results. After the fabrication and assembly of the test tool, the temperature measurements are carried out to verify the thermal design calculations. Particular attention is paid to the temperature distribution in the insulation plates. As the temperatures of the channel part are regulated by

the hotcontrol® temperature controller to the target temperature of e.g. 225 °C and reach a state of saturation actually after 1.5 h, the marked points on the side of the active elements are measured using a tactile thermometer (Figure 3.8). The calculated temperatures at the passage part are lower and at insulation plates higher than the measurement results, respectively. Since the holes and bolts are neglected in the simulation model, the insulation works especially well, and hence the surrounding elements have relative low temperatures. In general, the predicted temperatures are in a good agreement with the temperature measurements. In this respect, one key objective of the tool concept is achieved.

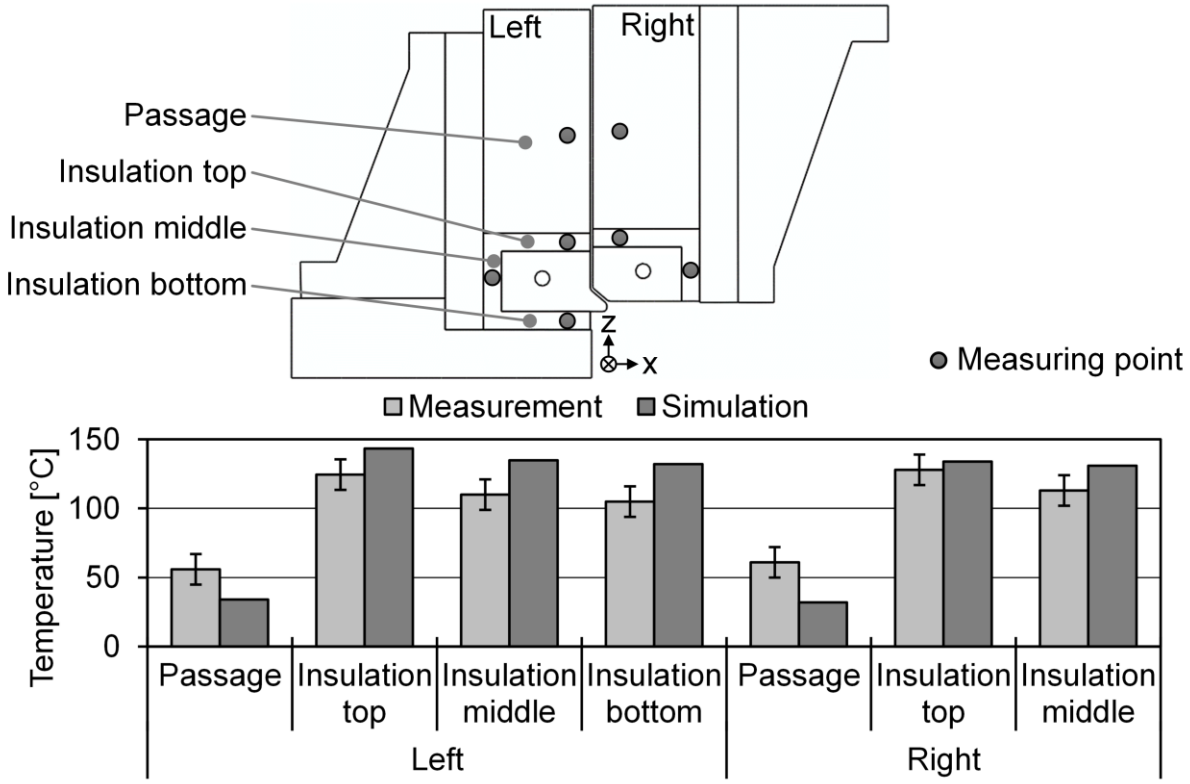

Figure 3.8: Verification of simulation-based thermal design in comparison with measurement results at processing temperature of 225 °C

Figure 3.9 shows the measured and calculated process force and temperatures with the press speed of 5 mm/s. The heated ECAP process can be well understood with this diagram. At first, it takes about 10-15 s to insert AZ31 sheet into the gap between the tool active elements and to stand ready for operation of the press. Then, the blank holder plate moves down with the constant speed. After ca. 7 s, it contacts the sheet and the actual forming process starts. Because the stamp pushes the sheet through

the entrance of the channel part by force, the peak point marks the beginning of the process. On this point, the sheet has to reach the set temperature. The measured temperature curves show the temperature reduction of 5-10 °C at the right and left channel part. Afterwards, the channel part is heated to a temperature of ca. 217 °C as a stationary state. On the other hand, after the insertion of the sheet, the calculated temperature of the right channel element is reduced drastically to a temperature of 195 °C. This is due to the large contact of the right channel element with the sheet as depicted in Figure 3.9. During the processing, the temperature rises again similar to the measured temperature until the blank holder plate opens. It is noted that additional deformation heat is introduced into the sheet by the intensive shear deformation along the channel radii. Therefore, the locally dominant temperature in the intersected shear plane can be significantly higher than predicted.

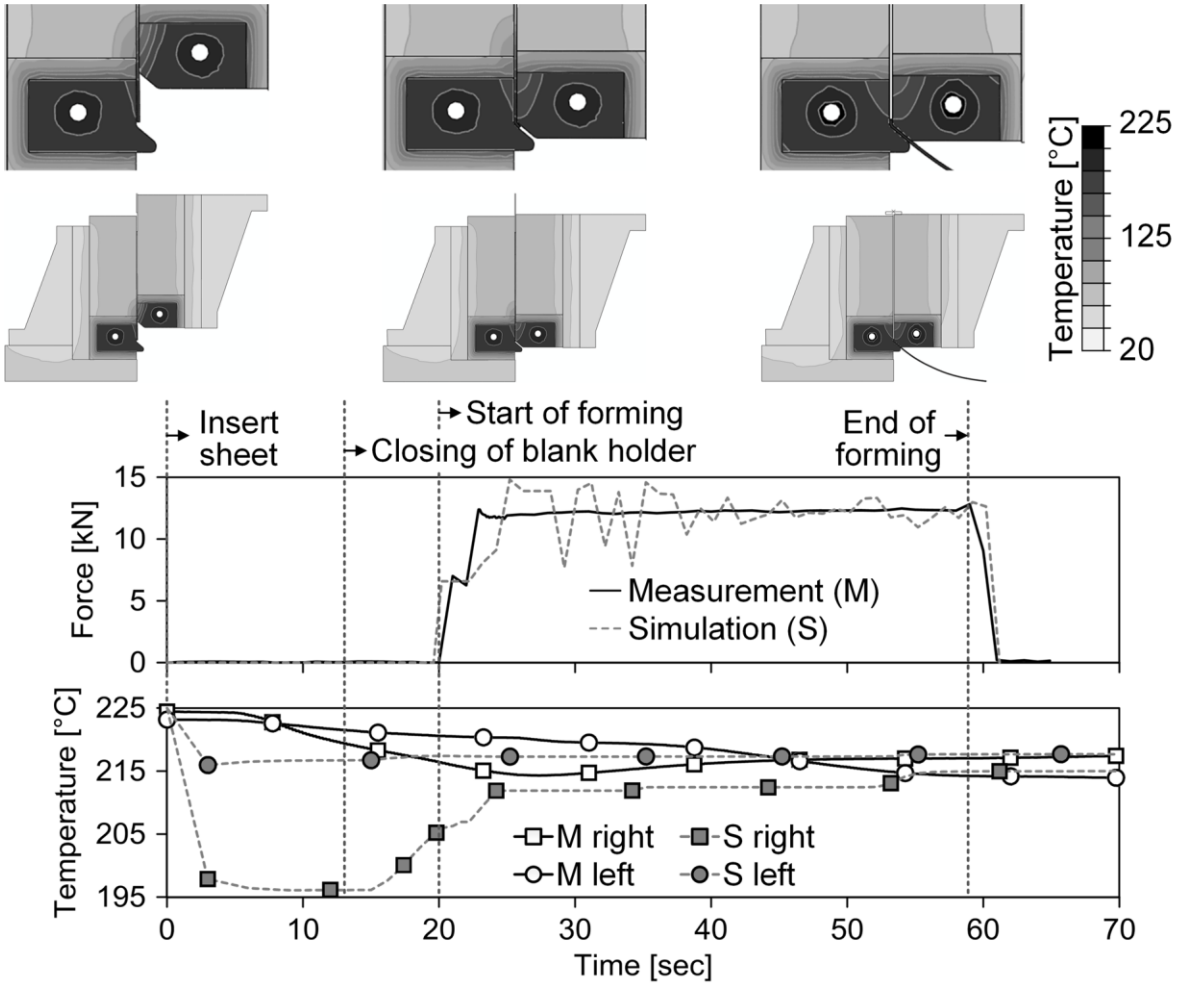

Figure 3.9: Diagram of measured and simulation-based force and temperatures at processing temperature of 225 °C

3.3 Furnace for hot straightening

The ECAPed sheets are bent due to the asymmetrical shear deformation. For the homogenization and the achievement of completely flat ECAPed sheets, a hot straightening process is necessary. Hence, a laboratory furnace Heraeus T5042 EK (Heraeus Holding GmbH) is employed. It provides the maximal heating temperature of 300 °C and inner working space of 394 × 305 × 394 mm^3. In this space, the ECAPed sheet is located between two flat steel plates and the extra block is mounted on the upper plate. The total weight of the upper plate and extra block amounts to 32 kg.

3.4 Tool for forming test of a U-shaped channel

For the forming tests of a U-shaped channel with the ECAPed AZ31 sheets, a deep drawing tool for round cup-shaped components is utilized and mounted in the hydraulic C-frame Press Typ TEZ 40 B (section 3.1). The punch diameter and punch radius amounts to 80 and 5 mm, respectively. The gap between the punch and die is 2.3 mm and its die radius is 10 mm.

3.5 Measuring equipment

3.5.1 Universal testing machine

A universal testing machine of Typ 1484/DUPS-M (Zwick GmbH & Co. KG) is available for the determination of tensile properties at room temperature under uniaxial load. This testing facility provides a maximum tolerance of 0.05% of the nominal force for the measuring range between 0.4 and 200 kN. The Zwick sensor arm extensometer in conjunction with the incremental reduction-in-width monitor is designed for the tactile measurement of width and length variation with a high accuracy of grade 1. The measurement data are automatically connected with the software testXpert® II v3.0.

3.5.2 Sheet metal testing machine

Nakajima test is carried out to determine forming limit curve (FLC) of sheet metal materials using a sheet metal testing machine (Typ BUP 1000, Zwick GmbH & Co. KG).

With the forming limit curves, sheet formability is evaluated in the range from the uniaxial to biaxial strain condition. This testing machine is available with maximal pressing force and clamping force of 1000 kN (refer to Table 3.3). The diameter of the hemispherical punch is 100 mm for a flat sheet metal blank with a diameter of 250 mm. The measurement data are automatically connected with the software testXpert® II v3.6. During the Nakajima test, an optical 3D deformation measurement system ARAMIS 4M (GOM mbH) acquires and evaluates the entire image sequence from the beginning of the deformation up to the fracture. This system provides the frame rate up to 168 Hz, camera resolution of 2400 × 1728 pixel and strain measuring range from 0.005 up to 2000% with the measuring accuracy up to 0.005%. The testing and evaluation procedure are carried out using the ARAMIS software v6.3.0 following ISO 12004.

Parameter	***Value***	***Unit***
Maximum pressing force	*1000*	*kN*
Maximum clamping force	*1000*	*kN*
Maximum deep drawing speed	*750*	*mm/min*
Maximum ram stroke	*150*	*mm*
Maximum outer diameter of die	*250*	*mm*
Maximum diameter of hemispherical punch	*100*	*mm*
Maximum sheet metal strip width	*260*	*mm*
Maximum sheet metal strip thickness	*10*	*mm*

Table 3.3: Technical data of sheet metal testing machine Typ BUP 1000

3.5.3 Optical microscope

For light micrograph, a light optical microscope Leica DMI 5000 (Leica Microsystems GmbH) is available. This microscope offers reflected light and transmitted light examinations with manual stage, motorized objective turret, motorized focus and a DFC280 camera. The image resolutions extend from 1.3 to 12 mega pixels at a color depth of up to 14 bits per color channel [LEIC14].

3.5.4 Electron backscatter diffraction (EBSD)

Electron Backscatter Diffraction (EBSD) can provide a more complete description of crystallographic properties such as grain size, grain orientation, misorientation and texture. For this, ULTRA 55 (Carl Zeiss Microscopy GmbH) of field emission scanning electron microscopes (FE-SEM) delivers advanced analytical microscopy. It provides low voltage imaging and stability, resolving structures as small as 1.5 nm. The large image frame store combined with high speed electron beam scanning permits the rapid (50 ns per pixel) and quantitative elemental mapping of high resolution fields of view with 12000 × 9000 pixels [ZEIS14].

3.5.5 X-ray diffraction (XRD)

An X-ray diffractometer X'Pert PRO system (PANalytical B.V.) is available for the measurement of global texture. In this system, the goniometer has an angular resolution of minimum step size in θ and 2θ of 0.001° and radius of 320 mm. A ceramic 50 kV X-ray tube is mounted onto the goniometer in a tube shield. This system provides phase determination, texture analysis and internal stress analysis [PANA14].

4 Test Material

4.1 AZ31 magnesium alloy sheet

The present study investigated the possibility for the application of ECAP process to commercial AZ31 Mg sheets. AZ31 Mg sheet is one of the most widely used Mg sheets for industrial application. Especially, this alloy shows a strong basal-type texture after rolling [STYC04]. For this reason, the influence of ECAP on the microstructural development and resulting mechanical properties can be easily detected and analyzed.

Commercial AZ31 (3Al-1Zn-0.3Mn-Mg Bal. wt.%) sheets with an initial thickness of 2 mm were rolled to a final thickness of 1.8 mm at 400 °C in a single pass. This additional rolling pass was performed to refine the microstructure further. A recrystallization annealing treatment was carried out at 350 °C for 30 min, in order to provide a homogeneous microstructure with equiaxed grains for the subsequent ECAP process [SUH15]. The as-rolled AZ31 sheets were supplied by the Magnesium Innovation Centre (MagIC) at Helmholtz-Zentrum Geesthacht (HZG) as the project partner in the joint research project financed by Deutsche Forschungsgemeinschaft (DFG).

4.2 Microstructure at room temperature

The rolled AZ31 sheet exhibits a coarse-grained microstructure with an average grain size (d) of 15.4 ± 3.7 µm as depicted in Figure 4.1 (a). It shows equiaxed grain structure and elongated grains without twins. Figure 4.1 (b) displays a strong deformation texture, which is the recalculated (0001) pole figure obtained from XRD measurement. As the primary slip plane in Mg, this basal texture has a maximum pole intensity (I_{max}) of 9.5 in multiple random distribution (m.r.d.), which is characterized by the alignment of basal planes parallel to the sheet plane. The texture shows a spread of basal pole towards the RD and a markedly angular distribution towards the TD. On one hand, an orientation to the RD indicates a distinctive activity of <c+a> slip operative during the deformation [AGNE01]. On the other hand, an enhanced activation of prismatic <a> slip contributes broader angular distribution of basal planes to the TD [HUAN13, MACK08]. The texture development depends on the factors such as rolling reduction [PERE04], rolling temperature [PHIL94] and initial texture [STYC04]. In particular, the

reduction on the CRSS with increasing temperature facilitates the activation of non-basal slip such as prismatic <a> slip and pyramidal <c+a> slip [PART67]. Based on this, the applied rolling temperature of 400 °C makes either prismatic or pyramidal slip active during the rolling.

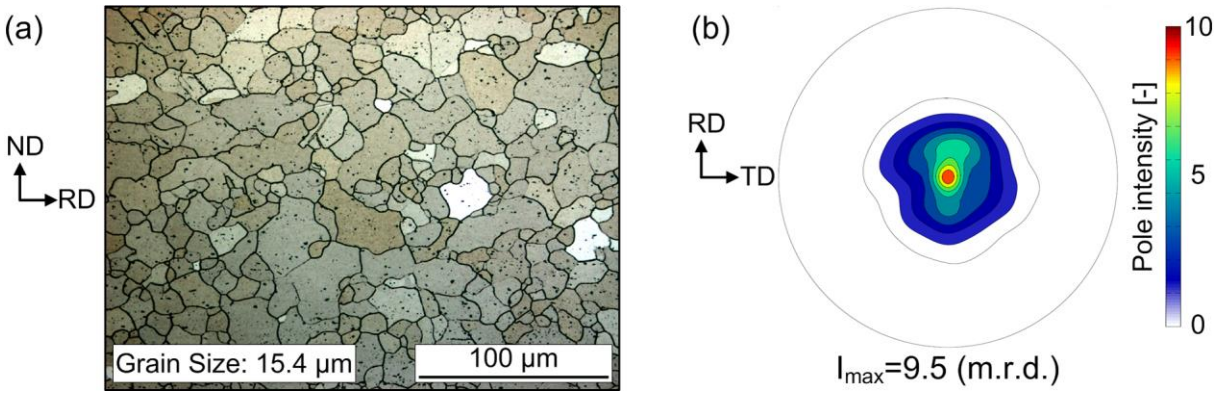

Figure 4.1: Microstructure and its associated global texture of rolled AZ31 sheet: (a) optical microstructure, (b) (0001) pole figure

4.3 Mechanical properties at room temperature

Figure 4.2 (a) describes the engineering stress-strain curves of the rolled AZ31 sheet at room temperature in terms of the loading direction (RD, 45° and TD). The corresponding tensile properties are listed in Table 4.1. This sample exhibits in-plane anisotropy in the YS and uniform elongation (ε_u), while the UTS and r-value are not significantly affected by the sample orientation. The YS is highest in the RD and lowest at 45°. By contrast, the ε_u and r-value are highest at 45°, but lowest in the RD. It is noticeable that there is a relative large difference in mechanical behavior between the RD and 45°, while the differences between the 45° and TD are less significant. This is due to the relative broad spread of the basal planes towards the TD. This angular distribution eases the activation of basal <a> slip during the loading in the TD as compared with the RD. For this reason, there is a difference in the mechanical properties between the present test sample and a typical AZ31 alloy. A typical basal texture of AZ31 shows that the basal poles are tilted more broadly to the RD than to the TD as mentioned in Figure 2.8 (a). As a result, the YS and r-value increase gradually from the RD to the TD as reported by [KAIS03, YI10]. From this point of view, it follows that the initial texture is one of the most important factors that has a remarkable effect on the forming properties of Mg alloys.

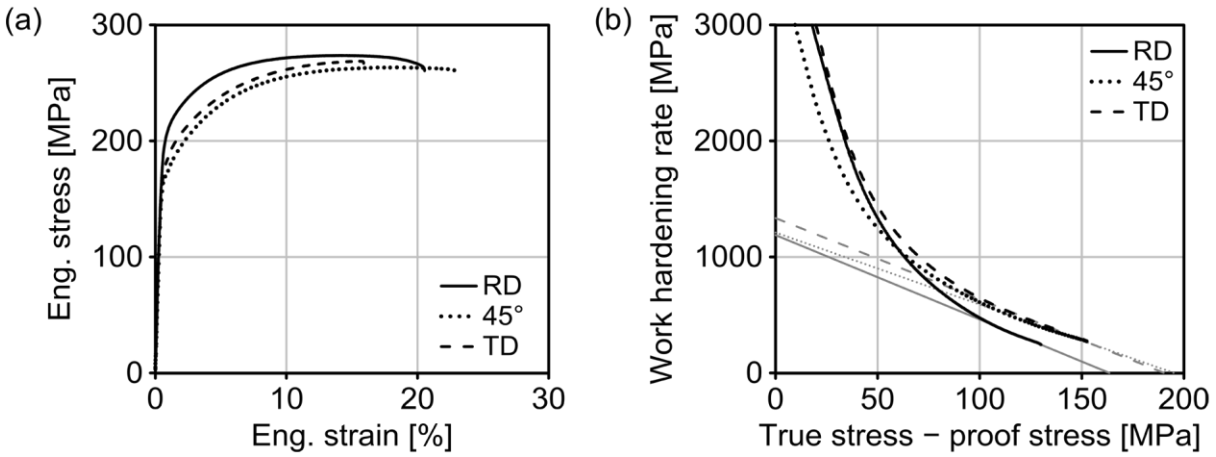

Figure 4.2: (a) stress-strain curve at room temperature of rolled AZ31 sheet, (b) corresponding work hardening rate as a function of $\sigma - \sigma_{0.2}$

Tensile direction	***YS [MPa]***	***UTS [MPa]***	***ε_u [%]***	***ε_f [%]***	***r-value at ε=10% [-]***	***n-value [-]***
RD	*190*	*275*	*13.4*	*19.4*	*1.59*	*0.13*
45°	*167*	*264*	*17.4*	*22.0*	*1.87*	*0.17*
TD	*171*	*269*	*14.8*	*15.7*	*1.73*	*0.17*

Table 4.1: Room temperature tensile properties of rolled AZ31 sheet

Figure 4.2 (b) shows the macroscopic work hardening rate Θ of the rolled sheet in the RD, 45° and TD as a function of $\sigma - \sigma_{0.2}$, where σ, and $\sigma_{0.2}$ are true stress and proof stress, respectively. The $\sigma - \sigma_{0.2}$ is related to the dislocation contribution to the flow stress [VALL06]. As mentioned above, no linear hardening (stage II) is observed in all tensile directions. Instead, the hardening rate decreases linearly with increasing σ after the elasto-plastic transition (transition from stage I to stage III).

The Θ in the TD and 45° is comparable, while the gentlest slope and the largest transition section are observed at 45°. By contrast, the rapid transition in the RD leads to a steep drop in the Θ. That is, the work hardening effect is stronger in the TD and 45° after the yielding, and dynamic recovery is more suppressed than in the RD. In a related development, the n-value in the TD and 45° is 0.17 as compared to 0.13 in the RD. High n-value leads to a low sensitivity to the strain localization and is responsible for the increase in the uniform elongation, which is known to be equivalent to the n-value at the point of the maximum load [HUAN08].

The highest uniform strain is measured at 45°. It can be explained that the suppressed dynamic recovery at 45° supports a high working hardening rate. This results in a relative high resistance against the strain instability and hence improves the uniform elongation. On the other hand, a relative large post-uniform elongation (from uniform strain to fracture strain) is observed in the RD. This indicates that the dynamic recovery may contribute to the increase in the post-uniform elongation, which is known to be affected by the strain rate sensitivity [HUAN08].

5 Experimental Procedures

5.1 Experimental plan

The experimental plan described in Figure 5.1 represents the procedure for the enhancement of the cold formability of AZ31 Mg sheet using ECAP.

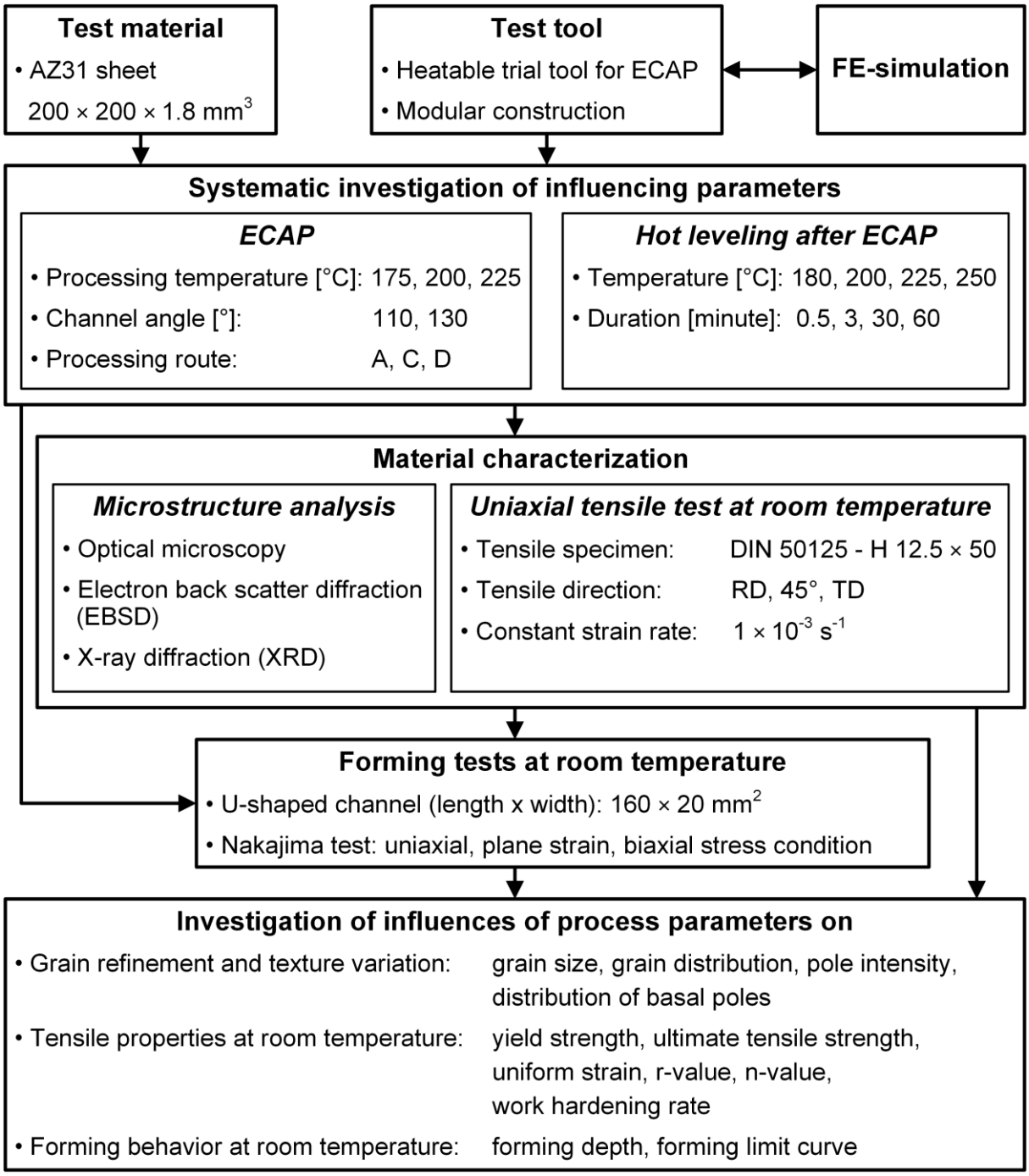

Figure 5.1: Experimental plan

5.2 Process parameters for ECAP trials

For the investigation of the ECAP process on the microstructure development and cold formability of AZ31 sheets, the ECAP processes are carried out with the following defined process parameters in the developed test tool.

5.2.1 Processing temperature

The processing temperature is a key factor in ECAP, because it can be controlled relatively easily [VALI06]. Increasing temperature facilitates the activation of slip systems due to the reduction of the CRSS. For this reason, Mg alloys are often processed by ECAP in the temperature range from 175 to 325 °C [FIGU10-1]. Especially, 200 °C is proposed as the minimum temperature for the successful deep drawing with AZ31 sheet [YI10]. This temperature represents a typical temperature for the processing of Mg alloys by ECAP [FIGU10-2]. Based on this, three processing temperatures are set as 175, 200, and 225 °C for the reduction of the energy consumption. During ECAP, the sheet and active elements are lubricated with the water-soluble lubricant (Statac BD 146, Finke Mineralölwerk GmbH) in consideration of the surface contamination. In a single pass of ECAP, the RD of the AZ31 sheets is parallel to the PD.

5.2.2 Channel angle

The channel angle is the most significant factor, since it determines directly the amount of the shear deformation in each pass. A change in the channel angle influences the characteristics of the ECAPed microstructure due to the different orientations of the shear planes and the different strains [FIGU10-2]. Earlier experiments with bar types of Mg alloys were performed in the channel angle range between 90° and 120° [MUKA01, FURU02]. In order to prevent unexpected premature failure of Mg sheets during ECAP, the tests are conducted first with two channel angles of $\Phi = 110°$ and 130°. Here the corresponding arc angle Ψ is 70° and 50°, respectively (see Figure 5.2). The effective strain per pass in the channel part with $\Phi = 110°$ and 130° amounts to ~0.8 and ~0.5, respectively.

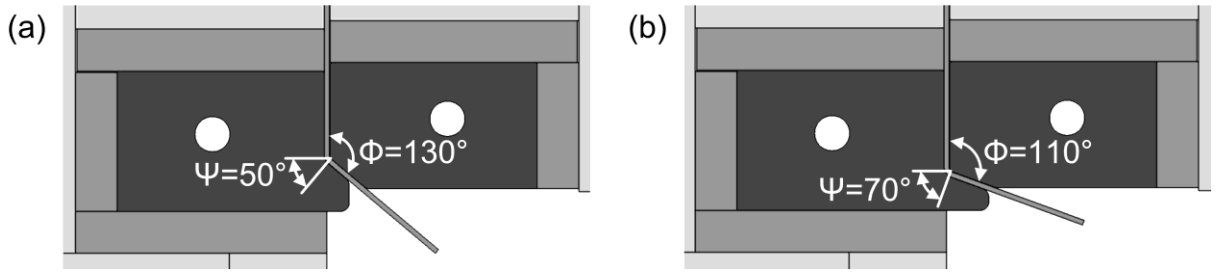

Figure 5.2: Schematic representation of channel angle Φ and arc angle Ψ: (a) Φ = 130°and Ψ = 50°, (b) Φ = 110° and Ψ = 70°

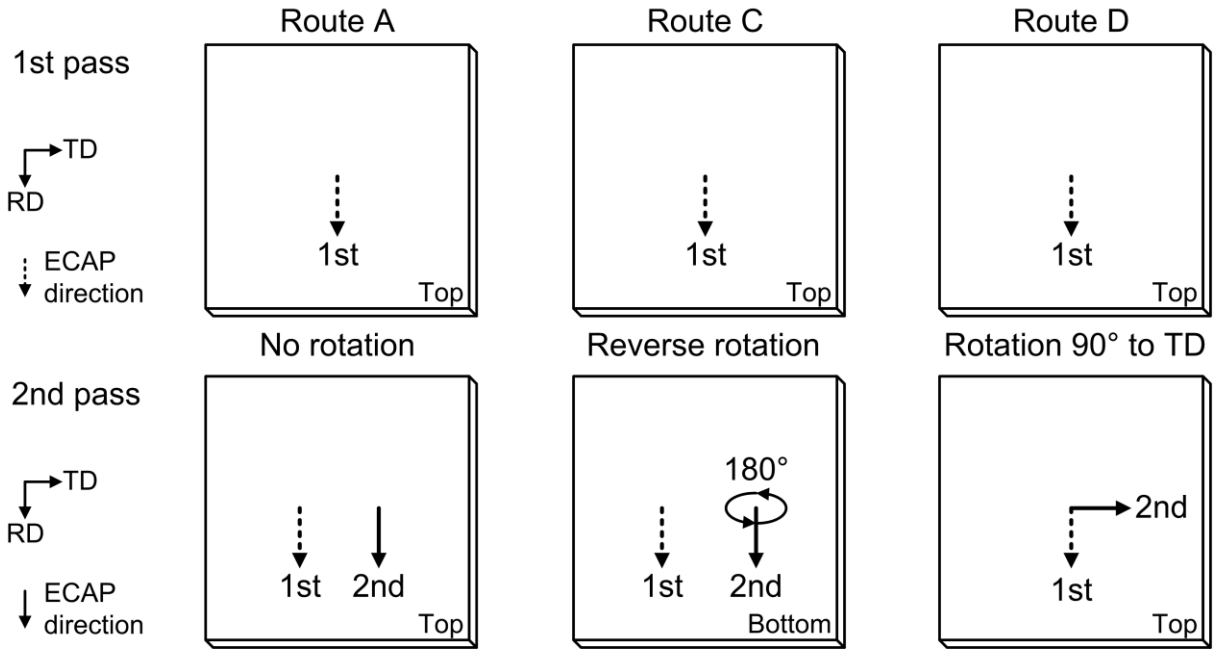

Figure 5.3: Definition of processing route for application to sheets

5.2.3 Processing route

Different slip systems and shear patterns are essentially associated with the four fundamental processing routes A, B_A, B_C and C (refer to section 2.2.1). However, routes B_A and B_C can be applied only to rectangular bar-type specimens. In the present study, the influence of the processing routes on the ECAPed microstructure and resulting mechanical and forming behavior is investigated with three routes A, C and D as illustrated in Figure 5.3. In the first pass, the PD is parallel to the RD. On route A, there is no rotation of the sheet between each pass. Thus, ECAP is performed on the same surface and same direction. On route C, the sheet is rotated by 180° to the opposite side and the PD is identical with the previous PD. Route D is the modified one of route B in consideration of the pronounced anisotropic behavior of Mg alloys. Hereby the

sheet is rotated by 90° in the plane at the second pass, and hence the PD is parallel to the TD [FERR04]. Therefore, it is expected that the ECAP effect comes into the RD and TD in the sheet plane on route D.

5.3 Hot straightening

After ECAP, the ECAPed sheets are bent due to the asymmetrical shear deformation. Hence, hot straightening process is necessary to obtain homogeneous microstructure and fully flat ECAPed sheets. For this, in the laboratory furnace Heraeus T5042 EK (Heraeus Holding GmbH), the ECAPed sheet is located between two flat steel plates and the extra block is mounted on the upper plate. As the total weight of the upper plate and extra block amounts to 32 kg, the ECAPed sheet is hot leveled with a pressure of 7.3 kPa. In particular, the microstructures of ECAPed sheets are influenced directly by temperature and duration during hot leveling process. Therefore, the microstructural stability analysis is implemented with different homogenization conditions such as at temperatures of 180, 200, 225 and 250 °C for times of 0.5, 3, 30 and 60 min. Based on this, hot straightening is performed on the ECAPed sheets.

5.4 Material characterization

5.4.1 Microstructure analysis

Microstructures of the rolled and ECAPed sheets are analyzed by optical microscopy and EBSD in the field emission gun scanning electron microscope (Zeiss™ Ultra 55) equipped with the EDAX/TSL EBSD system with a Hikari detector. Samples are cut parallel to the rolling and pressing direction. They are mechanically ground with SiC paper (grit 800-2500) and polished with oxide polishing suspension of 0.05 µm. The polished samples are chemically etched with a picric acid solution (150 ml of ethanol, 40 ml distilled water, 6.5 ml acetic acid and 3-4 g picric acid). The average grain size of the optical microstructures is determined by the linear intercept method using the Olympus™ Analysis Pro 5.0 software [SUH16-1].

In case of the EBSD samples, after the grinding process, electrochemical polishing is carried out using a Struers^{TM} AC2 solution at 16 V for 80 s at -25 °C. EBSD measurements are carried out at an accelerating voltage of 15 kV and a step size of 0.3 µm over an area of 150 × 300 µm^2. SEM investigation is performed for the observation of the fracture surfaces after Nakajima tests. Energy dispersive X-ray spectroscopy (EDS) is employed to measure the composition of segregation particles in the fracture surfaces [SUH16-2].

Quantitative texture measurements on both rolled and ECAPed samples are implemented with the Panalytical^{TM} X-ray diffractometer in reflection geometry using Cu-Kα radiation. Six pole figures, (0001), $(10\bar{1}0)$, $(10\bar{1}1)$, $(10\bar{1}2)$, $(10\bar{1}3)$ and $(11\bar{2}0)$, are measured up to a tilt angle of 70°. The data are used to calculate the complete orientation distribution function coupled with the MTEX toolbox [HIEL08]. The results are represented in terms of the (0001) pole figure [SUH15].

5.4.2 Uniaxial tensile test at room temperature

Tensile specimens are machined according to DIN 50125 H 12.5 × 50. Following the standard DIN 10002-1, uniaxial tensile tests are performed at room temperature with a quasi-static strain rate of 1×10^{-3} s^{-1} using the universal test machine (Typ 1484/DUPS-M, Zwick GmbH & Co. KG). The tensile tests are carried out at the angles of 0° (RD), 45° and 90° (TD) between the tensile direction and the RD. During the tests, the tensile force and strains along the length and width direction are measured continuously. The plastic strain ratio is calculated within the uniform elongation. The r-value in cubic materials is calculated commonly at the elongation of 20% [GHOS84]. However, Mg alloy sheets exhibit fracture strains lower than 20%. Nebebe et al. [NEBE09] reported that the uniform elongation is observed up to 10% in AZ31 and ZE10 Mg alloys. In the present study, the r-value is calculated at 10% engineering strain in the tensile direction and is designated as r_{10}. The strain-hardening exponent (n-value) is calculated by the power law regression of the tensile test data over the strain range from 10 to 15%. The results of the tensile tests are the average values obtained from at least five stress-strain curves in each direction [SUH15].

5.5 Evaluation of cold formability

The investigation of the cold formability of the ECAPed sheets is one of the main objectives in this study. For this, the forming tests of a U-shaped channel and the Nakajima tests are carried out at room temperature. With regard to the plastic anisotropy of Mg sheets, the forming tests of a U-shaped section is performed at first. To evaluate the enhanced cold formability of the ECAPed AZ31 sheets, the Nakajima tests are carried out for the determination of their forming limit curves.

5.5.1 U-shaped channel forming

In the forming tests of a U-shaped channel, strips with dimensions of 160 mm × 20 mm are prepared along the RD, 45° and TD regarding anisotropic forming behavior. The tests are conducted using the deep drawing test tool with a punch diameter of 80 mm (refer to section 3.4). The punch speed of 20 mm/s is constant and the blank holder force is set as zero for the maximization of the material flow between the punch and die. The whole strip and contact area of the active forming elements are lubricated with a water-soluble cooling lubricant (Statac BD 146, Finke Mineralölwerk GmbH). The forming depth of each sample is measured from the flange to the floor zone excluding the sheet thickness [SUH16-2].

5.5.2 Nakajima test for determination of forming limit curve

Figure 5.4 presents the testing and evaluation procedure for the determination of FLCs for sheet metals following ISO 12004. Nakajima tests are carried out using the sheet metal testing machine BUP 1000 (Zwick GmbH & Co. KG). Here the flat sheet metal blanks are mechanically deformed by a hemispherical punch with diameter of 100 mm. A forming die has a diameter of 105 mm and corner radius of 10 mm. The punch speed is 1 mm/s and the blank holder force is 300 kN. A draw ring bead is not used, because a sharp bead radius causes unexpected failure in the contact area between bead and Mg sheets due to low formability. The punch and specimen are lubricated by the combination of oil and two circular blanks made from PVC, in order that the specimens are fractured in the center of the dome.

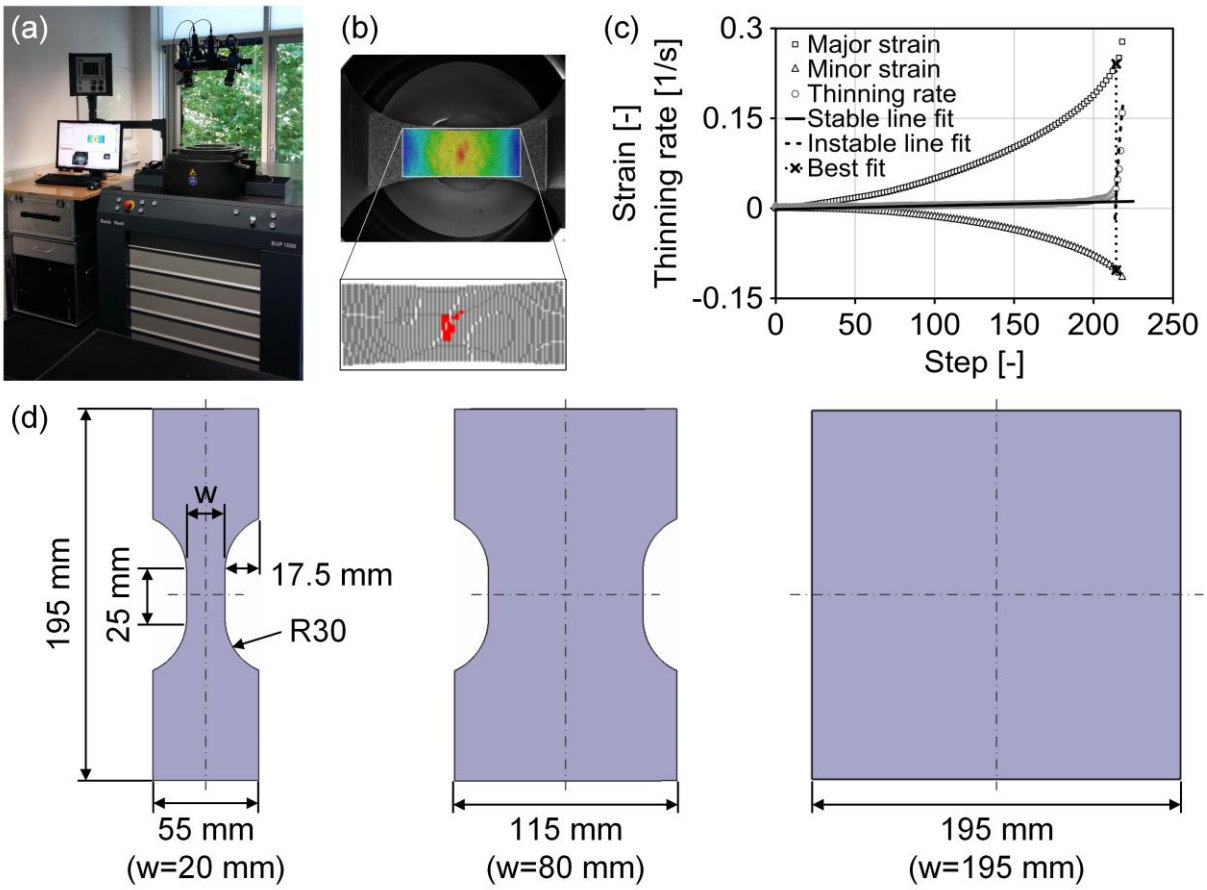

Figure 5.4: Description of Nakajima test and time dependent evaluation method: (a) sheet metal test machine, (b) major strain distribution before failure and thinning gradient of necking zone, (c) time dependent evaluation method, (d) geometry dimensions of three specimens for different strain conditions [SUH16-2]

During the test, the optical 3D measurement system ARAMIS 4M (GOM mbH) acquires the full sequence from the beginning of the deformation up to the fracture with a recording frequency of 10 Hz. For this, the specimens are prepared with a stochastic pattern using black and white spray. Three specimen geometries are milled as illustrated in Figure 5.4 (d), to derive forming states from uniaxial to biaxial strain conditions. The Nakajima tests are performed with three repetitions of each geometry [SUH16-2].

The so-called time based evaluation method [VOLK10] is applied to the calculation of forming limit values for the FLC. The concentration of the remaining plastic deformation in small shear bands will lead to high thinning rates, while the thinning rates outside the shear bands will stay nearly constant. In the second stage before the specimen

failure, the thinning rate is calculated using the volume constancy form the major and minor strains. Figure 5.4 (b) shows the marked area with the largest thinning rate values, where can be understood as the area of local necking. Figure 5.4 (c) describes the principle of the linear best-fit method [VOLK12]. The local necking occurs during instable deformation and before crack initiation. The stable and instable areas are fitted with two linear trend lines using the least square method. The intersection point of these two straight lines defines the beginning instability [SUH16-2].

6 Results and Discussion

6.1 Microstructure development during a single pass

Figure 6.1 describes the ongoing ECAP process and the three samples, which are processed in a single ECAP pass with a channel angle of Φ = 130° and arc angle of Ψ = 50° at processing temperatures of 175, 200 and 225 °C. Here, the RD of the AZ31 sheet is parallel to the PD. The samples are deformed at a generally acceptable level of reliability and quality without mechanical failure, such as cracking and buckling.

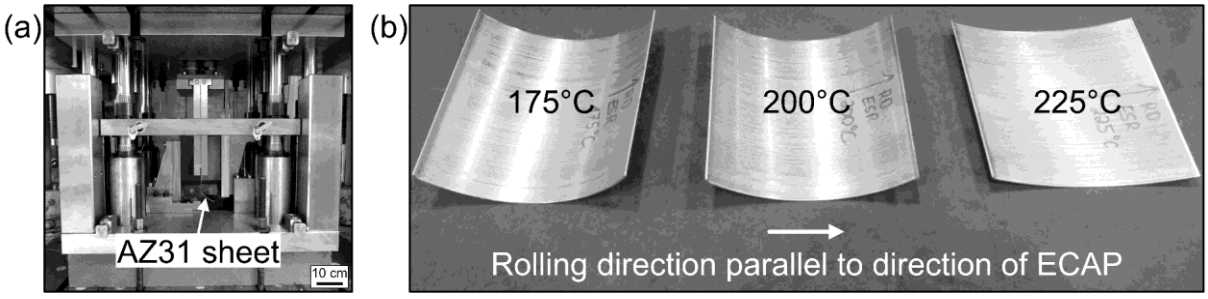

Figure 6.1: (a) ECAP process and (b) ECAPed AZ31 sheets at 175, 200 and 225 °C with Φ = 130° [SUH15]

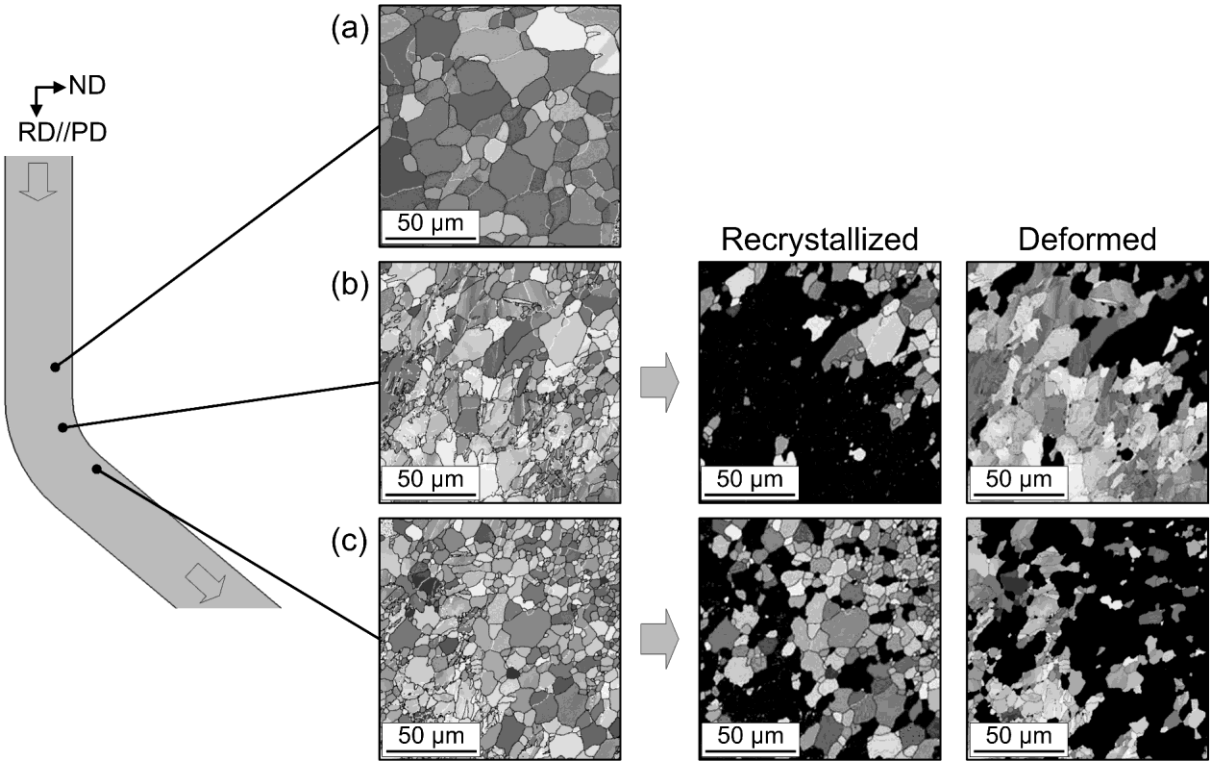

Figure 6.2: Microstructure development of AZ31 sheet during a single ECAP pass at 225 °C with Φ = 130° [VICT14-1]

In order to track the microstructure development of AZ31 sheet during ECAP with Φ = 130° at 225 °C, the microstructures on the three points are measured using EBSD as presented in Figure 6.2. This approach provides a distinction between the area fractions of the deformed and recrystallized microstructure before and after a single ECAP pass. Figure 6.2 (a) shows the initial equiaxed microstructure of AZ31 sheet before entering the shear plane. At the intersection plane of the channel part, dislocation slip and twinning become active as depicted in Figure 6.2 (b). The area fraction of small grains now increases and the fraction of coarse grains decreases significantly. Moreover, some coarse grains of above 10 µm are visibly distorted and surrounded by finer grains. This is due to the activation of dynamic recrystallization and recovery. Figure 6.2 (c) presents that fine grains develop more and the area fraction of largely deformed grains left still after processing.

Grain refinement in Mg alloys by ECAP is based on the formation of new grains along the original grain boundaries in a necklace-like manner by dynamic recrystallization [FIGU09-1]. At dynamic recrystallization, the grains nucleate preferentially along the original boundaries of the coarse-grained structure and along twin boundaries in a necklace-like pattern. Hence, the inner cores of the coarse grains may not be refined [FIGU10-1]. This microstructure development during ECAP is consistent with the observations of previous studies using transmission electron microscopy (TEM) [DING09], optical microscopy [FIGU09-1] and EBSD [FIGU09-2].

6.2 Analysis of microstructure stability at hot straightening

After ECAP process, the ECAPed sheets are bent due to the asymmetrical shear deformation as displayed in Figure 6.1 (b). Moreover, ECAPed Mg alloys can exhibit low thermal stability, e.g. due to the presence of non-equilibrium grain boundaries [RADI10] or due to the high stored energy caused by severe plastic deformation [STRA14]. The low thermal stability leads to a limited secondary processing like forming process of Mg sheets. Therefore, it is important to analyze the microstructural instability at the post heat treatment. Since microstructure evolution directly depends on the heat treatment temperature and duration, the microstructure stability was analyzed under different annealing conditions.

Figure 6.3 shows the optical microstructures of the ECAPed AZ31 sheets, which were hot-leveled at 200 and 250 °C for 0.5, 3, 30 and 60 min, respectively. The microstructures heat-treated at 200 °C have a comparable grain size of ~8 µm and an acceptable homogeneous grain distribution regardless of the annealing time. This microstructural feature is also observed at 180 °C. On the contrary, the annealing time has a significant influence on the microstructure evolution during the heat treatment at 250 °C. The average grain size increases from 7.7 to 18.3 µm with the annealing time from 0.5 to 60 min. Such a dramatic grain growth is observed at above 225 °C and from the annealing time of 3 min. After 30 and 60 min, the existing fine grains are rapidly consumed and replaced by the nucleation and abnormal growth of new grains.

Figure 6.4 depicts the effect of the hot straightening conditions on the texture development regarding (0001) pole figure. As a representative result, the as-ECAPed condition is compared with the samples in Figure 6.3 (c), which were hot-leveled at 200 and 250 °C for 30 min, respectively. The as-ECAPed sample exhibits a low pole density and a highly tilted texture component along the RD, which originates from the activation of $\{10\bar{1}2\}$ tension twins. The shear strain induced by ECAP inclines the c-axis of the hcp structure, and hence $\{10\bar{1}2\}$ tension twinning can be easily accommodated by the tension in the c-axis. Even if the sample heat-treated at 200 °C has a negligible change in the grain size and morphology, the texture is slightly strengthened and the pronounced texture component is weakened in Figure 6.4 (b). At 250 °C, the I_{max} is extremely strengthened from 7.9 to 15.5 and the rotated components disappear as displayed in Figure 6.4 (c). That is, the ECAP effect is completely lost at 250 °C. It indicates that the fraction of the twinned microstructure has a low thermal stability. This can reduce a potential to tailor the microstructure and texture of Mg-Al-Zn alloys.

In consideration of the homogenization and thermal stability of the ECAPed sheets, the hot straightening temperature is set as 200 °C. As compared with the optical microstructure annealed for 60 min, there is no major differences in grain distribution at the annealing time of 30 min. Particularly, the bent sheets are completely leveled after 30 min. For the above reasons, the ECAPed sheets are hot straightened at 200 °C for 30 min. In the following sections, the ECAPed sheets and their material characteristics indicate the hot-leveled state in the above-determined conditions.

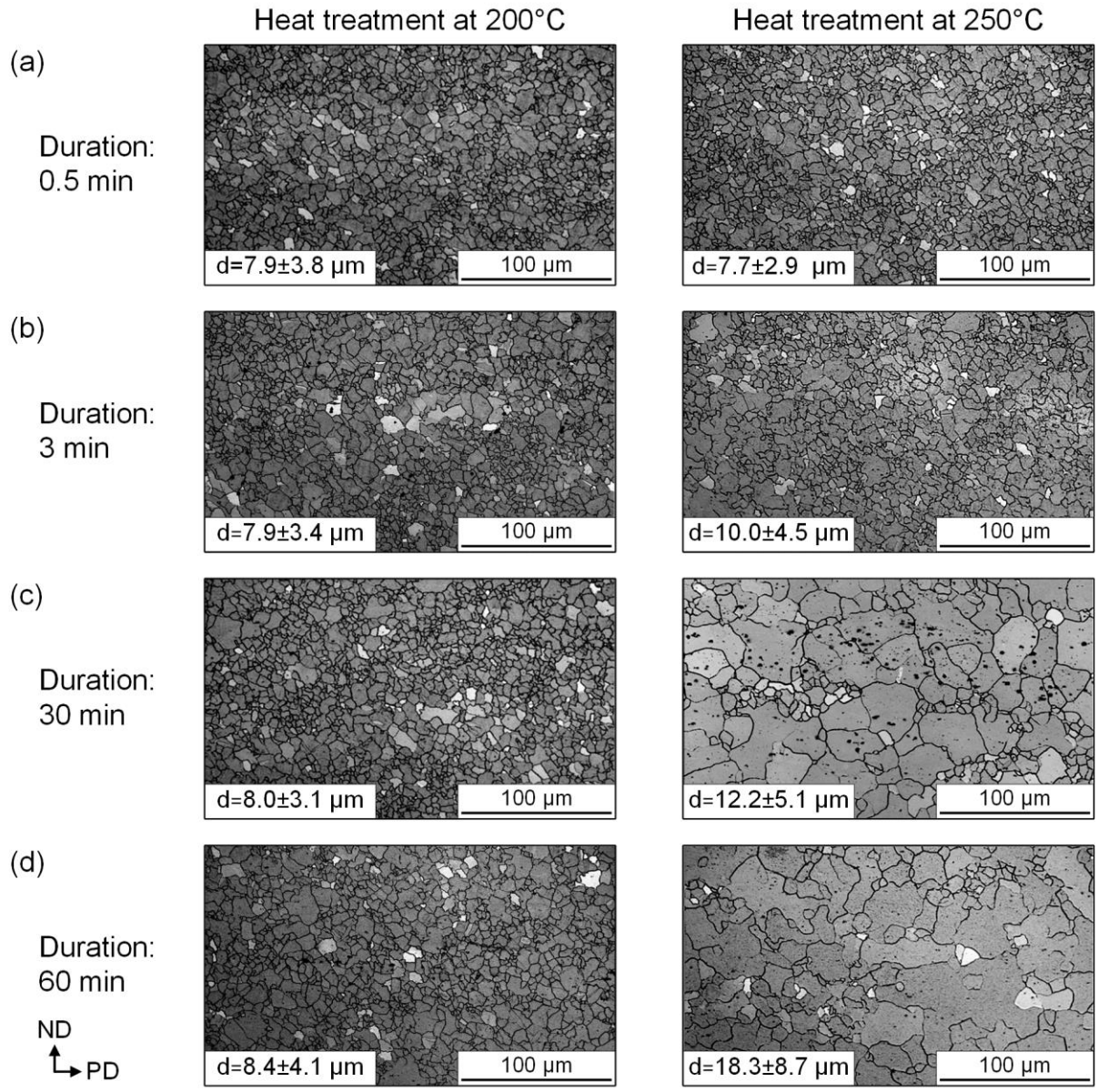

Figure 6.3: Microstructure development of ECAPed AZ31 sheets at hot straightening in terms of heat treatment temperature and duration [VICT14-2]

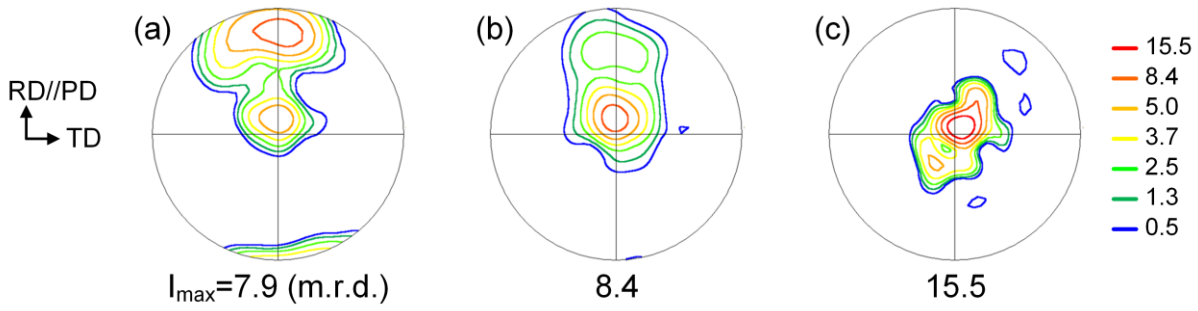

Figure 6.4: (0001) pole figure of ECAPed AZ31 sheets regarding heat treatment: (a) as-ECAPed sample, (b) sample hot-leveled at 200 °C for 30 min, (c) sample hot leveled at 250 °C for 30 min

6.3 Influence of process parameters on microstructure and texture development

6.3.1 Processing temperature

As one of the easiest controllable parameters, the effect of the processing temperature is investigated first with the fixed channel angle of Φ = 130°. Figure 6.5 displays the optical microstructures of the rolled and ECAPed AZ31 sheets at 175, 200 and 225 °C, respectively [SUH15]. In Figure 6.5 (a), the rolled sheet shows a coarse-grained microstructure with an average grain size of 15.4 ± 3.7 µm. In comparison of the initial microstructure, more homogeneous microstructures develop after a single ECAP pass at 175 and 200 °C, as depicted in Figure 6.5 (b) and (c). The average grain size of the sample processed at 175 °C is 10.5 ± 3.4 µm. The ECAPed sample at 200 °C exhibits a comparable grain size distribution and the average grain size is slightly refined to 9.4 ± 3.1 µm. Figure 6.5 (d) displays the microstructure of the ECAPed sample at 225 °C, where the microstructure is further refined to 7.6 ± 3.2 µm. As a characteristic feature, the relatively coarse grains in the ECAPed samples result from twinning, which is identified mainly as formation of $\{10\bar{1}2\}\langle 10\bar{1}1\rangle$ twins (see closed arrows). This is derived from the fact that twins can be nucleated easier in small grains, but their growth is easier in lager grains [YI05].

From the comparison of the optical microstructures, it is noteworthy that a reasonably homogeneous microstructure develops in a single ECAP pass at the three temperatures. At the ECAPed samples, the original coarse grains are consumed by the formation of fine grains along the grain boundaries. Especially, the occurrence of serrated grain boundaries and small grains, which are marked as open arrows in Figure 6.5 (d), indicates the activation of dynamic recrystallization [VICT13]. This results from the continuous production and absorption of dislocation in low angle grain boundaries, as well as the progressive transformation to high angle grain boundaries, i.e. the formation of new grains [ION82]. Since new grains tend to appear along the grain boundaries of coarse grains, new fine grains will surround them and form a necklace-type microstructure. This observation is in good agreement with the fact that fine microstructures can be produced in any material using ECAP at low temperatures [SAKA14].

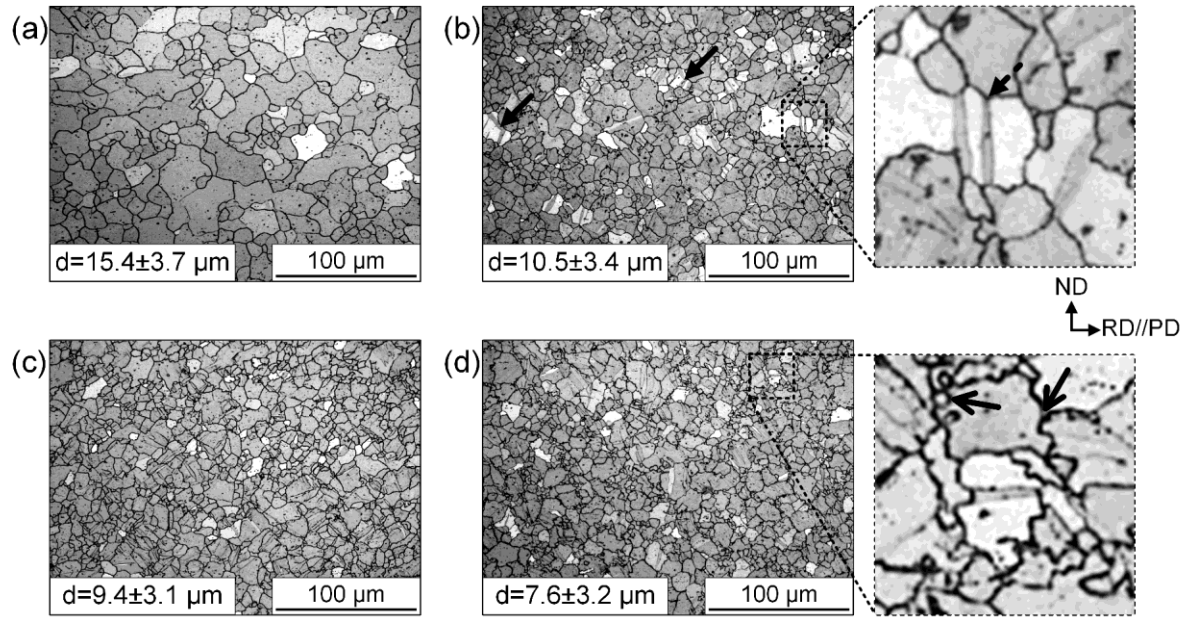

Figure 6.5: *Microstructure of rolled (a) and ECAPed AZ31 sheets with Φ = 130° at (b) 175 °C, (c) 200 °C, (d) 225 °C (closed arrows: tensile twin, open arrows: serrated grain boundaries and small grains) [SUH15]*

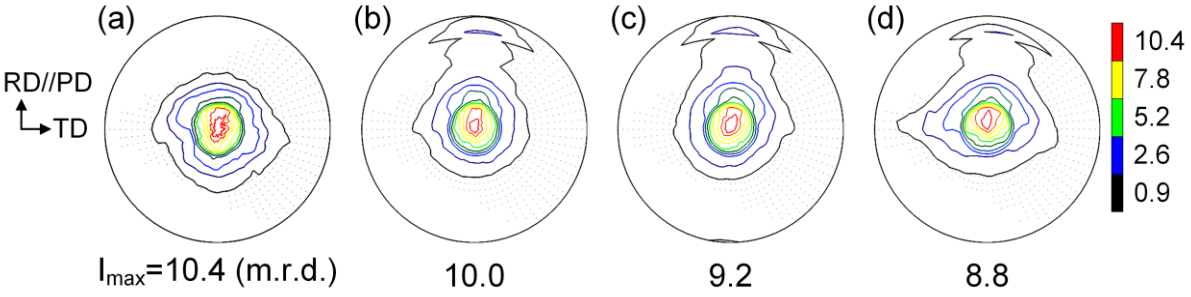

Figure 6.6: *(0001) pole figures of rolled (a) and ECAPed AZ31 sheets with Φ = 130° at (b) 175 °C, (c) 200 °C, (d) 225 °C*

With regard to the texture development, Figure 6.6 presents the recalculated (0001) pole figures of the rolled and ECAPed sheet, as obtained from XRD measurements. In Figure 6.6 (a), the rolled sheet exhibits a strong basal texture with I_{max} = 10.4. This texture is characterized by the alignment of the basal planes perpendicular to the ND. After a single ECAP pass with Φ = 130° at 175 and 200 °C, the texture intensity decreases slightly from 10.4 to 10.0 and 9.2 as shown in Figure 6.6 (b) and (c), respectively. In the ECAPed sheet at 225 °C, the texture is further weakened and the pole density is reduced to 8.8.

Especially noteworthy is the development of a new texture component, which tilts by 70-85° towards the PD in all ECAPed samples. This texture component is originated from the microstructure containing $\{10\bar{1}2\}$ $<10\bar{1}1>$ tension twins, because they can re-orient the c-axis in 86° away of the original direction [YI09]. This twinning mode is the most commonly and easily activated twin in Mg [ROBE60]. An activity promotion of certain twinning modes have a favorable effect on the weakening and randomization of the texture. More importantly, the mechanical and forming properties of many engineering alloys are directly related with the formation of twins, because they can accommodate the plastic deformation and change the orientation of the lattice [NIE13]. As the lattice is reoriented and hence the basal planes are tilted and split, one of the main effects is a high increase in the activity of basal <a> slip. In Mg, a theoretical maximum extension of 6.4% along the c-axis can be accommodated by complete reorientation of $\{10\bar{1}2\}$ $<10\bar{1}1>$ twins [PART67]. This effect can enhance the uniform elongation in Mg alloys [BARN07].

Since basal <a> slip is the easiest deformation mode at room temperature, the analysis of Schmid factor can help evaluate the influence of the reorientation of the basal planes on the activation of basal <a> slip [SUH15]. The Schmid factor is a geometrical value that indicates the feasibility to activate a determined slip mode regarding a defined direction of the applied load. Figure 6.7 (a) presents the microstructures of the rolled sheet and ECAPed sample at 225 °C regarding the Schmid factor for basal <a> slip. The data from the EBSD measurements are used to calculate the Schmid factors for basal <a> slip in tension, when loading parallel to the RD or PD. As a result, the ECAP process allows the increase in the fraction of the microstructure with a high Schmid factor of 0.4. Another important feature is that the fraction of the microstructure with high Schmid factors is increased by twinning. Some related examples are highlighted by the dashed white squares and in the close up of Figure 6.7 (a).

Figure 6.7 (b) presents the distribution of the Schmid factors for the activation of basal <a> slip, when a tension is applied along the RD and TD in the rolled and ECAPed sheets. It is abundantly evident that the ECAP process has a strong effect on the activation of basal <a> slip along the PD. Because ECAP makes rotation of the c-axis towards the PD, the slip direction is not parallel to the loading in the sheet plane. As a

result, basal <a> slip and tensile twinning can be accommodated easier by the rotated basal planes at in-plane extension. This is evident from a monotonic increase in the fraction of the microstructure with high Schmid factors in terms of relative frequency. However, there is no distinct increase in the Schmid factors of both cases under extension parallel to the TD. These results are directly involved in the directional tensile properties of the rolled and ECAPed sheets at room temperature [SUH15].

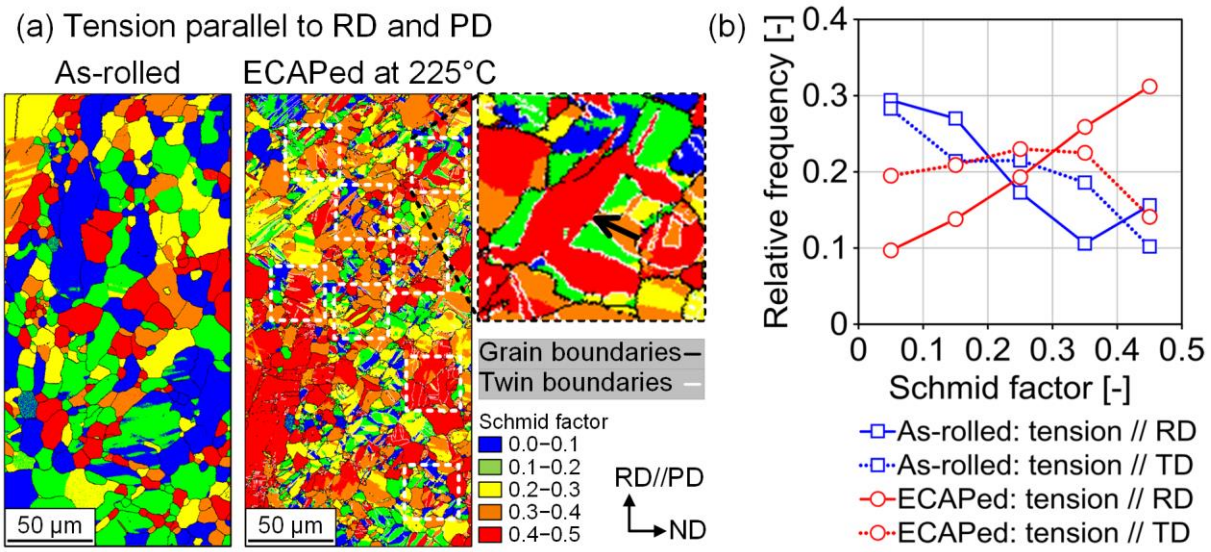

Figure 6.7: Analysis of Schmid factor for basal <a> slip of rolled and ECAPed sheet at 225 °C: (a) Schmid factor maps, (b) distribution of Schmid factors of a virtual tension along RD // PD and TD in terms of relative frequency [SUH15]

6.3.2 Channel angle

The channel angle Φ is the most significant factor that determines directly the amount of the shear deformation in each pass. In this section, its effect on the ECAPed microstructures are investigated using two channel angles of Φ = 110° and 130°. Since the AZ31 sheets processed with Φ = 130° exhibit the most refined grain and the lowest pole intensity at 225 °C, the characteristics of two channel angles are compared at 225 °C. The microstructures and textures in the middle plane of the rolled and ECAPed sheets are measured by EBSD and their global textures are measured by XRD.

Figure 6.8 presents the microstructures of the ECAPed sheets at 225 °C with Φ = 110° and 130° using EBSD IPF map, respectively. The average grain size of Φ = 110° is further refined to 8.4 ± 2.7 µm compared with Φ = 130° (d = 10 ± 4 µm). The ECAPed

microstructure with Φ = 130° exhibits several elongated grains as depicted in Figure 6.8 (b). On the other hand, the microstructure develops with higher fraction of serrated grain boundaries and fine grains at Φ = 110°. Such a grain distribution is one of the typical characteristics of dynamic recrystallization, as discussed in section 6.3.1 above. For this reason, higher shear deformation induced by lower channel angle can lead to more refined microstructure. Furthermore, the IPF map of the rolled sheet shows that most grains have (0001) axis parallel to the NR. On the contrary, many grains of the ECAPed sheets have other directions towards the RD or TD. It is evident that the shear deformation in ECAP makes the preferred orientation of AZ31 sheet to be weakened and randomized.

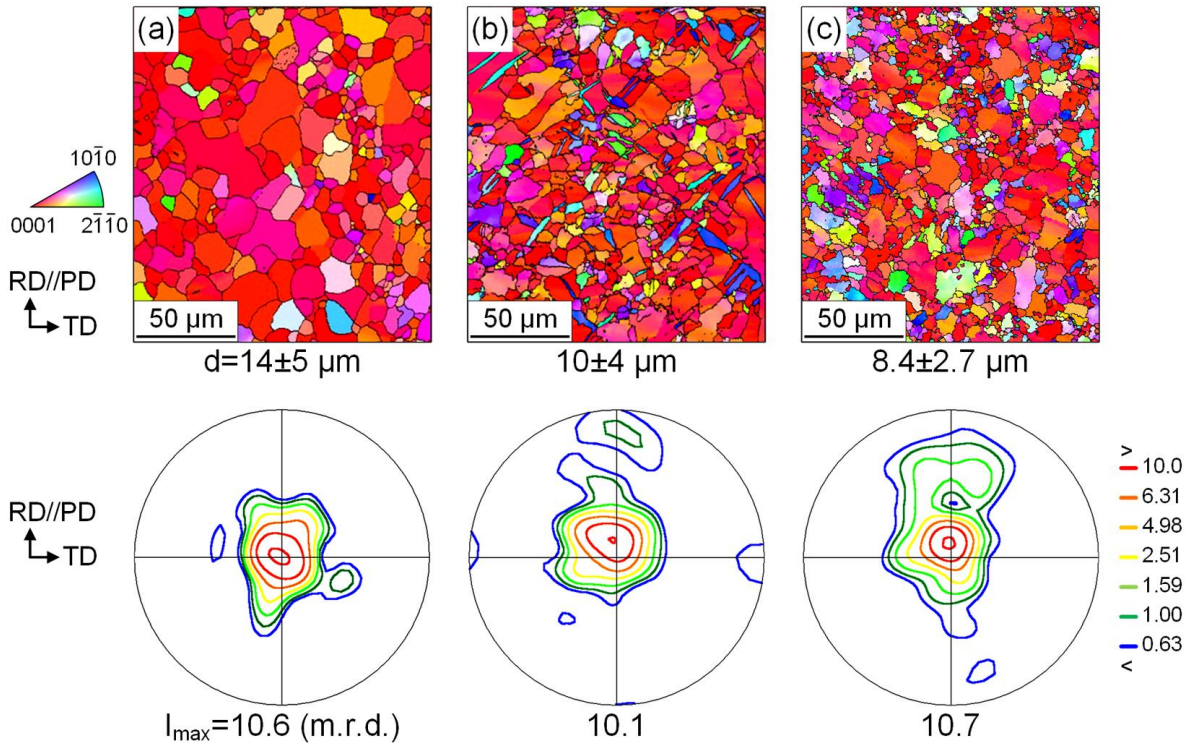

Figure 6.8: Inverse pole figure map (up) and respective local texture with (0001) pole figure (down) in terms of channel angle: (a) rolled sheet, (b) ECAPed sheet at 225 °C with Φ = 130°, (c) ECAPed sheet at 225 °C with Φ = 110°

Regarding the (0001) pole figure measured in the middle plane, there is a negligible difference in the pole density between the rolled and the ECAPed sheet with Φ = 130° and 110° (10.6 vs. 10.1 vs. 10.7). However, the local texture of Φ = 110° shows a broader angular distribution of the basal planes to the PD than that of Φ = 130°. Particularly, a new texture component develops more distinctly, tilting towards the PD.

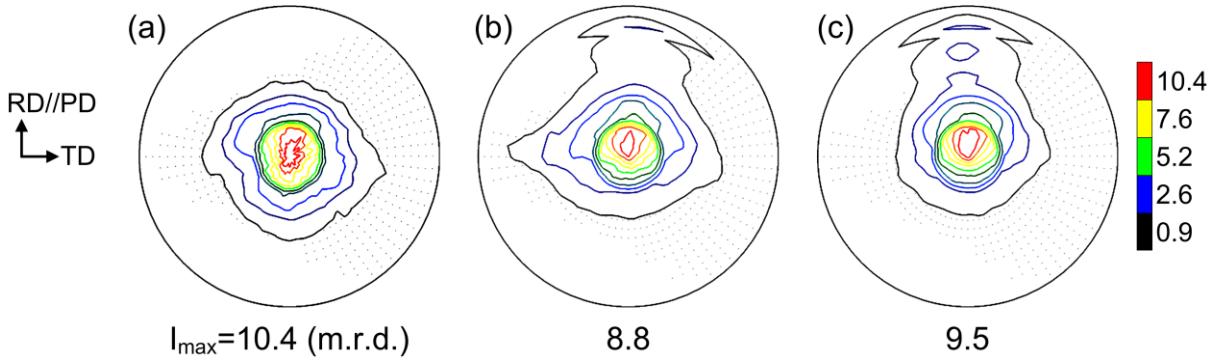

Figure 6.9: *(0001) pole figures presented as global texture for rolled and ECAPed AZ31 sheets: (a) rolled sheet, (b) ECAPed sheet at 225 °C with Φ = 130°, (c) ECAPed AZ31 sheet at 225 °C with Φ = 110°*

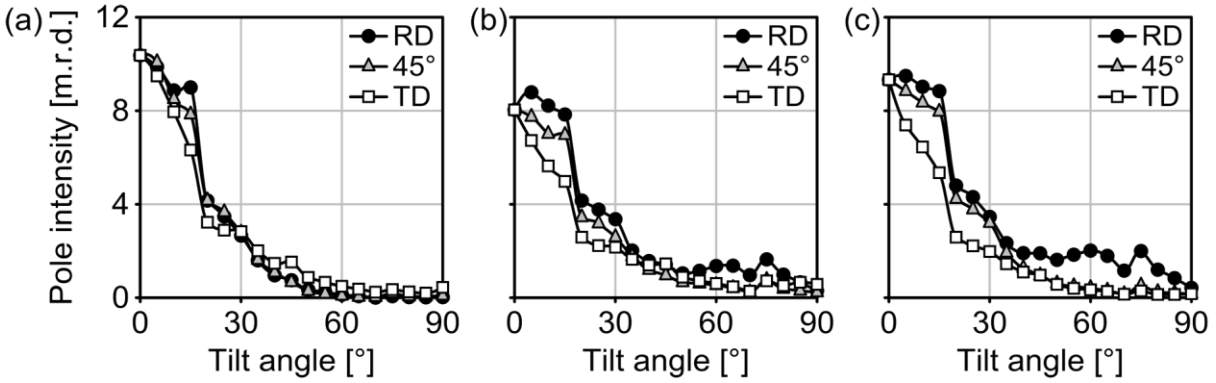

Figure 6.10: *Density profiles of the basal pole along RD and TD for rolled and ECAPed AZ31 sheets: (a) rolled sheet, (b) ECAPed sheet at 225 °C with Φ = 130°, (c) ECAPed sheet at 225 °C with Φ = 110°*

Figure 6.9 presents the global texture of the rolled sheet and ECAPed sheets at 225 °C with Φ = 110° and 130° in terms of the (0001) pole figure from the XRD measurements. Although the global texture is strengthened to 9.5 at Φ = 110°, the maximum density is weaker than the as-rolled condition. The basal poles of Φ = 130° distribute more broadly along the TD than Φ = 110°. On the contrary, there is a broader intensity spread of the basal poles at Φ = 110° from the ND towards the RD than the TD. This is evident through the comparison of the density profiles in Figure 6.10. The tilting angle of the I_{max} is ~5° in both channel angles. A further rotation of the basal poles to the RD is observed at Φ = 110°. Based on this, the local texture is in acceptable agreement with the global texture. As predicted, higher shear deformation allows more refined microstructure, higher tilting of the basal planes and more activation of tension twins

in the ECAPed sheets. This microstructural evolution can improve the mechanical behavior at room temperature of the ECAPed sheets. In this respect, the mechanical feature is described in section 6.4.2.

6.3.3 Processing route

For the investigation of the effect of processing routes, the ECAP processes are carried out with Φ = 110° and 130° at 225 °C under the three distinct processing routes A, C and D. These different processing routes are illustrated in Figure 5.3 above. In aspect of grain refinement, Figure 6.11 (a) shows that the grains are slightly refined processing through route A and C with Φ = 130°. The average grain size of route A and C is reduced from 10.0 to 9.0 and 8.8 compared with the first pass, respectively. On route D, there is no difference in the average grain size. However, the fraction of the finer grains and serrated boundaries is increased at all three routes as compared to the first pass with Φ = 130°. It can be seen that the number of passes and different strain paths induce higher shear deformation, and hence enhance dynamic recrystallization. This promotes the formation of new grains. In other words, the evolution of new grains results from a series of strain-induced reactions [SAKA14]. The changes in the microstructure are associated with the continuous formation of high angle grain boundaries due to the accumulation of dislocations [SAKA14].

Figure 6.11 (b) displays that the average grain sizes on route A, C and D are slightly increased than that of the first pass with Φ = 110°. However, higher shear deformation of Φ = 110° might promote further the activation of dynamic recrystallization. It can be suggested that this mechanism consumes the serrated boundaries and small grains of the first pass, and hence builds new grains. As a result, more homogenous microstructure develops through all three routes compared to the first pass with Φ = 110°. Furthermore, even if the average grain sizes at the second pass with Φ = 110° are larger than those with Φ = 130°, the microstructures of Φ = 110° have relatively homogenous grain distribution in comparison of Φ = 130°.

More importantly, both channel angles have the smallest average grain size on route C. This can be explained by the fact that the shear directions are inverted and parallel

to each other on the identical shear plane between the successive passes on route C [TONG10]. The initial coarse grains are subjected to repetitive deformations during ECAP. This might result in a higher dislocation accumulation in the shear bands, and hence enhance dynamic recrystallization process [TONG10]. Therefore, the grain refinement on route C is more effective than other routes [SUH16-2].

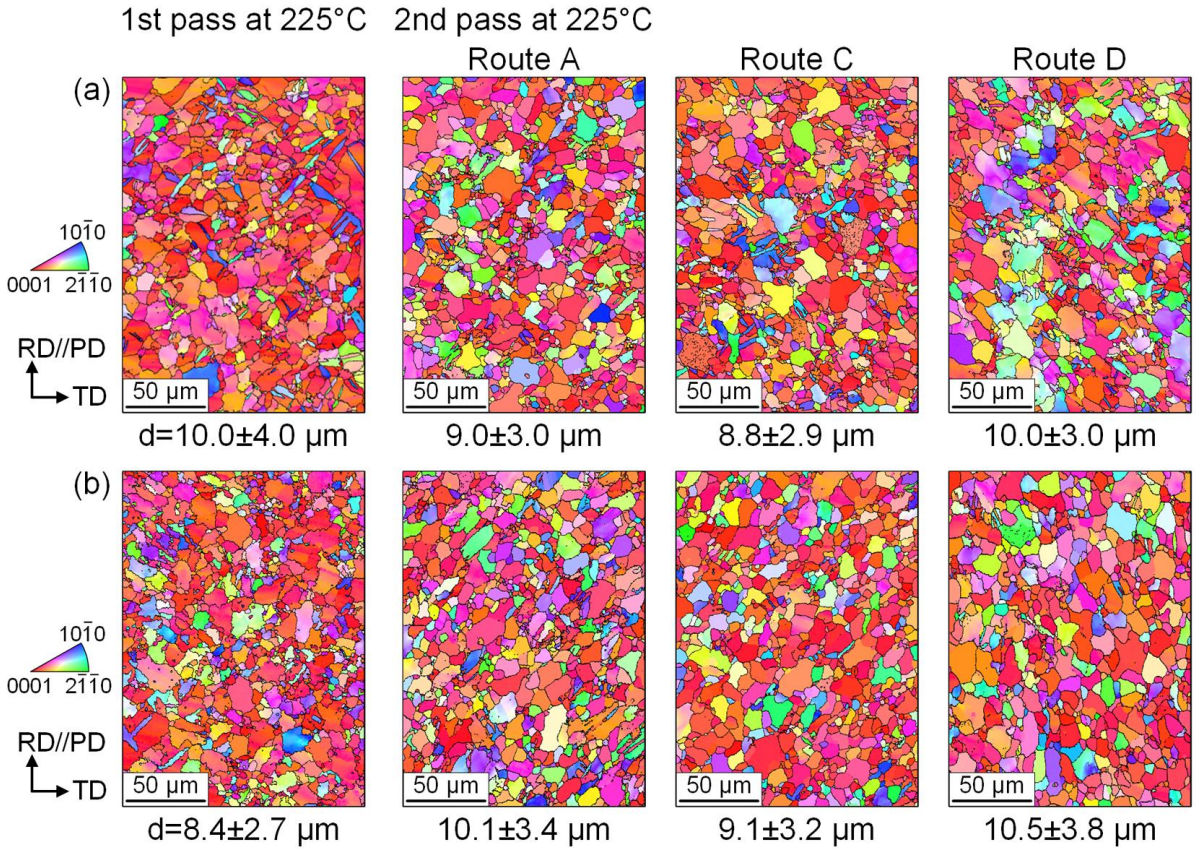

Figure 6.11: Influence of processing route on microstructure development of ECAPed AZ31 sheets at 225 °C with (a) Φ = 130° and (b) Φ = 110° [SUH16-2]

Figure 6.12 describes the global texture of ECAPed sheets at 225 °C with Φ = 110° and 130° on the routes A, C and D in terms of (0001) pole figure. Their corresponding density profiles are summarized in Figure 6.13. In the case of Φ = 130°, the texture exhibits a gradual waveform of the intensity distribution on route A and C, a symmetrical intensity spread on route D. On the other hand, in the case of Φ = 110°, parts of the texture generated in the first pass are split more dynamically on three routes. A distinct texture evolution is visibly evident in the intensity spread of the basal poles through different shearing patterns as follows [SUH16-2]:

Route A

Processing on route A leads to an increase in tendency for the (0001) poles to align from the ND to the RD. New texture component develops obviously, rotating by 70-80° to the RD. In the case of Φ = 130°, the tilt angle of the basal pole to the RD is 15° and a high valley is formed between the first and second peaks. On the other hand, the rotation of the basal poles by ~10° is observed at Φ = 110° and the intensity spread forms in a basin-like pattern.

Route C

As mentioned above, route C is characterized by shearing on the same plane but in an opposite sense in each pass [FURU01]. Hence, there may be a recovery of the initial texture after every even number of passes. However, this is not observed, but the texture intensity is weakened more markedly than the other routes with both channel angles. The splitting angle from the ND to the RD with Φ = 130° and 110° is about 25 and 15°, respectively. In both channel angles, the basal poles are distributed visibly broadly across the PD.

Route D

Processing on route D fundamentally makes a symmetrical texture formation in the RD and TD. The channel angle attributes to relatively different intensity distribution. In route D with Φ = 130°, the basal poles spread without rotation relatively homogenously in the RD and TD. In a similar manner to the first pass, a new texture component also develops along the TD by tensile twinning. By contrast, on route D with Φ = 110°, the texture component in the RD, which was generated in the first pass, weakens and the intensity is strengthened compared to Φ = 130°. Instead, a new component develops visibly along the TD. Moreover, there is a tilting of the basal poles by 5° in the RD and TD, respectively. Particularly, the basal poles are rotated by ~15° towards 45° from the RD. It suggests that this unique texture evolution also has a distinct effect on the mechanical anisotropy. In this regard, the mechanical and forming characteristics are described in sections 6.4.3 and 6.5.2 below in detail.

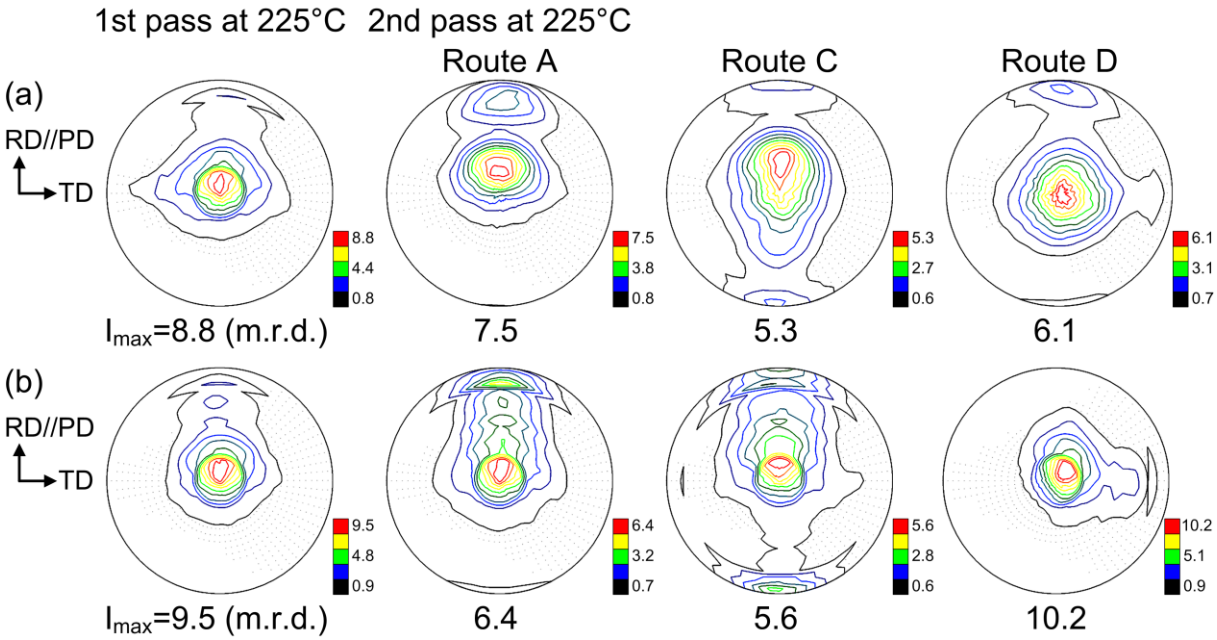

Figure 6.12: Influence of processing route on texture change of ECAPed AZ31 sheets at 225 °C with (a) Φ = 130°and (b) Φ = 110° in terms of (0001) pole figure [SUH16-2]

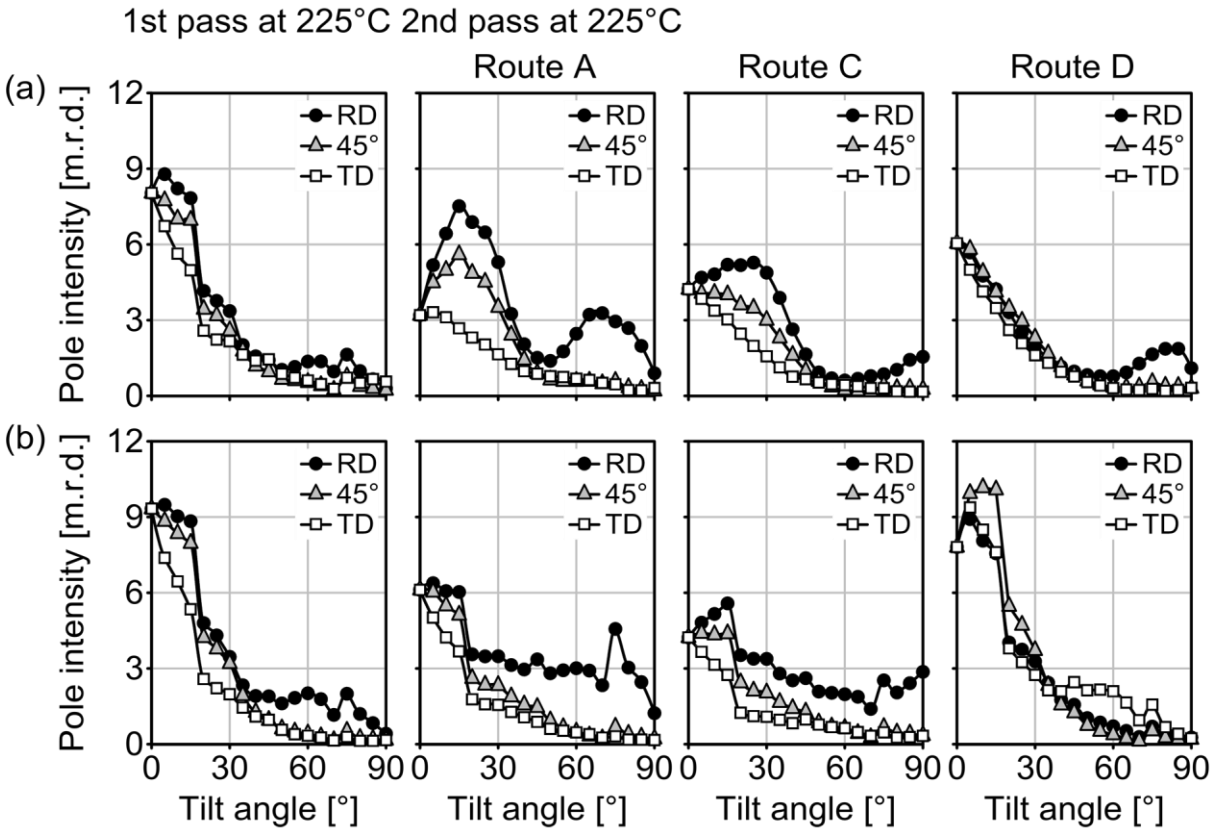

Figure 6.13: Density profiles of the basal pole along RD and TD depending on processing routes: (a) ECAPed AZ31 sheet at 225 °C with Φ = 130°, (b) ECAPed AZ31 sheet at 225 °C with Φ = 110° [SUH16-2]

6.4 Influence of process parameters on mechanical properties at room temperature

6.4.1 Processing temperature

For the evaluation of the effect of the processing temperature on the mechanical properties at room temperature, Figure 6.14 compares the stress-strain curves of the rolled and ECAPed sheets. The corresponding tensile properties at room temperature are listed in Table 6.1. The ECAP process enables the enhancement of the ductility at room temperature in comparison with the as-rolled condition. However, only the tensile properties in the direction, which is parallel to the PD, are developed in this regard. The ECAPed sheets have higher uniform strains and n-values in the RD than in the TD, while their yield strengths and r-values in the RD lower than in the TD. Besides, the specimen orientation has no significant influence on the ultimate tensile strengths as compared in Figure 6.15 [SUH15].

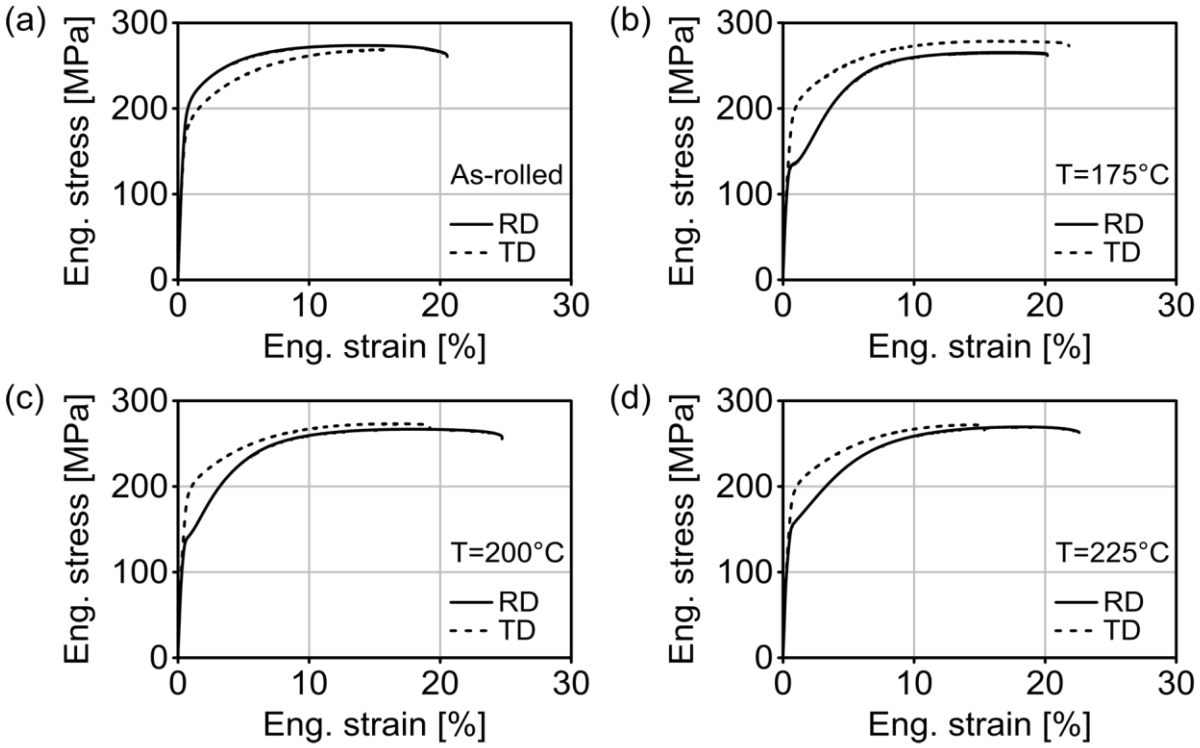

Figure 6.14: Strain-stress curves at room temperature of ECAPed AZ31 sheets with Φ = 130° in terms of processing temperature: (a) as-rolled condition, (b) 175 °C, (c) 200 °C, (d) 225 °C (RD: specimens parallel to PD, TD: specimens transverse to PD) [SUH15]

Processing temperature [°C]	*Tensile direction*	*YS [MPa]*	*UTS [MPa]*	*ε_u [%]*	*ε_f [%]*	*r_{10} [-]*	*n [-]*
As-rolled	*RD*	*190*	*275*	*13.4*	*19.4*	*1.59*	*0.13*
	TD	*171*	*269*	*14.8*	*15.7*	*1.73*	*0.17*
175	*RD*	*130*	*264*	*16.1*	*18.9*	*0.78*	*0.16*
	TD	*178*	*274*	*15.7*	*19.6*	*1.15*	*0.16*
200	*RD*	*137*	*266*	*17.2*	*23.2*	*0.82*	*0.17*
	TD	*180*	*275*	*15.3*	*19.1*	*1.08*	*0.16*
225	*RD*	*146*	*270*	*17.6*	*21.9*	*0.75*	*0.19*
	TD	*178*	*272*	*13.4*	*15.5*	*1.01*	*0.15*

Table 6.1: Influence of processing temperature on room temperature mechanical properties of ECAPed AZ31 sheets with Φ = 130° [SUH15]

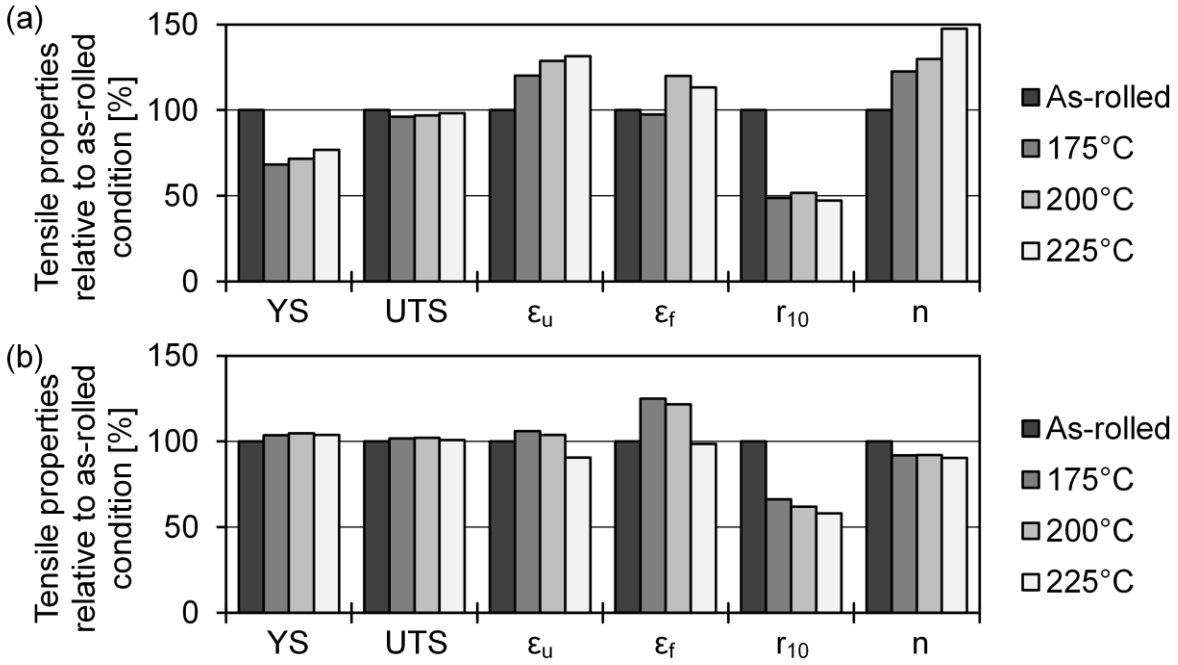

Figure 6.15: Relative tensile properties of ECAPed AZ31 sheets at Φ = 130° in terms of processing temperature compared with rolled sheet: (a) specimens parallel to PD (RD), (b) specimens transverse to PD (TD)

After a single ECAP process, the yield strengths in the RD are 30-50 MPa lower than in the TD. Especially, the yield strengths in the RD of the ECAPed sheets are decreased by 45-60 MPa as compared with the rolled sheet. It is observed that the ε_u in the RD increases with the processing temperature. The highest ε_u at room temperature is 17.6% in the RD of the ECAPed sheet at 225 °C. This is an improvement of 31% in

comparison to the rolled sheet (see Figure 6.15). On the other hand, there is no major improvement in the ε_u in the TD, but the ε_u decreases rather slightly with the temperature. This is directly related to the change in n-value. Compared to the rolled sheet, the n-value in the RD and TD of the ECAPed sheet at 225 °C increases from 0.13 to 0.19 and decreases from 0.17 to 0.15, respectively. In principle, high n-value indicates better ductility, particularly uniform elongation at room temperature [WU11]. Therefore, the ε_u in the RD is obviously enhanced, but the ε_u in the TD is slightly reduced.

The Lankford coefficients of the ECAPed sheets in both directions are reduced to 50-70% of the initial condition. The r_{10} is close to 0.8 in the RD and to 1.0 in the TD. That is, the thickness strain is accommodated more easily during the tension along the RD than along the TD. Even though these r-values indicate almost an isotropic deformation, an in-plane anisotropy appears actually after ECAP at three temperatures. Such a variation in the tensile properties at room temperature is associated with the grain refinement and texture weakening by ECAP [SUH15].

In the ECAPed samples, the increase in the ε_u and decrease in the YS along the RD have a direct correlation with the promoted activation of basal <a> slip. After a single ECAP pass, the basal poles are tilted towards the RD, which is parallel to the PD. This indicates that the c-axis of many grains is obliquely aligned to the tensile direction. This makes the resulting shear strain not zero, because the slip direction of the tilted c-axis is not parallel to the ND under in-plane extension at room temperature. That is, low activation energy for basal slip is necessary. Therefore, the ECAPed microstructure has high Schmid factor, where grains orient to facilitate the activation of basal <a> slip, as discussed in Figure 6.7. The rotation of grains and the low CRSS promote the activity of basal <a> slip during the tensile test. Consequently, higher ε_u and lower YS in the RD are observed than in the TD. With respect to the r_{10}, the larger tilt angle in the RD can also make easier the accommodation of the thickness strain. For this reason, the r_{10} in the RD is lower than in the TD at three processing temperatures.

In other aspects, the ductility of the ECAPed AZ31 sheets is improved by microstructure refinement due to dynamic recrystallization. Koike et al. [KOIK03] attributed the enhancement of ductility at room temperature after grain refinement through ECAP to

the activation of non-basal slips. With the aid of texture simulations, the activity of basal <a> slip decreases, but the activity of prismatic and pyramidal <a> slips increases after the plastic yielding [AGNE05-2]. The easiness of non-basal slip systems indicates the higher possibility for the occurrence of dynamic recrystallization, because these deformation modes lead to a large degree of grain distortion with high elastic stored energy [YI05]. Moreover, dynamic recrystallization removes dislocations and induces the strain-free grains [SAKA14]. For this reason, the yield strengths of the ECAPed sheets are lower than the rolled sheet.

6.4.2 Channel angle

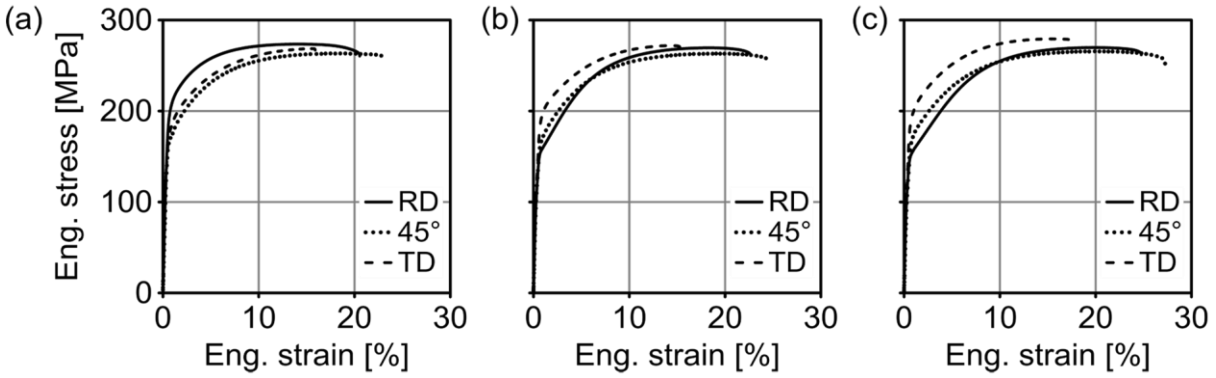

Figure 6.16: Stress-strain curves at room temperature of ECAPed AZ31 sheets with respect to channel angle: (a) as-rolled condition, (b) ECAPed sheet at 225 °C with Φ = 130°, (c) ECAPed sheet at 225 °C with Φ = 110°

Channel Angle [°]	***Tensile direction***	***YS [MPa]***	***UTS [MPa]***	***ε_u [%]***	***ε_f [%]***	***r_{10} [-]***	***n [-]***
As-rolled	*RD*	*190*	*275*	*13.4*	*19.4*	*1.59*	*0.129*
	45°	*167*	*264*	*17.4*	*22.0*	*1.87*	*0.173*
	TD	*171*	*269*	*14.8*	*15.7*	*1.73*	*0.172*
130	*RD*	*146*	*270*	*17.6*	*21.9*	*0.75*	*0.190*
	45°	*151*	*264*	*18.2*	*21.6*	*1.34*	*0.186*
	TD	*178*	*272*	*13.4*	*15.5*	*1.01*	*0.155*
110	*RD*	*142*	*268*	*19.3*	*24.4*	*0.74*	*0.217*
	45°	*154*	*265*	*19.3*	*26.9*	*1.28*	*0.193*
	TD	*183*	*280*	*15.0*	*16.6*	*1.45*	*0.154*

Table 6.2: Influence of channel angle on room temperature mechanical properties of ECAPed AZ31 sheets at 225 °C with Φ = 110° and 130°

Figure 6.16 presents the influence of the channel angle on the tensile properties at room temperature of AZ31 sheets, which are processed by ECAP at 225 °C with Φ = 110° and 130°. Their corresponding properties are given in Table 6.2. The stress-strain curves of the ECAPed sheets, which are deformed with Φ = 110° at other processing temperatures, are referred to Table 9.3.

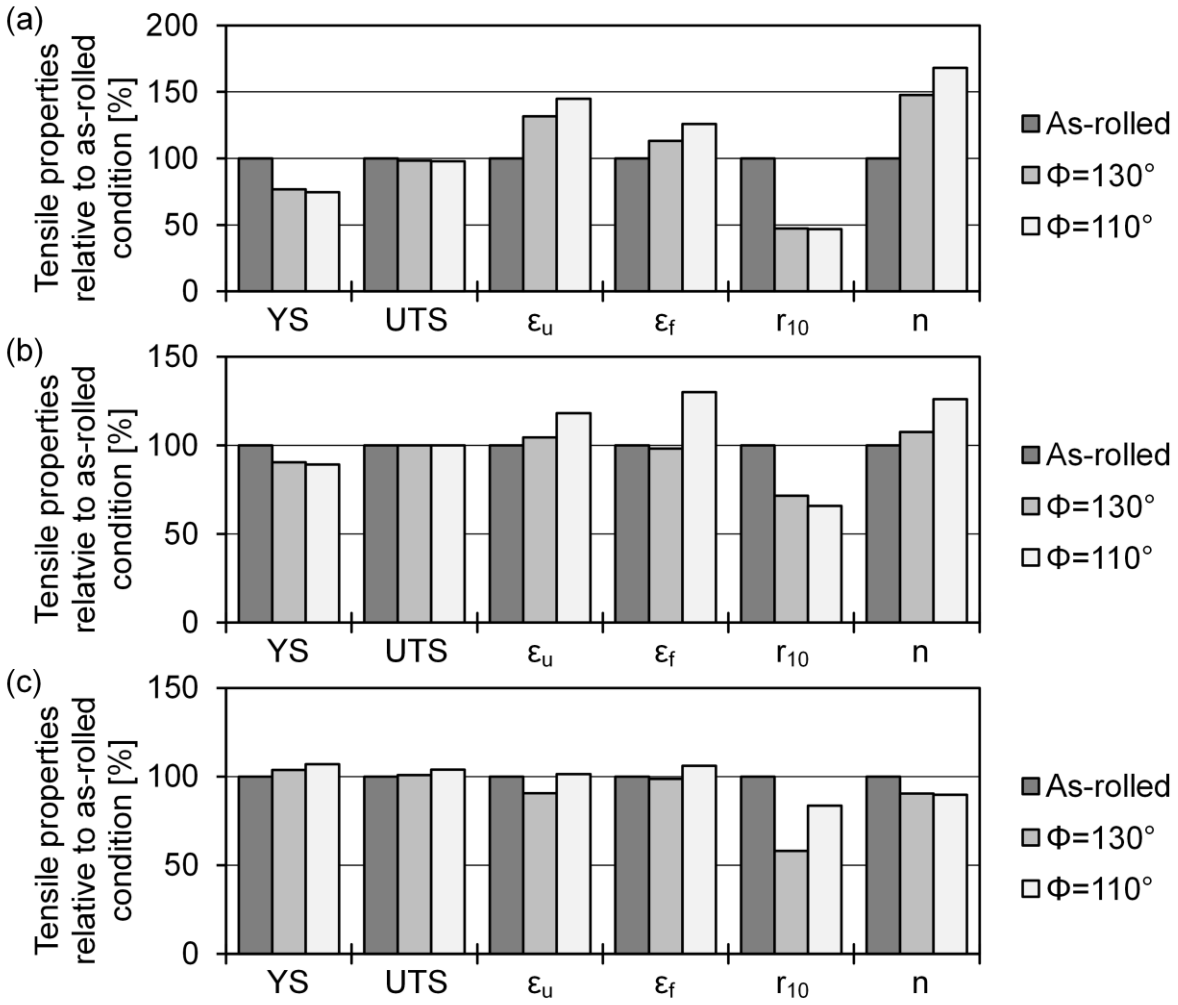

Figure 6.17: Relative tensile properties of ECAPed AZ31 sheets at 225 °C with respect to channel angle in comparison to rolled sheet: (a) specimens parallel to PD (RD), (b) specimens at 45° to PD (45°), (c) specimens transverse to PD (TD)

The analytically effective strain per pass with Φ = 110° and 130° amounts to about 0.8 and 0.5, respectively. In this context, the effect of higher shear deformation is evident from the increase in the ε_u in the RD with Φ = 110° (19.3%). The uniform elongation is improved by 45 and 10% compared to the rolled sheet (13.4%) and Φ = 130° (17.6%), respectively (refer to Figure 6.17). In a related development, the n-value of 0.22 at

Φ = 110° is increased by 68 and 14% compared to the rolled sheet (0.13) and Φ = 130° (0.19). Based on this, it is confirmed that high n-value leads to high ductility. It is noticeable that the ε_u and n-value are developed considerably at 45° with Φ = 110°. However, there is still no enhancement of the ε_u in the TD at Φ = 110° (15%).

The YS at Φ = 110° is more decreased along the RD, but slightly increased in the 45° and TD than that at Φ = 130°. Particularly, there is no difference of the r_{10} of 0.75 in the RD between two channel angles. In the case of Φ = 110°, the r_{10} increases from the RD to the TD (0.75 to 1.45). However, the r_{10} is highest at 45° with Φ = 130° (1.34). In comparison to the rolled sheet, it is a notable feature that the difference in mechanical behavior between the RD and 45° is reduced in both channel angles, whereas the differences between the 45° and TD are larger. This variation in the tensile properties is associated with the microstructure and texture evolution as described above.

After the single ECAP pass with Φ = 110°, the microstructure exhibits a higher fraction of serrated grain boundaries and fine grains. This microstructural evolution can promote the mobility of the grains due to a progressive transformation to high angle grain boundaries. This is also correlated with a broader angular distribution of the basal poles as well as the occurrence of tension twins along the RD. Such a change in the microstructure and texture at Φ = 110° enables further activation of basal <a> slip compared to Φ = 130°, with respect to the fact that ECAP with Φ = 130° already showed a higher feasibility to activate basal slip than the rolled sheet. Consequently, the higher shear formation by Φ = 110° reduces the YS in the RD and 45° and induces the larger ε_u in the RD and 45° than those of Φ = 130° and the rolled sheet. Regarding the r_{10} in the TD, the intensity spread with Φ = 130° is broader than with Φ = 110° as displayed in Figure 6.9. When the basal poles are distributed more broadly and split or inclined more along one direction than others, the r-value increases as the angle between the texture-broadened direction and tensile direction increases [SUH14]. The reason is that basal slip is favorable during tensile deformation along the texture-broadened direction [SUH14]. In this manner, this intensity distribution at Φ = 110° can be relatively unfavorable for the accommodation of the thickness strain compared to Φ = 130°. Consequently, the r_{10} in the TD of Φ = 110° is higher than that of Φ = 130°.

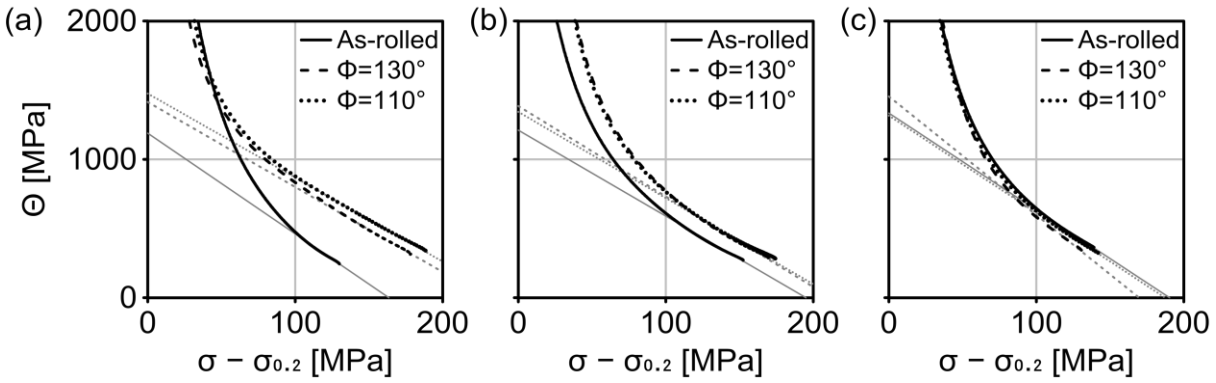

Figure 6.18: Influence of channel angle on work hardening behavior of ECAPed AZ31 sheets at 225 °C in form of Θ vs. (σ - $\sigma_{0.2}$) plot: (a) specimens parallel to PD (RD), (b) specimens at 45° to PD (45°), (c) specimens transverse to PD (TD)

Figure 6.18 compares the work hardening behavior of the ECAPed AZ31 sheets. The work hardening behavior in different tensile directions is remarkably distinct. In the RD, the ECAPed sheets have higher hardening rate and slower drop of the Θ, whereas the rolled sheet shows a steep decrease in the Θ and much lower hardening rate. The higher shear deformation at Φ = 110° leads to a relative high Θ and restrained dynamic recovery (related to the slope of the curves in stage III) as compared to Φ = 130°. Both channel angles exhibit a comparable hardening behavior at 45° and the Θ is higher than the rolled sheet. On the contrary, there is no difference of the hardening behavior in the TD between the rolled and ECAPed sheets.

Agnew et al. [AGNE03] analyzed the operation of non-basal slips in the basal-textured AZ31B plate using an elasto-plastic self-consistent simulation. They reported that prismatic <a> slip exhibits a relative large activity compared with pyramidal <c+a> slip during in-plane extension at room temperature. In this regard, the cross-slip of <a> dislocations from basal to prismatic planes leads to a decrease in the hardening rate of the basal planes [VALL06]. Consequently, dynamic recovery originates from this cross-slip of <a> dislocations, and it can contribute to this softening behavior [VALL06]. The slower drop in the Θ indicates that the tilted c-axis of the ECAPed AZ31 sheets, which is favorable for basal <a> slip, reduces the activation of prismatic <a> slip [SUH16-1]. This is in agreement with the work hardening behavior of AM60 alloys processed by hot rolling and ECAP [VALL06] and DSR processed AZ31 sheets [HUAN08].

The activated {10$\bar{1}$2} <10$\bar{1}$1> tension twins are observed in the ECAPed AZ31 sheets. In general, twinning occurs at the grain boundaries and then grows into the parent grain. {10$\bar{1}$2} tension twin boundaries with the reorientation of the basal planes by ~86° can act as barriers to dislocation motion and become a source of work hardening [HUAN08]. A similar observation on twin-induced work hardening is also reported in the existing studies. {10$\bar{1}$2} tension twinning induces strongly an increase in the work hardening during deformation and leads to a larger uniform elongation [BOHL07]. Therefore, the higher improved ε_u in the RD with Φ = 110° can be attributed to higher work hardening, which is resulted from the suppressed dynamic recovery and twin-induced work hardening [SUH16-1].

6.4.3 Processing route

ECAP process enables a multiple repetition so that higher shear strain leads to further development of the microstructure. Hereby, this technique provides variations by a change of the sample orientation regarding the shear direction. Figure 6.19 presents the influence of three processing routes on room temperature mechanical properties of the ECAPed AZ31 sheets [SUH16-2]. The samples are processed at 225 °C with Φ = 110°. Table 6.3 lists their corresponding tensile properties.

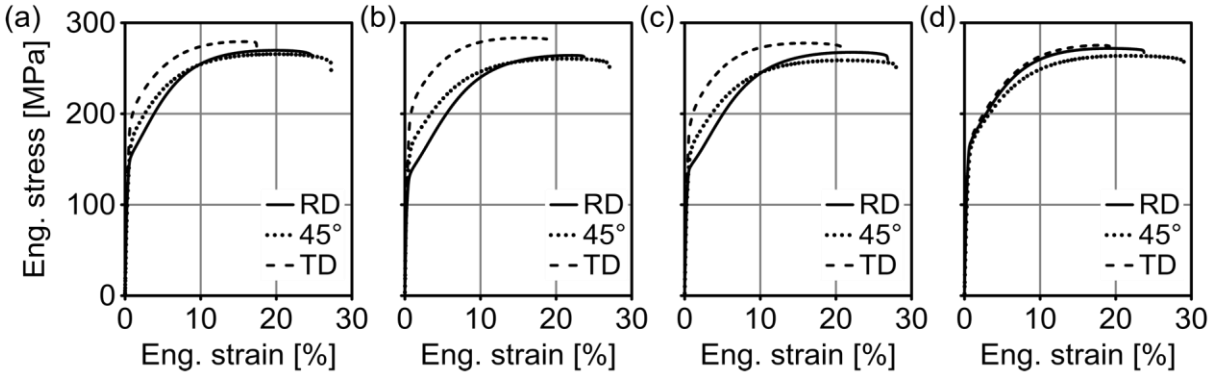

Figure 6.19: Stress-strain curves at room temperature of ECAPed AZ31 sheets with Φ = 110° in terms of processing route: (a) 1st pass at 225 °C, (b) 2nd pass on route A, (c) route C, (d) route D [SUH16-2]

Processing route	*Tensile direction*	*YS [MPa]*	*UTS [MPa]*	*ε_u [%]*	*ε_f [%]*	*r_{10} [-]*	*n [-]*
A	*RD*	*127*	*264*	*21.1*	*23.7*	*0.53*	*0.27*
	45°	*142*	*261*	*20.7*	*26.6*	*1.14*	*0.22*
	TD	*189*	*283*	*14.9*	*19.4*	*1.33*	*0.15*
C	*RD*	*136*	*268*	*21.5*	*26.1*	*0.71*	*0.27*
	45°	*146*	*260*	*20.4*	*26.7*	*1.17*	*0.21*
	TD	*183*	*279*	*15.3*	*20.5*	*1.13*	*0.15*
D	*RD*	*158*	*271*	*18.4*	*24.2*	*1.04*	*0.20*
	45°	*149*	*264*	*20.6*	*28.6*	*1.23*	*0.22*
	TD	*158*	*276*	*17.2*	*18.5*	*0.86*	*0.21*

Table 6.3: Influence of processing route on room temperature mechanical properties of ECAPed AZ31 sheets at 225 °C with Φ = 110° [SUH16-2]

Figure 6.20 compares the tensile properties of three routes with those of the rolled sheet. The YS on route A and C increases from the RD to the TD. Route A has the lowest YS of 127 MPa in the RD and the highest YS of 189 MPa in the TD among all cases. On route A, the YS is reduced by 33% in the RD and increased by ~10% in the TD and 45°, respectively. On route C, the YS is almost identical with the first pass. Route D has the YS in the RD and 45° comparable with the first pass, but the YS in the TD is lowest among all cases. Consequently, route D has comparable YS in three tensile directions. The variation in the UTS on three routes is negligible [SUH16-2].

There is much attention paid to the development of the ε_u. After the two ECAP passes, the ε_u in the RD is improved by above 40% compared to the as-rolled condition. Route C provides the highest ε_u in the RD among all samples, which is 21.5% and corresponds to above 160% of the rolled sheet. The texture processed by route C shows the lowest pole density and the broadest angular distribution of the basal poles across the sheet plane (refer to section 6.3.3). This texture weakening and misorientation facilitates to accommodate the plastic deformation more easily along the RD. This is also favorable for the deformation at 45°. That is, the more activated basal slip reduces the YS and increases the ε_u in the RD and 45°. However, there is no difference of the ε_u in the TD, because the considerable texture change occurs only in the RD. In a similar manner, on route A, the ε_u in the RD is increased by 58% compared to the rolled sheet,

but there is no development of the ε_u in the TD. In this regard, the n-values in the RD on route A and C are increased by 210% compared to the as-rolled sample, while the n-values in the TD rather decrease to 87% of the rolled sheet. Furthermore, the r_{10} in the RD is smaller than in the TD on route A and C. The reason is that the thickness strain can be accommodated more easily by the higher activation of basal <a> slip during in-plane extension in the RD than in the TD [SUH16-2].

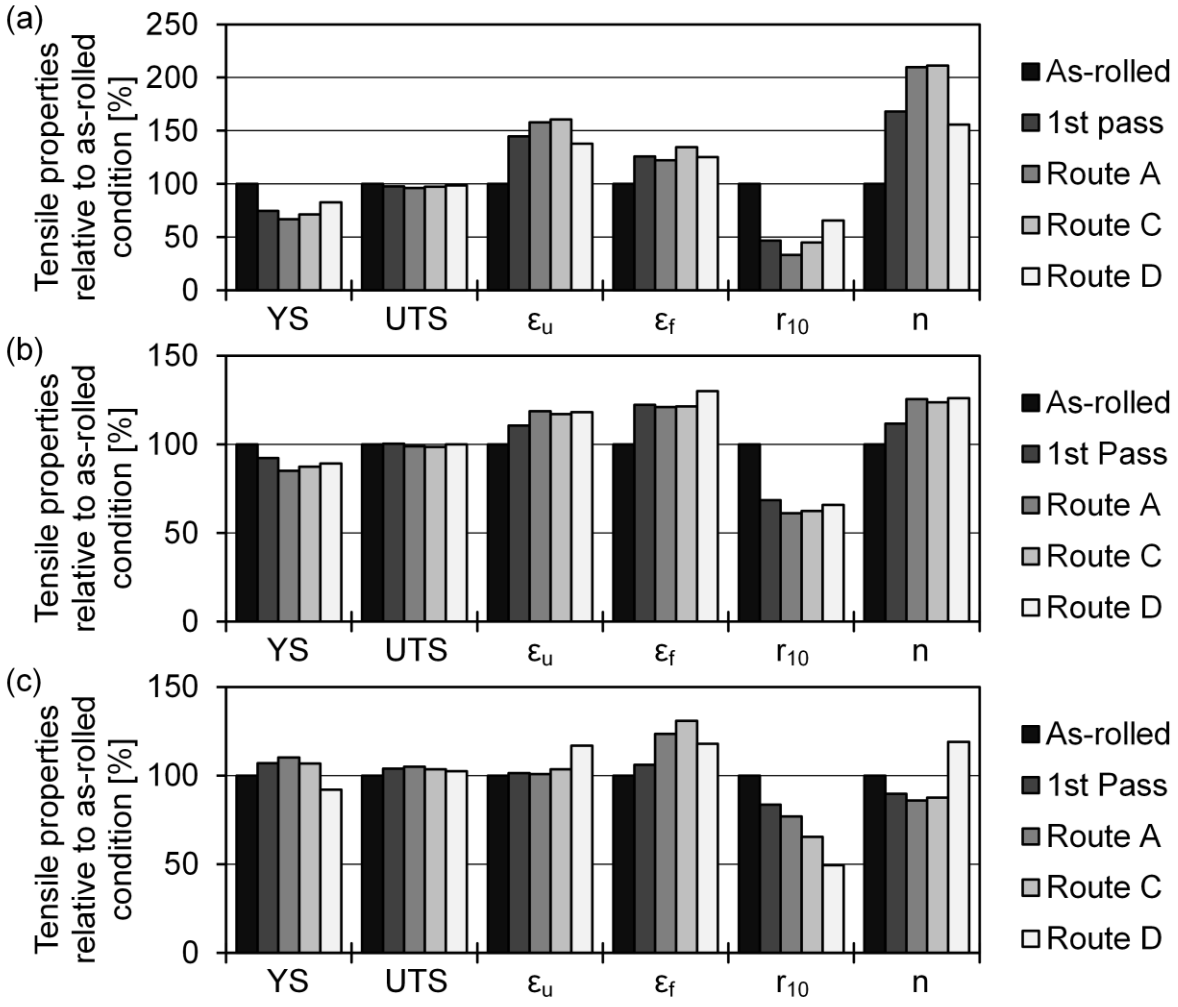

Figure 6.20: Relative tensile properties of ECAPed AZ31 sheets at 225 °C with Φ = 110° in terms of processing route: (a) specimens parallel to PD (RD), (b) specimens at 45° to PD (45°), (c) specimens transverse to PD (TD)

On the other hand, on route D, the ε_u in the RD, 45° and TD is 18.4, 20.6 and 17.2%, respectively. Compared to the first pass, the ε_u in the RD is reduced slightly, but the ε_u in the 45° and TD is enhanced by 6.7% and 17%, respectively. In a related development, it is noticeable that the n-value in the TD is improved significantly only on route D,

and hence the ε_u in the TD can be increased to a similar extent of the RD. Consequently, the r_{10} in three directions amounts to 1.04, 1.23 and 0.82, respectively. The r_{10} close to 1 indicates a quasi-isotropic cross-sectional contraction. On route D, the basal poles are tilted and spread along the RD, TD and 45°. This facilitates the accommodation of the thickness strain. For the above reasons, route D enables reducing the mechanical anisotropy in the tensile directions, and thus allows a comparable hardening behavior of the ECAPed sheet [SUH16-2].

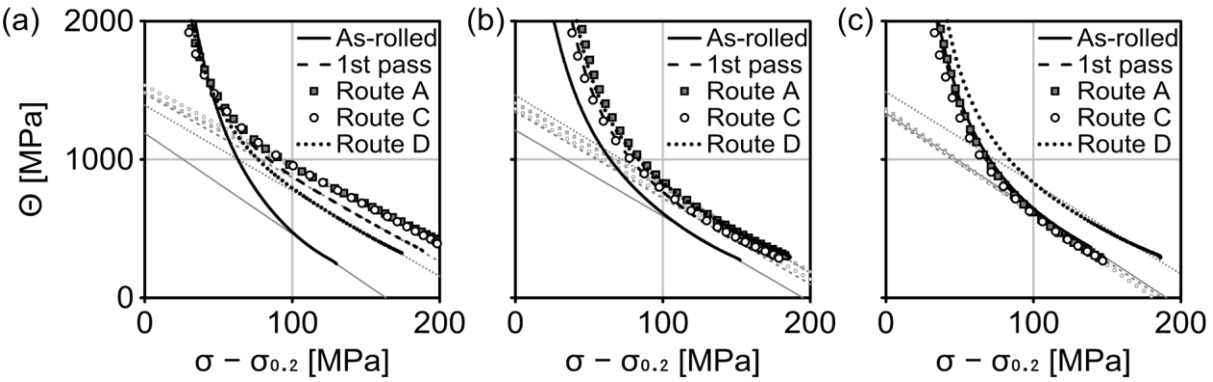

Figure 6.21: Influence of processing route on work hardening behavior of ECAPed AZ31 sheets at 225 °C with Φ = 110° in form of Θ vs. (σ - $\sigma_{0.2}$) plot: (a) specimens parallel to PD (RD), (b) specimens at 45° to PD (45°), (c) specimens transverse to PD (TD) [SUH16-1]

Figure 6.21 shows the effect of the processing route on the work hardening behavior of the ECAPed AZ31 sheets. In the RD, route A and C have a comparable hardening behavior with the highest Θ and the lowest slope in stage III as presented in Figure 6.21 (a). Route D has rather lower values and faster drop in the Θ than that of the single pass. This hardening behavior on route D results in the lower elongation in the RD than route A and C. Regarding the slope of the curves, the suppressed dynamic recovery on route A and C helps maintain a high hardening rate. This leads to low sensitivity to the strain localization, and hence improves the ε_u [SUH16-1].

As described above, the texture altering and misorientation provide a more favorable orientation for basal slip and tension twinning. Therefore, high work hardening capacity and weakened texture enhance the ductility on route A and C. Figure 6.21 (b) depicts that three routes and the first pass exhibit a comparable hardening behavior at 45° and the Θ is higher than the rolled sheet. In the TD, the hardening rate on route D is much

higher than other process conditions, while the hardening behavior of other conditions is almost similar as presented in Figure 6.21 (c). Therefore, route D provides the highest ε_u in the TD. This can be explained by the fact that the shear deformation along the TD by ECAP induces the inclination of the basal poles as well as the activation of $\{10\bar{1}2\}$ tension twins in the TD. The restrained dynamic recovery and the twin-induced work hardening result in the larger ε_u in the TD on route D. Consequently, route D provides a comparable hardening behavior in three tensile directions, and hence allows a quasi-isotropic hardening of the ECAPed AZ31 sheet at room temperature [SUH16-1].

6.5 Influence of process parameters on cold formability

The channel angle and processing route make a significant contribution to developing the microstructure and correlated mechanical behavior of the ECAPed AZ31 sheets. Based on this, forming tests of a U-shaped channel and Nakajima tests are carried out at room temperature with the AZ31 sheets, which are processed by ECAP at 225 °C with the channel angles of 110° and 130° as well as on the processing routes A, C, and D. The forming depths and forming limits are characterized and compared with the emphasis on the effect of the channel angle and processing route on cold formability of the ECAPed AZ31 sheets.

6.5.1 Channel angle

Figure 6.22 shows the effect of the channel angle on the U-channel forming at room temperature of the AZ31 sheets, which are processed by ECAP at 225 °C with Φ = 110° and 130°. In the case of the rolled sheets, the strips cut parallel to the RD and TD reach the forming depth of maximal 6 mm without cracking, because there is no large difference of the ε_u in the RD and TD as listed in Table 6.1. On the contrary, the forming depth at 45° is 7 mm without mechanical failure due to the higher ε_u than in the RD and TD. When applying further higher forming depths, the U-shaped strips show crack at the curvature, where a high degree of plastic deformation and thickness reduction is required.

Figure 6.22: Influence of channel angle on cold forming of U-shaped channel of rolled and ECAPed AZ31 sheets at 225 °C with Φ = 110° and 130°: (a) strips parallel to PD, (b) strips at 45° to PD, (c) strips transverse to PD

In the case of the ECAPed sheets, there is a quantitative improvement of the forming depth in the RD and 45° with Φ = 110°, but no distinct development with Φ = 130°. Besides, both channel angles provides no noticeable enhancement in the TD. At Φ = 110°, both forming depths in the RD and 45° are 10 mm. This corresponds to an improvement of 67 and 43% compared to the as-rolled condition, respectively. On the other hand, the forming depth in both direction is just 7 mm with Φ = 130°. In the strips cut transverse to the PD (equal to the TD), the samples are deformed with the forming depths of 7 and 6 mm at Φ = 110° and 130°, respectively.

As predicted, this directional forming behavior at the U-shaped channel is in good agreement with the results of the uniaxial tensile test at room temperature. Compared to the rolled sheet, the higher forming depths of the ECAPed sheets can be attributed to lower r_{10} and higher n-value as described in Figure 6.23. As mentioned above, low r-value and high n-value lead to the increase of sheet formability in Mg alloys [YI10]. Such an improvement in the formability can be expected for the ECAPed sheets due to the inclination of the basal poles and weakened basal texture. This is in good agreement with the results of Yukutake et al. [YUKU03]. They reported that a hot-rolled AZ31

thick plate with a favored texture for basal <a> slip exhibited a superior formability in both deep drawing and stretch forming [YUKU03].

Regarding the work hardening behavior, Figure 6.23 (a) presents that there is a distinct increase in the n_{RD} and $n_{45°}$ with $\Phi = 110°$ compared with the rolled sheet and $\Phi = 130°$. Therefore, the $\bar{n}$ also increases with decreasing the channel angle. In this context, it is confirmed that lower channel angle is considerably effective for increasing the activity of basal <a> slip, and hence it enables the enhancement of the forming properties of Mg sheets at room temperature.

In terms of the r-value, there is no difference of the r_{RD} and $r_{45°}$ between $\Phi = 110°$ and 130° as depicted in Figure 6.23 (b). Compared to the $r_{45°}$, the r_{TD} of $\Phi = 110°$ is rather increased, while the r_{TD} of $\Phi = 130°$ is reduced. Hence, the r_{TD} of $\Phi = 110°$ is around 50% higher than that of $\Phi = 130°$. Consequently, the $\bar{r}$ of $\Phi = 110°$ and 130° is comparably close to 1, but the absolute Δr of $\Phi = 130°$ is almost three times higher than that of $\Phi = 110°$ (0.46 vs. 0.18). However, the difference between the maximal and minimal r-value at $\Phi = 110°$ is rather higher than $\Phi = 130°$ (0.71 vs. 0.59). Because the Δr is conventionally devised with respect to earing behavior during deep drawing of cubic metal sheets [BOHL07], it is necessary to interpret the in-plane anisotropy in hexagonal materials differently.

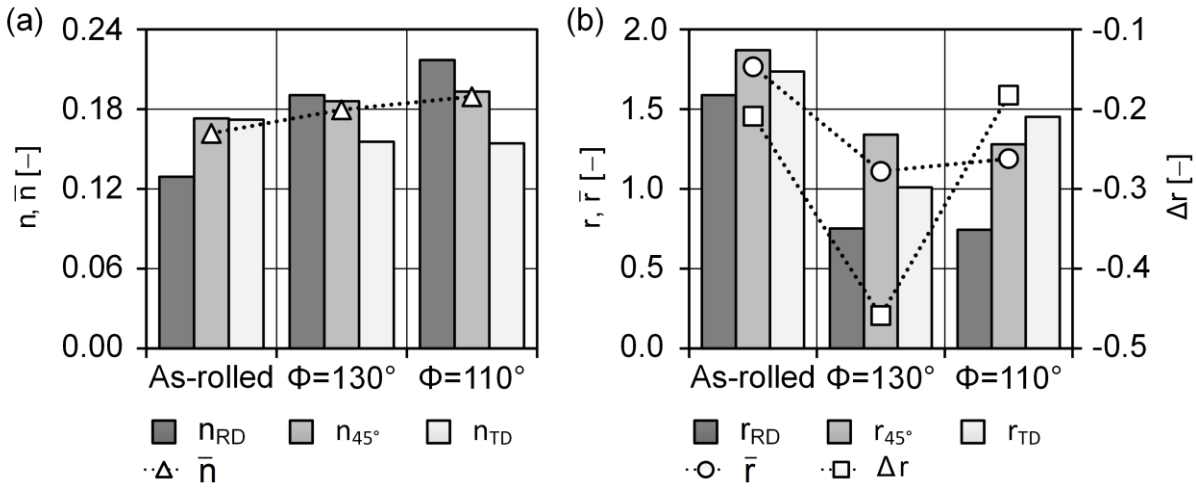

Figure 6.23: Comparison of n-value (a) and r-value (b) of rolled sheet and ECAPed AZ31 sheets at 225 °C with Φ = 110° and 130°

6.5.2 Processing route

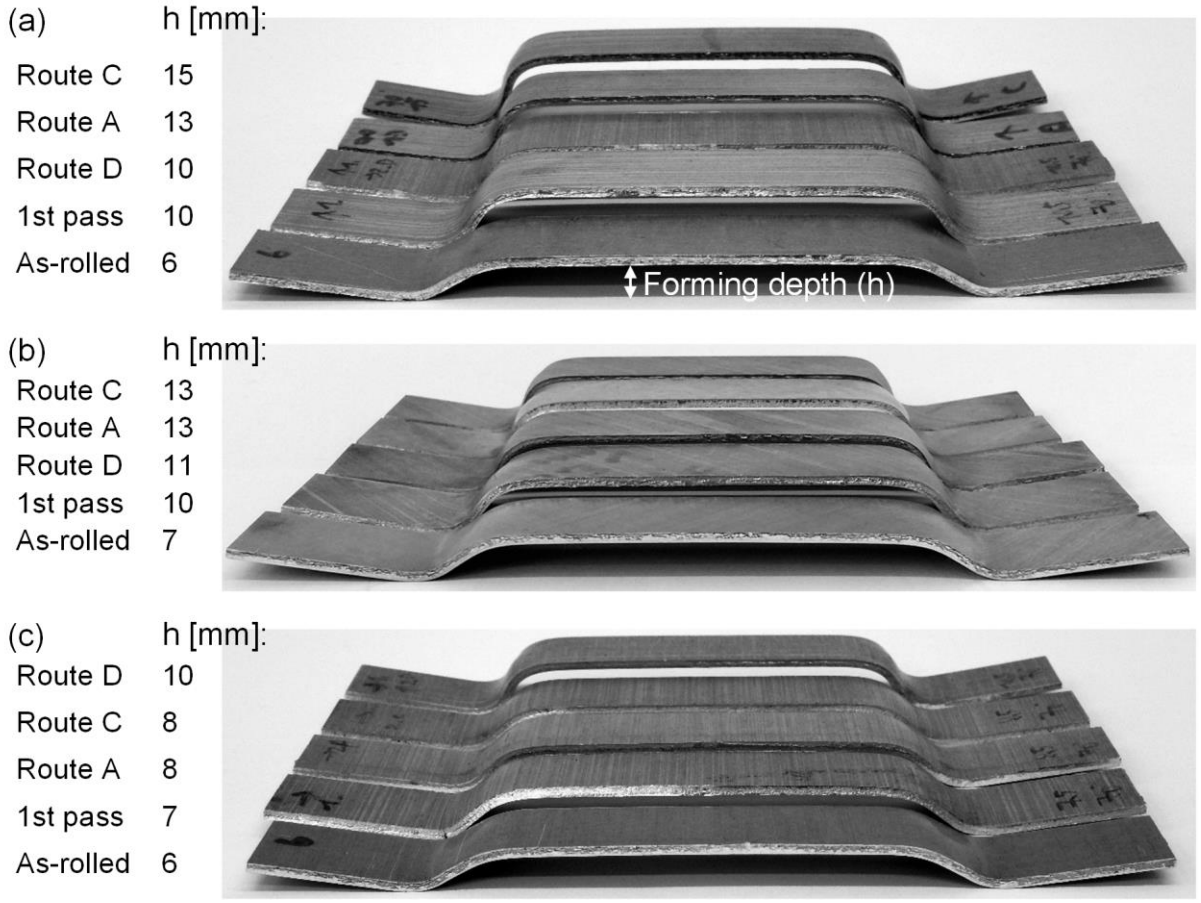

Figure 6.24: Influence of processing route on cold forming of U-shaped channel of rolled and ECAPed AZ31 sheets at 225 °C with Φ = 110°: (a) strips parallel to PD (RD), (b) strips at 45° to PD (45°), (c) strips transverse to PD (TD) [SUH16-2]

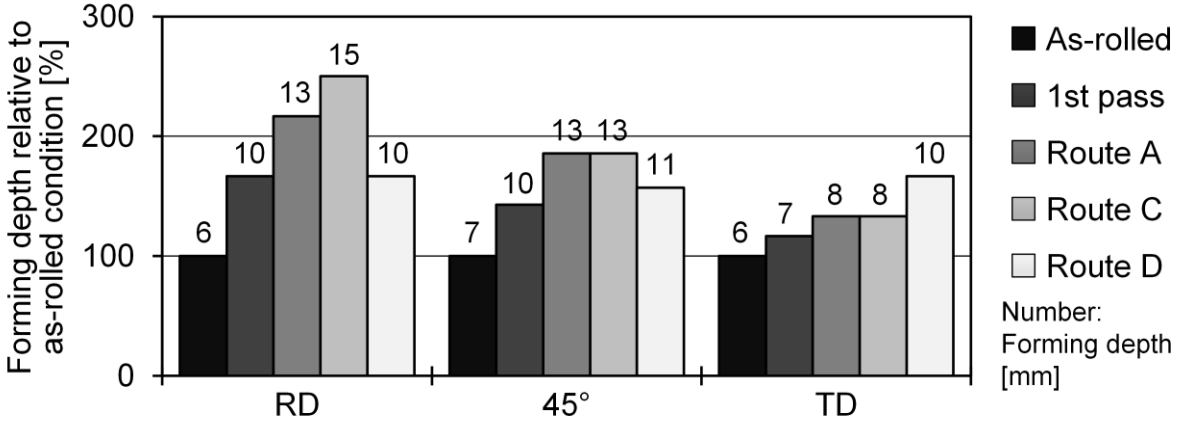

Figure 6.25: Relative forming depth of ECAPed AZ31 sheets at 225 °C with Φ = 110° regarding processing route in comparison of as-rolled condition (RD: strips parallel to PD, 45°: strips at 45 to PD, TD: strips transverse to PD) [SUH16-2]

From the results of the tensile tests, it is predicted that route C provides the highest forming depth in the RD and route D results in a comparable forming depth in three directions at the U-shaped strips [SUH16-2]. These predicted results actually occur as displayed in Figure 6.24. Since the cold formability at Φ = 110° is better than Φ = 130°, the comparison of the forming depths focuses on the effect of the processing routes on the ECAPed sheets with Φ = 110°.

In the RD, route C deforms the strip with the highest forming depth of 15 mm, which is 150% higher than that of the rolled sheet (refer to Figure 6.25). On route A and D, it corresponds to 13 and 10 mm, respectively. The forming depth of route D is equal to that of the first pass. At 45°, the forming depth reaches 13 mm on route A and C. Route D forms the strip with the forming depth of 11 mm. In the TD, route D makes the maximal forming depth of 10 mm, while the strip reaches up to 8 mm on route A and C. In the RD and 45°, route A and C have the highest forming depth. On the contrary, route D exhibits the maximum value in the TD among all cases. Consequently, route D provides a comparable formability with the forming depth of 10, 11 and 10 mm in three directions. These results are in good agreement with the development of the ε_u and n-value depending on different shear orientation as discussed above [SUH16-2].

It is generally expected that high r-values tend to reduce the fracture around cup corner and hence lead to higher limiting drawing ratios [LEE84]. Based on this, the rolled sheet should have superior sheet formability. In Figure 6.26 (a), the r-values of the rolled sheet are twice larger than those of route C in the RD. However, route C shows more enhanced formability than the as-rolled sample. This indicates that high r-values restrict the deformability in the thickness direction, which is the main limit of Mg alloy sheets with a strong basal texture [SUH14]. Several studies show that Mg alloys with random texture accompanying low plastic anisotropy are suitable for deep drawability [CHEN07, YI10] and stretch formability [HUAN11, WU11]. Regarding $\bar{r}$ and Δr, the $\bar{r}$ on three routes is comparably close to 1. On the contrary, route D has the absolute Δr, even though route D exhibits a comparable forming behavior at room temperature. However, the difference between the maximal and minimal r-value is lowest on route D among all conditions [SUH16-2]. The results represent that the correlation of sheet formability with r-value in Mg alloys should be interpreted in a different way [YI10].

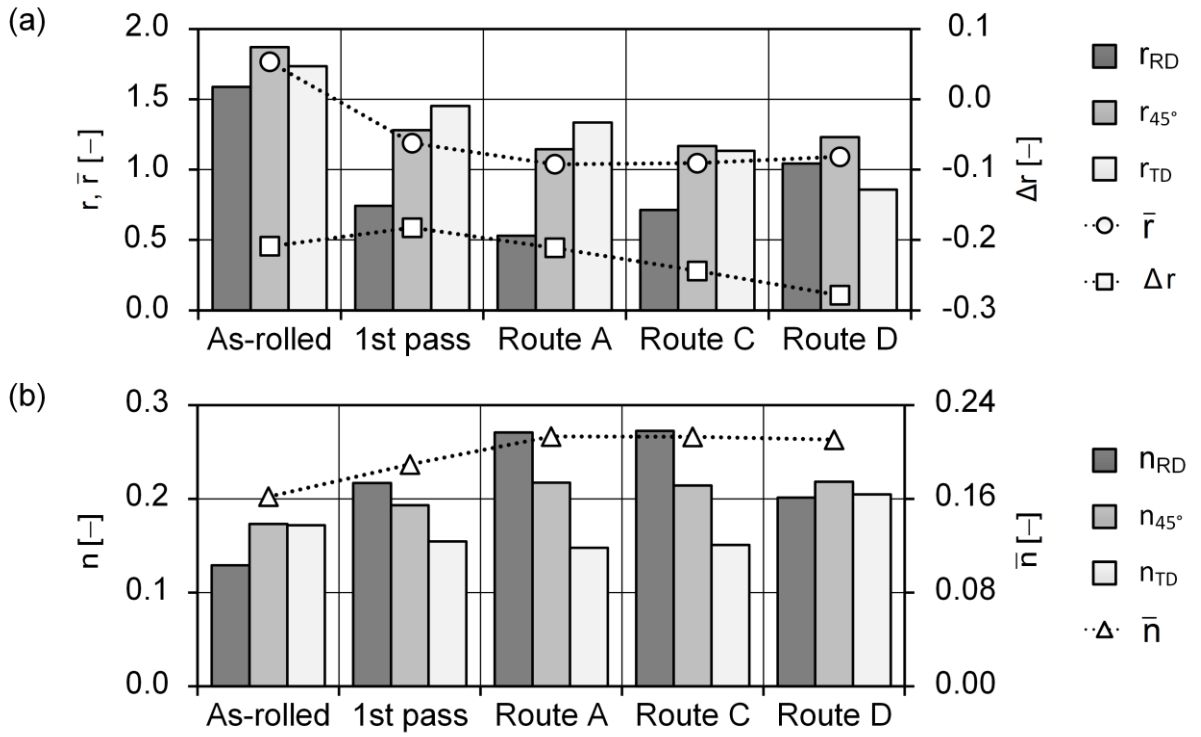

Figure 6.26: Influence of processing route on r-value (a) and n-value (b) of ECAPed AZ31 sheets at 225 °C with Φ = 110° [SUH16-2]

Such a development of cold formability has been attributed mainly to low r-value and high n-value induced by weakened texture [SUH14]. In this regard, the rolled AZ31 sheet has high r-value and low n-value. Therefore, the forming depths in three directions are lowest. In the case of ECAPed sheets, Figure 6.26 (b) shows that the n_{RD} is highest on route A and C. The $n_{45°}$ is comparable on three routes. The n_{TD} is highest on route D, which is almost identical to n_{RD} and $n_{45°}$. This is related with the comparable work hardening behavior on route D as presented in Figure 6.21. Compared to the rolled sheet, the $\bar{n}$ on route D is increased by 30% from 0.16 to 0.21. Although the $\bar{n}$ on route A and C is 0.21, there is a large difference between the n_{RD} and n_{TD} on both routes. The development of the forming depths shows a deep correlation with the n-value. Particularly, it is confirmed that almost identical n-value and r-value in three directions contribute to a comparable forming behavior on route D. Moreover, there is an interrelationship between r-value and n-value in the ECAPed sheets. Low r-value leads to high n-value, or inversely high n-value results in low r-value. In the RD, such a relationship is observed obviously. This is correlated directly with the microstructure development during ECAP [SUH16-2].

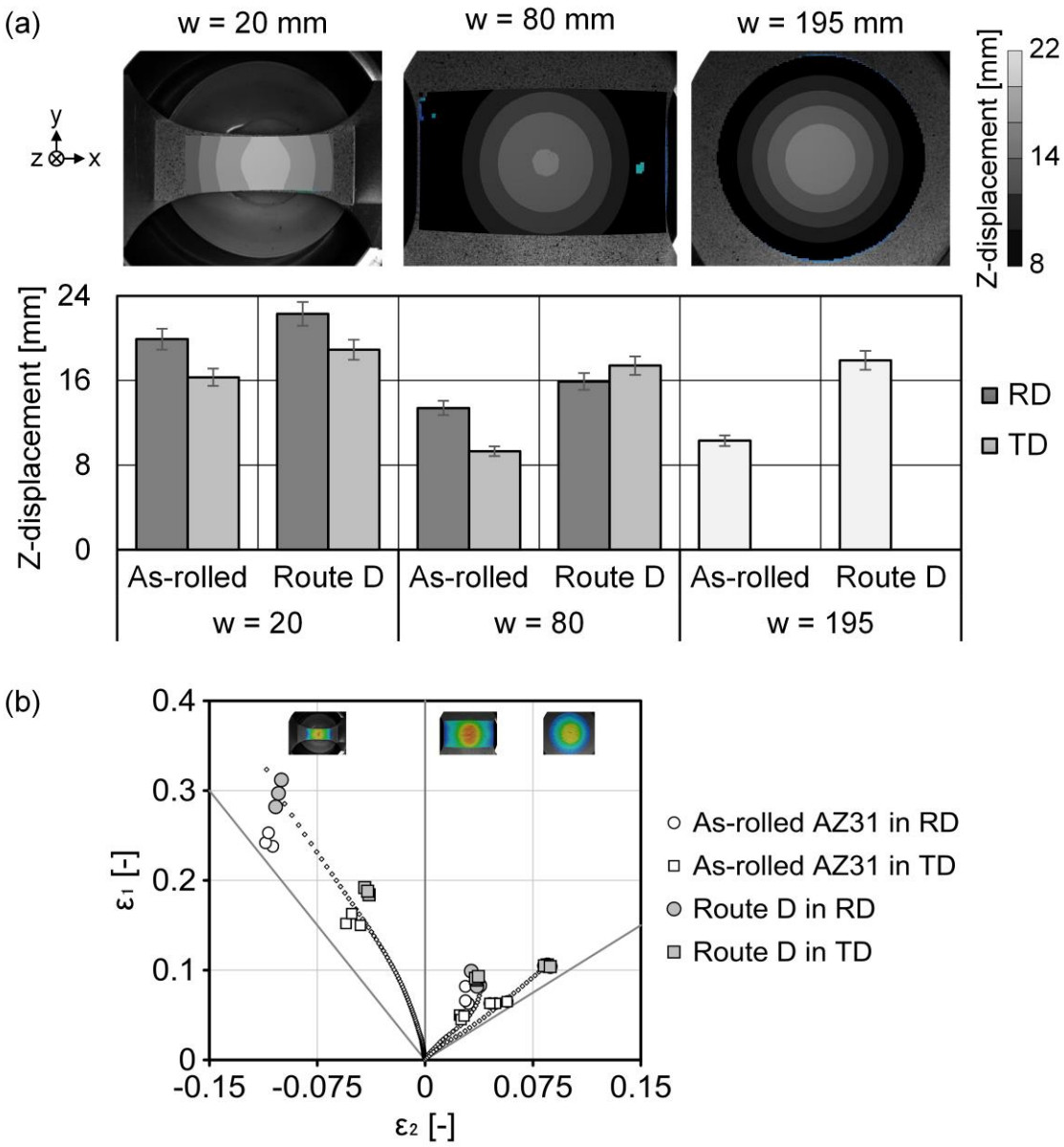

Figure 6.27: Comparison of forming depths and forming limit strains of as-rolled condition and route D regarding sample orientation: (a) comparison of z-displacement, (b) comparison of forming limit strains [SUH16-2]

For a more general evaluation of the cold formability, the forming limit strains are determined at room temperature using Nakajima tests. Before the comparison of the forming limits, the forming depths (z-displacement) of three specimen geometries are compared with respect to the sample orientation as depicted in Figure 6.27 (a). In the case of the simple tension condition (w = 20 mm), the forming depths on route D in the RD and TD are increased by 12 and 16% compared to the as-rolled sample, respectively. In the case of w = 80 mm, the z-displacement is enhanced by 19% in the RD

and particularly by 87% in the TD, respectively. Thus, both directions have a comparable value. Under biaxial tension (w = 195 mm), route D shows an explicit development of 74% compared to the as-rolled sample [SUH16-2].

In this connection, Figure 6.27 (b) presents that the forming limit strains on route D are compared with those of the rolled AZ31 sheet regarding the specimen orientations (RD and TD). As expected, both directions on route D have higher forming limit values than those of the rolled sheet. In comparison of the as-rolled sample, at w = 20 mm, the ε_1 on route D is improved by 22% in the RD and by 21% in the TD, respectively. At w = 80 mm, the ε_1 on route D is increased by 25% in the RD and especially by 90% in the TD. Under biaxial extension, the ε_1 is improved significantly by 65% after ECAP on route D [SUH16-2].

On route D, the forming limit strains in the RD and TD are in good agreement in the stretch forming area ($\varepsilon_1 > 0$ and $\varepsilon_2 > 0$). That is, the difference of the limit values between the RD and TD is reduced and their local instabilities are enhanced as compared to the rolled sheet. Nevertheless, there is a substantial difference between the limit strains in the deep drawing area ($\varepsilon_1 > 0$ and $\varepsilon_2 < 0$). In this area, the as-rolled sample and route D exhibit much higher forming capacity in the RD than in the TD. This result is not in an agreement with the tensile tests despite the enhanced hardening behavior and the reduced mechanical anisotropy. For this reason, a microstructure analysis is required to investigate the influence of the deformed microstructure on plastic instability and crack initiation [SUH16-2].

Figure 6.28 presents the cross-sectional SEM images of the fracture surfaces on the Nakajima specimens (w = 20 mm), which are deformed under uniaxial tension in the RD and TD, respectively [SUH16-2]. In the rolled sheet, a brittle-like fracture is observed with cleavage planes at tension in the RD, as shown in Figure 6.28 (a). After the uniaxial loading in the TD, the fractured sample also has brittle fracture with large shearing planes. Especially, large segregation particles are observed, which are pointed by the white arrow in Figure 6.28 (b). They are identified as Mg oxides using EDS. In the cross section, these impurities are aligned along the RD. This is characteristic for twin-roll cast Mg strips [BOHL15].

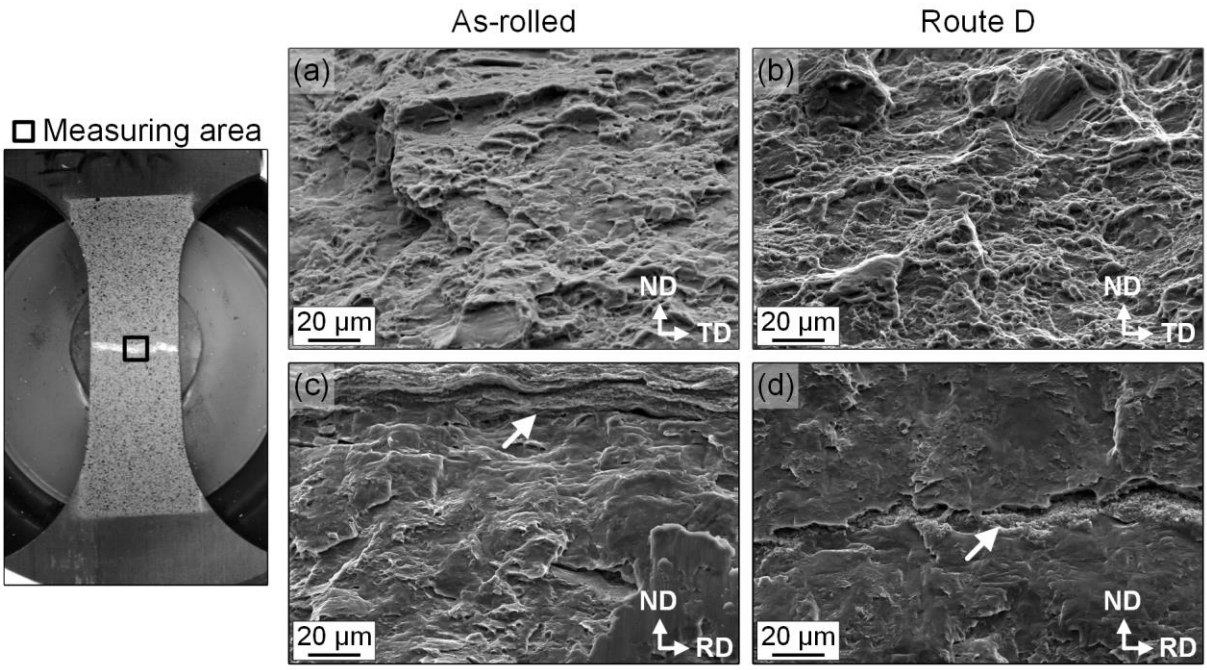

Figure 6.28: Cross-sectional SEM images of fractured Nakajima specimens with w = *20 mm: (a) and (c) for as-rolled condition, (b) and (d) for ECAPed sheet on route D under tension along RD and TD, respectively (white arrow: impurities such as Mg oxides) [SUH16-2]*

On route D, the sample shows an improvement in the ductility of the ECAPed sheet at tension in the RD. In Figure 6.28 (c), a substantial increase of dimples is observed on the fracture surface, which are typical for ductile fracture [ANDO14]. On the other hand, Figure 6.28 (d) presents that a brittle-type fracture occurs at the specimen deformed in the TD. Here the impurities such as Mg oxides are also observed, which are elongated along the RD. This is related with the crack initiation in a similar way to the rolled sheet. Based on this fractographic analysis, it can be concluded that the casting defect such as Mg oxide leads to the premature failure in the TD, resulting in an anisotropic forming capacity in the RD and TD at the Nakajima tests [SUH16-2].

Furthermore, it is also necessary to explain the considerable increase of the forming limit strain at biaxial stretching on route D [SUH16-2]. For this, the microscopic features of the fracture surfaces are analyzed using EBSD. Figure 6.29 (a) describes the measuring area of the fractured samples under biaxial extension (w = 195 mm). Special attention is paid to the activated twinning modes near the fracture surface, because deformation twinning has a considerable influence on the fracture behavior of Mg alloys [ANDO14]. In Figure 6.29 (b) and (C), the image quality (IQ) maps present the specific

twinning modes near the fracture surface of the rolled sheet and route D. In the IQ maps, three twinning modes are observed, where {10$\bar{1}$2} tension twins are highlighted in red, {10$\bar{1}$1} compression twins in yellow, and {10$\bar{1}$1}-{10$\bar{1}$2} double twins in green, respectively. Table 6.4 lists the area fraction of each twinning mode [SUH16-2].

In the as-rolled sample, {10$\bar{1}$1}-{10$\bar{1}$2} double twins are activated with area fraction of 7.8%. The occurrence of double twins is related to crack initiation sites [ANDO14, HART67, NIKN16, VICT14-2]. This twinning mode results from the increase in the resolved shear stresses on the basal slip systems. The crystal orientation induced by double twinning accompanies severe shear deformation, which leads to early void nucleation and transgranular fracture [VICT14-2]. In Figure 6.29 (b), double twins are marked with the white arrow near micro cracks, particularly in the coarse grain with a high volume of double twins. Victoria-Hernandez et al. [VICT14-2] reported the appearance of coarse elongated grains and double twins in a hot-rolled AZ31 sheet. It was found that pyramidal <c+a> slip, which also promotes the alignment of the c-axis nearly parallel to the ND, is related with the formation of coarse grain structure. In the as-rolled microstructure, the c-axis of most grains aligns predominantly parallel to the ND of Mg sheet. Such a preferred orientation of a strong texture stimulates the activation of {10$\bar{1}$1}-{10$\bar{1}$2} double twins under biaxial extension. At in-plane extension, compression is applied to the grain structure along the c-axis. This plays a role as the activation load of double and compression twins. On the other hand, Figure 6.29 (c) depicts that there is a drastic decrease in the fraction of double twins on route D (refer to Table 6.4). One of the main reasons is that the c-axis of the ECAPed sheets is tilted towards the PD. As a result, double twins and compression twins on route D are activated lower than the rolled sheet under biaxial stretching. For this reason, this microstructural change can enhance the ductility of the ECAPed sheets at room temperature. The fractographic analysis explicitly indicates that the activation of {10$\bar{1}$1}-{10$\bar{1}$2} double twins leads to premature failure in a macroscopically brittle manner. Therefore, the prevention of double twinning is essential for enhancing the cold formability of Mg sheets [SUH16-2].

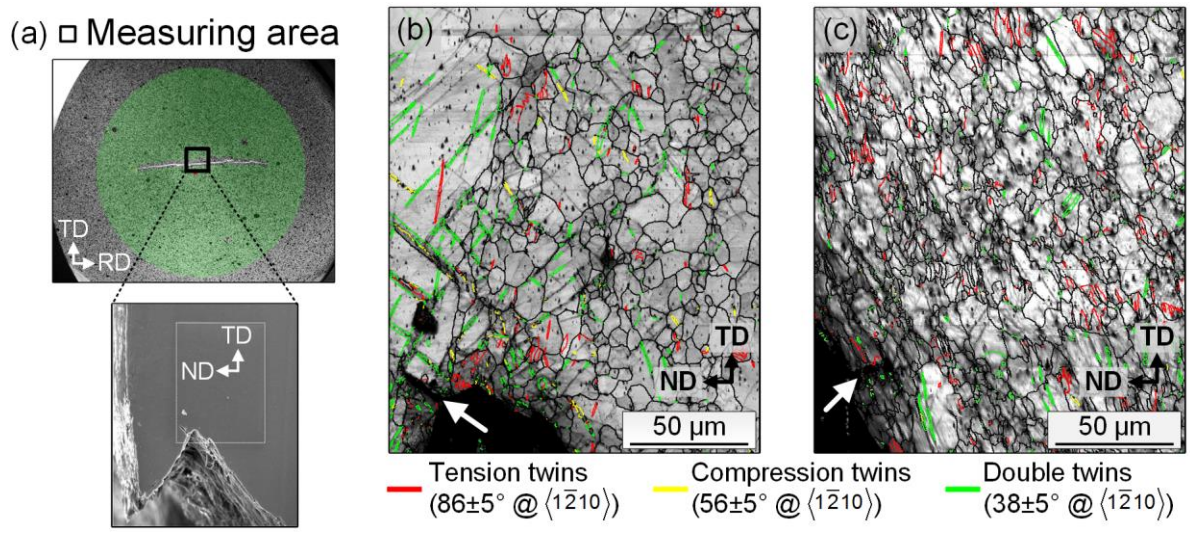

Figure 6.29: IQ maps on the fracture surfaces of Nakajima samples with w = 195 mm (bi-axial tension): (a) measuring area, (b) rolled sheet and (c) ECAPed sheet on route D [SUH16-2]

Twinning mode	***Rolled sheet [%]***	***Route D [%]***
{10$\bar{1}$2} tension twins	*3.8*	*3.4*
{10$\bar{1}$1} compression twins	*1.4*	*0.2*
{10$\bar{1}$1}-{10$\bar{1}$2} double twins	*7.8*	*2.6*

Table 6.4: Area fraction of microstructure consisting of {10$\bar{1}$2} tension, {10$\bar{1}$1} compression and {10$\bar{1}$1}-{10$\bar{1}$2} double twins from IQ maps [SUH16-2]

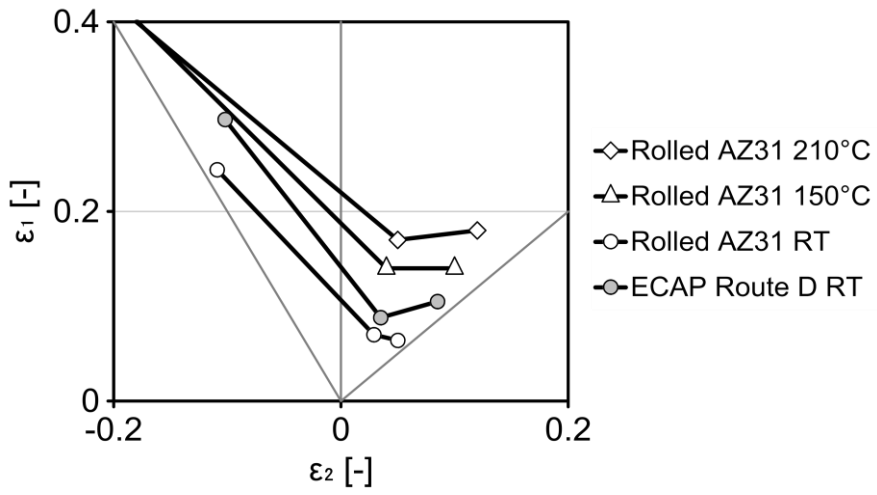

Figure 6.30: Comparison of forming limit curves at room temperature of as-rolled condition and route D with AZ31 sheet at 150 and 210 °C (thickness = 1.6 mm) [REDE09]

For the estimation of a potential to industrial applications, Figure 6.30 compares the FLC on route D with the FLCs of AZ31 sheet at 150 and 210 °C [REDE09]. Despite the improvement in the cold formability on route D, the forming limit strains on route D are much lower than other two cases. However, this study has two engineering significances: the first is to enhance the mechanical and forming behavior at room temperature of AZ31 sheet using ECAP, the second is to reduce the plastic anisotropy on the new presented route D by imposing shear strain along the RD and TD in the sheet plane. This knowledge can help apply ECAP to other Mg alloy sheets for the enhancement of their sheet formability at room temperature.

In view of the results so far achieved, cold formability of the ECAPed AZ31 sheets should be improved further coupled with microstructure and texture. To develop the sheet formability at room temperature, alloys having small or negligible anisotropy should be developed by suitable alloying elements and/or processing [SUH14]. That is, alloys exhibit a broadened but symmetric distribution of basal poles in sheet plane from the ND. Even though route D provides an almost isotropic hardening, the sheet formability should be enhanced further to a similar extent of the elongation in the RD on route C. The higher elongation in the RD on route C corresponds to its characteristic texture as described above, where the basal poles spread extensively across the RD, and hence the texture intensity is lowest. In this manner, the combination of route C and D can result in a reduction of mechanical anisotropy as well as higher formability at room temperature.

7 Summary and Outlook

This present work contributes to a basic understanding for the application of ECAP process to AZ31 Mg alloy sheets. For this, a novel tool is developed and AZ31 sheets are processed successfully with the various process parameters: processing temperature, channel angle and processing route. The microstructure and texture development is investigated, and the resulting mechanical properties are analyzed with the uniaxial tensile tests at room temperature. The enhanced cold formability is proven using the forming tests of a U-shaped channel. Finally, the sheet formability is evaluated and compared by the determination of the FLCs using Nakajima test.

First, a selectively heatable ECAP tool is developed for imposing shear strain on AZ31 sheets with dimensions 200 × 200 × 1.8 mm^3 at processing temperature up to 250 °C. There is no pre-heating of the sheet for the minimization of energy consumption. The locally heated tool components are segmented and adjusted so that the risk of unfavorable buckling or transverse loading can be avoided regarding thermal expansion. The temperature-induced changes in the dimensions and the positional accuracy are ensured by the insulation of the heated tool components from the tool frame and guide. The thermo-mechanical FE simulation demonstrates the functionality of the developed tool concept. The experimental measurements confirm these simulation results.

The AZ31 sheets processed by ECAP are in an acceptable state of reliability and quality without mechanical failure. During ECAP, dislocation slip and twinning become active at the intersection plane of the channel part. The area fraction of small grains increases and the fraction of coarse grains decreases significantly. The as-ECAPed samples exhibit a low pole density and a highly tilted texture component along the RD, which originates from the activation of $\{10\bar{1}2\}$ tension twins. The shear strain induced by ECAP inclines the c-axis of the hcp structure, and hence $\{10\bar{1}2\}$ tension twinning can be easily accommodated by the tension along the c-axis.

After ECAP, hot straightening is performed at 200 °C for 30 min for the homogenization and completely flat ECAPed sheets. These hot leveling conditions are determined by the analysis of the microstructure stability in terms of the heat treatment temperature

and duration. The texture is extremely strengthened again and an abnormal grain growth is observed at 250 °C. This indicates that the fraction of the twinned microstructure has a low thermal stability, which can reduce a potential to tailor the microstructure and texture of Mg-Al-Zn alloys. Regarding the homogenization and thermal stability of the ECAPed samples, the temperature for the hot leveling is set as 200 °C. The bent sheets are completely leveled after 30 min. The ECAPed samples and their material characteristics indicate the hot-leveled state in the above-determined conditions.

As one of the easiest controllable parameters, the effect of the processing temperature is investigated first at 175, 200 and 225°°C. ECAP makes more homogeneous and finer grain structure with increasing processing temperature. The average grain size at 225 °C is reduced from 15 to 8 µm in comparison of the rolled sheet. Dynamic recrystallization and texture weakening are observed after ECAP. Shear deformation makes the basal planes inclined along the RD, which is parallel to the PD. In this context, ECAP leads to a directional influence on the tensile properties at room temperature. In the RD, the YS is decreased by 45-60 MPa. Particularly, the ε_u of the ECAPed sheet at 225 °C is improved by 31% compared to the rolled sheet. This increase in the ε_u and decrease in the YS along the RD have a direct correlation with the enhanced activation of basal <a> slip.

After a single ECAP pass, the c-axis of many grains is obliquely aligned to the ECAP direction. This makes the activation energy for basal slip low, because the tilted c-axis is not parallel to the ND under in-plane extension. Therefore, the ECAPed microstructure has high Schmid factor, where grains orient to facilitate the activation of basal <a> slip. The rotation of grains and the low CRSS promote the activity of basal <a> slip during the tensile test. Consequently, higher ε_u and lower YS in the RD are observed than in the TD. With respect to the r_{10}, the larger tilt angle in the RD can also make easier the accommodation of the thickness strain. For this reason, the r_{10} in the RD is lower than in the TD at three processing temperatures.

The channel angle (Φ) is the most significant factor that determines directly the amount of the shear deformation in each pass. Higher shear deformation allows more refined microstructure, higher tilting of basal planes and activation of tension twins in the as-

ECAPed samples at 225 °C. In this context, the effect of higher shear deformation is evident from the increase in the ε_u in the RD with Φ = 110°. The uniform elongation is improved by 45 and 10% compared to the as-rolled condition and Φ = 130°, respectively. The higher improved ε_u in the RD with Φ = 110° can be attributed to higher work hardening, which is resulted from the suppressed dynamic recovery and twin-induced work hardening.

ECAP enables a multiple repetition so that higher shear strain leads to further development of the microstructure. This technique provides variations by a change of the sample orientation regarding shear direction. In comparison of the single pass, more homogenous microstructure develops through all three processing routes. Particularly, route C has the smallest average grain size. The initial coarse grains are subjected to repetitive deformations on the identical shear plane. This can leads to higher dislocation accumulation in the shear bands, and hence promote dynamic recrystallization process. On route C, the texture is weakened more markedly than the other routes and the basal poles are distributed visibly broadly across the RD. Processing on route A also leads to an increase in tendency for the basal poles to align along the RD. Processing on route D makes an almost symmetrical texture formation in the RD and TD. Particularly, the basal poles are rotated by ~15° towards 45° from the RD. This unique texture evolution has a distinct effect on the mechanical anisotropy.

In this regard, route C provides the highest ε_u in the RD among all samples, but there is no improvement of the ε_u in the TD. The suppressed dynamic recovery on route A and C helps maintain a high hardening rate. This leads to low sensitivity to the strain localization, and hence improves the ε_u. The texture altering and misorientation provide a more favorable orientation for basal slip and tension twinning. Therefore, high work hardening capacity and weakened texture enhance the ductility on route A and C. As expected, route D provides a comparable elongation in three tensile directions. The shear deformation along the TD induces the inclination of the basal planes as well as the activation of tension twins in the TD. The restrained dynamic recovery and twin-induced work hardening increase the ε_u in the TD to a similar extent of the RD and 45°. Consequently, route D allows an almost isotropic hardening of the ECAPed AZ31 sheet at room temperature.

In the forming tests of a U-shaped channel at room temperature, route C provides the highest forming depth in the RD and route D results in a comparable forming depth at the U-shaped strips. As predicted, this directional forming behavior at the U-shaped channel is in good agreement with the results of the uniaxial tensile test at room temperature. It is necessary to consider the correlation of sheet formability with r-values in a different way than cubic metals. Even though the r-value of the rolled sheet is twice larger than that of route C, route C exhibits a more enhanced forming behavior than the rolled sheet. This development can be attributed mainly to low r-value and high n-value induced by weakened texture in ECAP.

For a more general evaluation of the cold formability, the forming limit curves are determined at room temperature using Nakajima tests. Route D exhibits higher forming limit values than the as-rolled condition. The FLC in the RD and TD shows a good agreement in the stretch forming area. However, there is still large difference of the limit strains in the uniaxial tension area. Here, the rolled sheet and route D have much higher forming capacity in the RD than in the TD. SEM investigations present that the impurities such as Mg oxides make a contribution to brittle fracture behavior under uniaxial tension in the TD. This results in an anisotropic forming capacity in the RD and TD at the Nakajima tests. From the analysis of IQ maps, high activity of $\{10\bar{1}1\}$-$\{10\bar{1}2\}$ double twins leads to premature failure in the as-rolled sample under biaxial extension. Microstructure and texture development induced by ECAP can reduce the formation of double twins, and hence enhance the cold formability of AZ31 sheets. Despite the improvement in the cold formability, the FLCs on route D are much lower than that of AZ31 sheets at 150 and 210 °C However, this work is of central significance; processing of AZ31 sheet by ECAP can enhance mechanical and forming behavior at room temperature and reduce mechanical anisotropy.

Based on the results of ECAP process, the cold formability of the ECAPed AZ31 sheets should be improved further coupled with microstructure and texture. One approach is to strengthen the characteristic features of the routes C and D. In this manner, the combination of route C and D can lead to the reduction of mechanical anisotropy as well as higher formability at room temperature. Based on this, it can make application of ECAP to other Mg alloys such as AZ61 and ZE10. It is also necessary to determine

the limit value of the channel angle such as lower than 110°. Moreover, the forming performance of ECAPed sheets can be evaluated by deep drawing tests with different stamp geometries. This provides an evidence of the functionality for industry related applications. Finally, it is essential to investigate the requirements and process conditions for the mass production of ECAPed sheets in practice.

8 Index

8.1 List of figures

8.2 List of tables

8.3 List of literatures

[AGNE01] Agnew, S.; Yoo, M.H.; Tomé, C.N.:
Application of texture simulation to understanding mechanical behavior of Mg and solid solution alloys containing Li or Y
Acta Materialia, Vol. 49, pp. 4277–4289, 2001

[AGNE03] Agnew, S.R.; Tomé, C.N.; Brown, T.M.; Vogel, S.C.:
Study of slip mechanisms in a magnesium alloy by neutron diffraction and modeling
Scripta Materialia, Vol. 48, pp. 1003–1008, 2003

[AGNE04] Agnew, S.R.; Horton, J.A.; Lillo, T.M.; Brown, D.W.:
Enhanced ductility in strongly textured magnesium produced by equal channel angular processing
Scripta Materialia, Vol. 50, pp. 377–381, 2004

[AGNE05-1] Agnew, S.R.; Duygulu, O.:
Plastic anisotropy and the role of non-basal slip in magnesium alloy AZ31B
International Journal of Plasticity, Vol. 21, pp. 1161–1193, 2005

[AGNE05-2] Agnew, S.R.; Mehrotra, P.; Lillo, T.M.; Stoica, G.M.; Liaw, P.K.:
Texture evolution of five wrought magnesium alloys during route A equal channel angular extrusion: Experiments and simulations
Acta Materialia, Vol. 53, pp. 3135–3146, 2005

[AIDA01] Aida, T.; Matsuki, K.; Horita, Z.; Langdon, T.G.:
Estimating the equivalent strain in equal-channel angular pressing
Scripta Materialia, Vol. 44, pp. 575–579, 2001

[ANDO14] Ando, D.; Koike, J.; Sutou, Y.;
The role of deformation twinning in the fracture behavior and mechanism of basal textured magnesium alloys
Materials Science and Engineering A Vol. 600 pp. 145–152

[ARMS62] Armstrong, R.W.; Codd, I.; Douthwaite, R.M.; Petch, M.J.:
The plastic deformation of polycrystalline aggregates
Philoshopical Magazine, Vol. 7, pp. 45–58, 1962

[AVED99] Avedesian, M.M.; Backer, H.:
Magnesium and Magnesium Alloys (ASM Specialty Handbook)
ASM International, 1999

[AZUS08] Azushima, A.; Kopp, R.; Korhonen, A.; Yang, D.Y.; Micari, F.; Lahoti, G.D.; Groche, P.; Yanagimoto, J.; Tsuji, N.; Rosochowski, A.; Yanagida, A.:
Severe plastic deformation (SPD) processes for metals
CIRP Annals – Manufacturing Technology, Vol. 57, pp. 716–735, 2008

[BANA10] Banabic, D.:
Sheet Metal Forming Processes
Springer, Berlin Heidelberg, 2010

[BARN03] Barnett, M.R.:
A taylor model based description of the proof stress of magnesium AZ31 during hot working
Metallurgical and Materials Transactions A, Vol. 34, pp. 1799–1806, 2003

[BARN04] Barnett, M.R.; Keshavarz, Z.; Beer, A.G.; Atwell. D.:
Influence of grain size on the compressive deformation of wrought Mg–3Al–1Zn
Acta Materialia, Vol. 52, pp. 5093–5103, 2004

[BARN07] Barnett, M.R.:
Twinning and the ductility of magnesium alloys Part I: “Tension” twins
Materials Science and Engineering A, Vol. 464, pp. 1–7, 2007

[BENE08] Benedyk, J.C.:
Magnesium: where have we been, where are we going? – a 65 year retrospective on the use of magnesium
65th Annual World Magnesium Conference, Warsaw, 2008

[BOEH11] N. N.:
BÖHLER K890 MICROCLEAN®
Datasheet of BÖHLER Edelstahl GmbH & Co KG (http://www.bohler-edelstahl.com), 2011

[BOEH14] N. N.:
BÖHLER K390 MICROCLEAN®
Datasheet of BÖHLER Edelstahl GmbH & Co KG (http://www.bohler-edelstahl.com), 2014

[BOHL07] Bohlen, J.; Nürnberg, M.R.; Senn, J.W.; Letzig, D.; Agnew, S.R.:
The texture and anisotropy of magnesium–zinc–rare earth alloy sheets
Acta Materialia, Vol. 55, pp. 2101–2112, 2007

[BOHL10] Bohlen, J.; Yi, S.; Letzig, D.; Kainer, K.U.:
Effect of rare earth elements on the microstructure and texture development in magnesium – manganese alloys during extrusion
Materials Science and Engineering A, Vol. 527, pp. 7092–7098, 2010

[BOHL15] Bohlen, J.; Yi, S.; Victoria-Hernandez, J.; Schell, B.; Schwebke, B.; Brokmeier, H.G.; Kurz, G.; Letzig, D.:
in: M.V. Manuel, A. Singh, M. Alderman, N.R. Neelameggham (Eds.), Magnesium Technology 2015, pp. 476–176, 2015

[BRAV50] Bravais, A.:
Mémoire sur les systèmes formés par les points distribués régulièrement sur un plan ou dans l'espace
Journal de l'Ecole Polytechnique, Vol. 19, 1–128, 1850

[CARD08] Cardarelli, F.:
Materials handbook
Springer, London, 2008

[CHEN07] Cheng, Y.Q.; Chen, Z.H.; Xia, W.J.:
Drawability of AZ31 magnesium alloy sheet produced by equal channel angular rolling at room temperature
Materials Characterization, Vol. 58, pp. 617–622, 2007

[CHRI95] Christian, J.W.; Mahajan, S.:
Deformation twinning
Progress in Materials Science, Vol. 39, 1–157, 1995

[CUI96] Cui, Z.:
Science and Heat Treatment of Metal
Mechanical Industry Press of China, Beijing, pp. 205–207, 1996

[CZER08] Czerwinski, F.:
Magnesium injection molding
Springer, New York, 2008

[DAHL93] Dahl, W.; Kopp, R.; Pawelski, O.:
Umformtechnik – Plastomechanik und Werkstoffkunde
Springer, Berlin, 1993

[DELO99] Delo, D.P.; Semiatin, S.L.:
Hot working of Ti-6Al-4V via equal channel angular extrusion
Metallurgical and Materials Transactions A, Vol. 30, pp. 2473–2481, 1999

[DING09] Ding, S.X.; Chang, C.P.; Kao, P.W.:
Effects of processing parameters on the grain refinement of magnesium alloy by equal-channel angular extrusion
Metallurgical and Materials Transactions A, Vol. 40, pp. 415–425, 2009

[DOEG88] Doege, E.; Breidohr, B.:
Untersuchungen zum Tiefziehen von Teilen mit unebenen Bodenformen
EFB, 1998

[EIFE14-1] N. N.:
SUCASLIDE® - the carbon-coating from Eifeler
Datasheet of Eifeler Werkzeug GmbH (http://www.eifeler.com), 2014

[EIFE14-2] N. N.:
CrN / CrCN – chrome nitride / chrome carbon-nitride
Datasheet of Eifeler Werkzeug GmbH (http://www.eifeler.com), 2014

[EMBU89] Embury, J.D.; Lloyd, D.J.; Ramachandran, T.R.:
in: A.K. Vasudevan, R.D. Doherty (Eds.), Aluminum Alloys–Contemporary Research and Applications
Treatise on Materials Science and Technology, Vol. 31, Academic Press, Inc., Boston, USA, 1989

[ENSS01] Enß, J.; Juchmann, P.; Evertz, T.; Schumann, S.; Reier, T.; Sebastian, W.:
Neue Magnesium-Blechprodukte für den Automobilbau
ATZ Automobiltechnische Zeitschrift, Vol. 103, pp. 142–145, 2001

[ESTR13] Estrin, Y.; Vinogradov, A.:
Extreme grain refinement by severe plastic deformation: a wealth of challenging science
Acta Materialia, Vol. 61, pp. 782–817, 2013

[FERR04] Ferrasse, S.; Segal, V.M.; Kalidindi, S.R.; Alford, F.:
Texture evolution during equal channel angular extrusion: Part I. Effect of route, number of passes and initial texture
Materials Science and Engineering A, Vol. 368, pp. 28–40, 2004

[FIGU09] Figueiredo, R.B.; Langdon, T.G.:
Principles of grain refinement in magnesium alloys processed by equal-channel angular pressing
Journal of Materials Science, Vol. 44, pp. 4758–4762, 2009

[FIGU10-1] Figueiredo, R.B.; Langdon, T.G.:
Grain refinement and mechanical behavior of a magnesium alloy processed by ECAP
Journal of Materials Science, Vol. 45, pp. 4827–4836, 2010

[FIGU10-2] Figueiredo, R.B.; Beyerlein, I.J.; Zhilyaev, A.P.; Langdon, T.G.:
Evolution of texture in a magnesium alloy processed by ECAP through dies with different angles
Materials Science and Engineering A, Vol. 527, pp. 1709–1718, 2010

[FRIE06] Friedrich, H.E.; Mordike, B.L.:
Magnesium technology
Springer, Berlin, 2006

[FURU01] Furukawa, M.; Horita, Z.; Nemoto, M.; Langdon, T.G.:
Review processing of metals by equal-channel angular pressing
Journal of Materials Science, Vol. 36, pp.2835–2843, 2001

[FURU02] Furukawa, M.; Horita, Z.; Langdon, T.G.:
Factors influencing the shearing patterns in equal-channel angular pressing
Materials Science and Engineering A, Vol. 332, pp. 97–109, 2002

[GHOL00] Gholinia, A.; Prangnell, P.B.; Markushev, M.V.:
The effect of strain path on the development of deformation structures in severely deformed aluminium alloys processed by ECAE
Acta Materialia, Vol. 48, pp. 1115–1130, 2000

[GHOS84] Ghosh, A.K.; Hecker, S.S.; Keeler, S.P.:
In: GE Dieter, ed. Workability Testing Techniques
Ohio: ASM International, Materials Park, pp. 135–195, 1984

[GOFO00] Goforth, R.E.; Hartwig, K.T.; Cornwell, L.R.:
Severe Plastic Deformation of Materials by Equal Channel Angular Extrusion (ECAE)
Investigations and Applications of Severe Plastic Deformation, Vol. 80, pp. 3–12, 2000

[GOOD14] Goodarzy, M.H.; Arabi, H.; Boutorabi, M.A.; Seyedein, S.H.; Hasani Najafabadi, S.H.:
The effects of room temperature ECAP and subsequent aging on mechanical properties of 2024 Al alloy
Journal of Alloys and Compounds, Vol. 585, pp. 753–759, 2014

[GOTT07] Gottstein, G.:
Physical Foundations of Materials Science
Springer-Verlag, Berlin, 3. Auflage, 2007

[HADA13] Hadadzadeh, A.; Wells, M.A.:
Mathematical modeling of thermo-mechanical behavior of strip during twin roll casting of an AZ31 magnesium alloy
Journal of Magnesium and Alloys, Vol. 1, pp. 101–114, 2013

[HALL51] Hall, E.O.:
The Deformation and Ageing of Mild Steel: III Discussion of Results
Proceedings of the Physical Society, Vol. 64, pp. 747–753, 1951

[HAOU05] Haouaoui, M.; Hartwig, K.T.; Payzant, E.A.:
Effect of strain path on texture and annealing microstructure development in bulk pure copper processed by simple shear
Acta Materialia, Vol. 53, pp. 801–810, 2005

[HART67] Hartt, W.H.; Reed-Hill, R.E:
The internal habit of second-order $\{10\bar{1}1\}$-$\{10\bar{1}2\}$ twins in magnesium
Transactions of the Metallurgical Society of AIME Vol. 239, pp.1511-1517, 1967

[HIBB00] Hibbeler, R.C.:
Mechanics of Materials
Prentice Hall, Inc., New Jersey, 2000

[HIEL08] Hielscher, R.; Schaeben, H.:
A novel pole figure inversion method: specification of the MTEX algorithm
Journal of Applied Crystallography, Vol. 41, pp. 1024–1937, 2008

[HIRS13] Hirsh, J.; Al-Samman, T.:
Superior light metals by texture engineering: Optimized aluminium and magnesium alloys for automotive applications
Acta Materailia, Vol. 61, pp. 818–843, 2013

[HIRS65] Hirsch, P.B.; Lally, J.S.:
The deformation of magnesium single crystals
Philosophical Magazine, Vol. 12, pp. 595–648, 1965

[HORN93] Hornbogen, E.; Stark, E.A. Jr.:
Overview no. 102 Theory assisted design of high strength low alloy aluminum
Acta Metallurgica et Materialia, Vol. 41, pp. 1–16, 1993

[HOSF07] Hosford, W.F.; Caddell, R.M.:
Metal forming: mechanics and metallurgy
Cambridge University Press, 2007

[HUAN08] Huang, X.; Suzuki, K.; Watazu, A.; Shigematsu, I.; Saito, N.:
Mechanical properties of Mg–Al–Zn alloy with a tilted basal texture obtained by differential speed rolling
Materials Science and Engineering A, Vol. 488, pp. 214–220, 2008

[HUAN09] Huang, X.; Suzuki, K.; Watazu, A.; Shigematsu, I.; Saito, N.:
Microstructural and textural evolution of AZ31 magnesium alloy during differential speed rolling
Journal of Alloys and Compounds, Vol. 479, pp. 726–731, 2009

[HUAN11] Huang, X.; Suzuki, K.; Chino, Y.; Mabuchi, M.:
Improvement of stretch formability of Mg–3Al–1Zn alloy sheet by high temperature rolling at finishing pass
Journal of Alloys and Compounds, Vol. 509, pp. 7579–7584, 2011

[HUAN13] Huang, X.; Suzuki, K.; Chino, Y.:
Different annealing behaviours of warm rolled Mg–3Al–1Zn alloy sheets with dynamic recrystallized microstructure and deformation microstructure
Materials Science and Engineering A, Vol. 560, pp. 232–240, 2013

[HUPP11] Huppmann, M.:
Charakterisierung der Verformungsmechanismen der stranggepressten Magnesiumlegierungen AZ31 und ME21 unter monotoner und zyklischer Belastung
Ph.D. thesis, TU Berlin, 2011

[ION82] Ion, S.E.; Humphreys, F.J.; White, S.H.:
Dynamic recrystallization and the development of microstructure during the high temperature deformation of magnesium
Acta Metallurgica, Vol. 30, pp. 1909–1919, 1982

[IWAH96] Iwahashi, Y.; Wang, J.; Horita, Z.; Nemoto, M.; Langdon, T.G.:
Principle of equal-channel angular pressing for the processing of ultra-fine grained materials
Scripta Materialia, Vol. 35, pp. 143–146, 1996

[IWAH98] Iwahashi, Y.; Horita, Z.; Nemoto, M.; Langdon, T.G.:
The process of grain refinement in equal-channel angular pressing
Acta Materialia, Vol. 46, pp.3317–3331, 1998

[JIN05] Jin, L.; Lin, D.L.; Mao, D.M.; Zeng, X.Q.; Ding, W.J.:
Mechanical properties and microstructure of AZ31 Mg alloy processed by two-step equal channel angular extrusion
Materials Letters, Vol. 59, pp. 2267–2270, 2005

[JUFU10] Jufu, J.; Ying, W.; Zhiming, D.; Jianjun, Q.; Yi, S.; Shoujing, L.:
Enhancing room temperature mechanical properties of Mg-9Al-Zn alloy by multi-pass equal channel angular extrusion
Journal of Materials Processing Technology, Vol. 210, pp. 751–758, 2010

[JUNG13] Jung, H.S.:
Konstruktion eines ECAP-Werkzeugs zur Texturoptimierung von Magnesiumblechen der Knetlegierung AZ31
Master thesis, TU München, 2013

[KAIS03] Kaiser, F.; Bohlen, J.; Letzig, D.; Styczynski, A.; Hartig, Ch.; Kainer, K. U.:
Anisotropic properties of magnesium sheet AZ31
Materials Science Forum, Vol. 419–422, pp. 315-320, 2003

[KAIS05] Kaiser F.:
Zum Anisotropieverhalten der gewalzten Magnesiumknetlegierung AZ31
Ph. D. thesis, Universität Hamburg-Harburg, 2005

[KAMM00] Kammer, C.:
Magnesium Taschenbuch
Aluminium-Verlag, Düsseldorf, 2000

[KAMM02] Kammer, C.:
Aluminium Taschenbuch, Band 1 Grundlagen und Werkstoffe
Aluminium-Verlag, Düsseldorf, 2002

[KANG08] Kang, S.H.; Lee, Y.S.; Lee, J.H.:
Effect of grain refinement of magnesium alloy AZ31 by severe plastic deformation on material characteristics
Journal of Materials Processing Technology, Vol. 201, pp. 436–440, 2008

[KIM00] Kim, H.S.; Seo, M.H.; Hong, S.I.:
On the die corner gap formation in equal channel angular pressing
Materials Science and Engineering A, Vol. 291, pp. 86–90, 2000

[KIM03] Kim, W.J.; Hong, S.I.; Kim, Y.S.; Min, S.H.; Jeong, H.T.; Lee, J.D.:
Texture development and its effect on mechanical properties of an AZ61 Mg alloy fabricated by equal channel angular pressing
Acta Materialia, Vol. 51, pp. 3293–3307, 2003

[KIM05] Kim, W.J.; Jeong, H.T.:
Grain-Size Strengthening in Equal-Channel-Angular-Pressing Processed AZ31 Mg Alloys with a Constant Texture
Materials Transactions, Vol. 46, pp. 251–258, 2005

[KLEI02] Kleiner, S.:
Magnesium und seine Legierungen
6. Internationales IWF-Kolloquium, Egerkingen, Schweiz, 2002

[KOCK67] Kocks, U.F.; Westlake, D.G.:
The importance of twinning for the ductility of CPH polycrystals
Transactions of the Metallurgical Society of AIME, Vol. 239, pp. 1107–1109, 1967

[KOIK03] Koike, J.; Kobayashi, T.; Mukai, T.; Watanabe, H.; Suzuki, M.; Maruyama, K.; Higashi, K.:
The activity of non-basal slip systems and dynamic recovery at room temperature in fine-grained AZ31B magnesium alloys
Acta Materialia, Vol. 51, pp. 2055–2065, 20003

[LANG90] Lange, K.:
Umformtechnik Handbuch für Industrie und Wissenschaft; Vol. 3 Blechbearbeitung
Springer, Berlin, 1990

[LAPO08] Lapovok, R.; Timokhina, I.; McKenzie, P.W.J.; O'Donnel, R.:
Processing and properties of ultrafine-grain aluminium alloy 6111 sheet
Journal of Materials Processing Technology, Vol. 200, pp. 441–450, 2008

[LEE00] Lee, D.Y.:
An upper-bound solution of channel angular deformation
Scripta Materialia, Vol. 43, pp. 115–118, 2000

[LEE84] Lee, D.N.:
Relation between limiting drawing ratio and plastic strain ratio
Journal of Materials Science Letters, Vol. 3, pp. 677–680, 1984

[LEIC14] N. N.:
Leica DMI 5000
Datasheet of Leica Microsystems GmbH (http://www.leica-microsystems.com), 2014

[LI04] Li, D.; Ghosh, A.:
Biaxial warm forming behavior of aluminum sheet alloys
Journal of Materials Processing Technology, Vol. 145, pp. 281–293, 2004

[LIU03] Liu, M.Y.; Shi, B.; Wang, C.; Ji, S.K.; Cai, X.; Song, H.W.:
Normal Hall–Petch behavior of mild steel with submicron grains
Materials Letter, Vol. 57, pp. 2798–2802, 2003

[LUO07] Luo, A.A.; Sachdev, A.K.:
Development of a new wrought magnesium-aluminum-manganese alloy AM30
Metallurgical and Materials Transactions A, Vol. 38, pp. 1184–1192, 2007

[LUO95] Luo, Z.P.; Song, D.Y.; Zhang, S.Q.:
Strengthening effects of rare earths on wrought Mg-Zn-Zr-RE alloys
Journal of Alloys and Compounds, Vol. 230 pp. 109–114, 1995

[LUIS04] Luis Pérez, C.J.:
On the correct selection of the channel die in ECAP processes
Scripta Materialia, Vol. 50, pp. 387–393, 2004

[MABU97] Mabuchi, M.; Iwasaki, H.; Yanase, K.; Higashi, K.:
Low temperature superplasticity in an AZ91 magnesium alloy processed by ECAE
Scripta Materialia, Vol. 36, pp. 681–686, 1997

[MACK08] Mackenzie, L.W.F.; Pekguleryuz, M.:
The influences of alloying additions and processing parameters on the rolling microstructures and textures of magnesium alloys
Materials Science and Engineering A, Vol. 480, pp. 189–197, 2008

[MEYE01] Meyers, M.A.; Vöhringer, V.; Lubarda, A.:
The onset of twinning in metals: a constitutive description
Acta Materialia, Vol. 49, pp. 4025–4039, 2001

[MILL39] Miller, W.H.:
A treatise on crystallography
For J. & J. J. Deighton, Cambridge, 1839

[MISE28] Mises, R.V.:
Mechanik der plastischen Formänderung von Kristallen
Zeitschrift für Angewandte Mathematik und Mechanik, Vol. 8, pp. 161–185, 1928

[MORD01] Mordike, B.L.; Ebert, T.:
Magnesium properties - applications - potential
Materials Science and Engineering A, Vol. 302, pp. 37–45, 2001

[MUKA01] Mukai, T.; Yamanoi, M.; Watanabe, H.; Higashi, K.:
Ductility enhancement in AZ31 magnesium alloy by controlling its grains structure
Scripta Materialia, Vol. 45, pp. 89–94, 2001

[NAVE04] Nave, M.D.; Barnett, M.R.:
Microstructures and textures of pure magnesium deformed in plane-strain compression
Scripta Materialia, Vol. 51, pp. 881–885, 2004

[NEBE09] Nebebe, M.; Bohlen, J.; Steglich, D.; Letzig, D.:
Mechanical characterization of Mg alloys and model parameter identification for sheet forming simulations
International Journal of Material Forming, Vol. 2, pp. 53–56, 2009

[NGUY14] Nguyen, N.-T.; Seo, O.S.; Lee, C. An.; Lee, M.-G.; Kim, J.-H.; Kim, H.Y.:
Mechanical behavior of AZ31B Mg Alloy sheets under monotonic and cyclic loadings at room and moderately elevated temperatures
Materials, Vol. 7, pp. 1271–1295, 2014

[NIE13] Nie, J.F.; Zhu, Y.M.; Liu, J.Z.; Fang, X.Y.:
Periodic segregation of solute atoms in fully coherent twin boundaries
Science, Vol. 340, pp. 957–960, 2013

[NIKN16] Niknejad, S.; Esaneili, S.; Zhou, N.Y.:
The role of double twinning on transgranular fracture in magnesium AZ61 in a localized stress field
Acta Materialia, Vol. 102, pp. 1–16, 2016

[NUER10] Nürnberg, G.:
Untersuchungen zum Scherschneiden von Magnesiumblech unter Serienbedingungen
Ph.D. thesis, TU München, 2010

[ONO03] Ono, N.; Nakamura, K.; Miura, S.:
Influence of Grain Boundaries on Plastic Deformation in Pure Mg and AZ31 Mg Alloy Polycrystals
Materials Science Forum, Vol. 419-422, pp. 195–200, 2003

[OSTE07] Ostermann, F.:
Anwendungstechnologie Aluminum
Springer, Berlin, 2007

[PANA14] N. N.:
PANalytical X'Pert PRO system
Datasheet of PANalytical B. V. (www.panalytical.com), 2014

[PART67] Partridge, P.G.:
The crystallography and deformation modes of hexagonal close packed metals
International Materials Reviews, Vol. 12, pp. 169–194, 1967

[PERE04] Pérez-Prado, M.T.; del Valle, J.A.; Contreras, J.M.; Ruano, O.M.:
Microstructural evolution during large strain hot rolling of an AM60 Mg alloy
Scripta Materialia, Vol. 50, pp. 661–665, 2004

[PETC53] Petch, N.J.:
The Cleavage Strength of Polycrystals
Journal : Iron and Steel Institute, Vol. 173, pp. 25-28, 1953

[PHIL94] Philippe, M.J.:
Texture Formation in Hexagonal Materials
Materials Science Forum, Vol. 157–162, pp. 1337–1350, 1994

[RADI10] Radi, Y.; Mahmudi, R.:
Effect of Al_2O_3 nano-particles on the microstructural stability of AZ31 Mg alloy after equal channel angular pressing
Materials Science and Engineeing A, Vol. 527, pp. 2764–2771, 2010

[REDE09] Redecker, M.:
Erweiterte Ermittlung der Umformeigenschaften von Magnesiumfeinblechen
Ph.D. thesis, TU München, 2009

[REED60] Reed-Hill, R.E.:
A study of the twinning modes in magnesium
Transactions of the Metallurgical Society of AIME, Vol. 218, pp. 554–558, 1960

[ROBE60] Roberts, C.S.:
Magnesium and Its Alloys
Wiley, New York, 1960

[SAIT99] Saito, Y.; Utsunomiya, H.; Tsuji, N.; Sakai, T.:
Novel ultra-high straining process for bulk materials – development of the accumulative roll-bonding (ARB) process
Acta Materialia, Vol. 47, pp. 579–583, 1999

[SAKA14] Sakai, T., Belyakov, A., Kaibyshev, R., Miura, H., Jonas, J.J.:
Dynamic and post-dynamic recrystallization under hot, cold and severe plastic deformation conditions
Progress in Materials Science, Vol. 60, pp. 130–207. 2014

[SCHM35] Schmid, E.:
Kristallplastizität: Mit Besonderer Berücksichtigung der Metalle
Springer, Berlin Heidelberg, 1935

[SEGA81] Segal, V.M.; Reznikov, V.I.; Drobyshevski, A.E.; Kopylov, V.I.:
Plastic working of metals by simple shear
Russian Metallurgy, Vol. 1, pp. 99–105, 1981 (English translation)

[SHAE15] Shaeri, M.H.; Shaeri, M.; Salehi, M.T.; Seyyedein, S.H.; Abutalebi, M.R.:
Effect of equal channel angular pressing on aging treatment of Al-7075 alloy
BYProgress in Natural Science: Materials International, Vol. 25, pp. 159-168, 2015

[SHAN99] Shan, A.; Moon, I.G.; Ko, H.S.; Park, J.W.:
Direct observation of shear deformation during equal channel angular pressing of pure aluminum
Scripta Materialia, Vol. 41, pp. 353–357, 1999

[STAR98] Staroselsky, A.V.:
Crystal plasticity due to slip and twinning
Ph.D. thesis, Massachusetts Institute of Technology, 1998

[STRA14] Stráská, J.; Janecek, M.; Cízek, J.; Stráský, J.; Hadzima, B.:
Microstructure stability of ultra-fine grained magnesium alloy AZ31 processed by extrusion and equal-channel angular pressing (EX–ECAP)
Materials Characterization, Vol. 94, pp. 69–79, 2014

[STYC04] Styczynski, A.; Hartig, C.; Bohlen, J.; Letzig, D.:
Cold rolling textures in AZ31 wrought magnesium alloy
Scripta Materialia, Vol. 50, pp. 943–947, 2004

[SUH14] Suh, B.C.; Shim, M.S.; Shin, K.S.; Kim, N.J.:
Current issues in magnesium sheet alloys: Where do we go from here?
Scripta Materialia, Vol. 84–85, pp. 1–6, 2014

[SUH15] Suh, J.; Victoria-Hernandez, J.; Letzig, D.; Golle, R.; Yi, S.; Bohlen, J.; Volk, W.:
Improvement in cold formability of AZ31 magnesium alloy sheets processed by equal channel angular pressing
Journal of Materials Processing Technology, Vol. 217, pp. 286–293, 2015

[SUH16-1] Suh, J.; Victoria-Hernandez, J.; Letzig, D.; Golle, R.; Volk, W.:
Enhanced mechanical behavior and reduced mechanical anisotropy of AZ31 Mg alloy sheet processed by ECAP
Materials Science and Engineering A, Vol. 650, pp. 523–529, 2016

[SUH16-2] Suh, J.; Victoria-Hernandez, J.; Letzig, D.; Golle, R.; Volk, W.:
Effect of processing route on texture and cold formability of AZ31 Mg alloy sheets processed by ECAP
Materials Science and Engineering A, under review

[SUN07] Sun, P.L.; Cerreta, E.K.; Bingert, J.F.; Gray III, G.T.; Hundley, M.F.:
Enhanced tensile ductility through boundary structure engineering in ultrafine-grained aluminum
Materials Science and Engineeing A, Vol. 464, pp. 343–350, 2007

[SUWA07] Suwas, S.; Gottstein, G.; Kumar, R.:
Evolution of crystallographic texture during equal channel angular extrusion (ECAE) and its effects on secondary processing of magnesium
Materials Science and Engineeing A, Vol. 471, pp. 1–14, 2007

[SUWA14] Suwas, S.; Ray, R.K.:
Crystallographic Texture of Materials
Springer-Verlag, London, 2014

[TONG10] Tong, L.B.; Zheng, M.Y.; Hu, X.S.; Wu, K.; Xu, S.W.; Kamado, S.; Kojima, Y.:
Influence of ECAP routes on microstructure and mechanical properties of Mg–Zn–Ca alloy
Materials Science and Engineeing A, Vol. 527, pp. 4250–4256, 2010

[VALI04] Valiev, R.Z.:
Nanostructuring of metals by severe plastic deformation for advanced properties
Nature Materials, Vol. 3, pp. 511–516, 2004

[VALI06] Valiev, R.Z.; Langdon, T.G.:
Principles of equal-channel angular pressing as a processing tool for grain refinement
Progress in Materials Science, Vol. 51, 881–981, 2006

[VALL06] del Valle, J.A.; Carreno, F.; Ruano, O.A.:
Influence of texture and grain size on work hardening and ductility in magnesium-based alloys processed by ECAP and rolling
Acta Materialia, Vol. 54, pp. 4247–4259, 2006

[VICT13] Victoria-Hernandez, J.; Yi, S.; Letzig, D.; Hernandez-Silva, D.; Bohlen, J.:
Microstructure and texture development in hydrostatically extruded Mg–Al–Zn alloys during tensile testing at intermediate temperatures
Acta Materialia, Vol. 61, pp. 2179–2193, 2013

[VICT14-1] Victoria-Hernandez, J.; Suh, J.; Bohlen, J.; Yi, S.; Kurz, G.; Golle, R.; Volk, W.; Letzig, D.:
Microstructural Stability Analysis of Mg 3Al 1Zn Sheets Deformed by Equal Channel Angular Pressing
ISMANAM 2014, Cancún, 2014

[VICT14-2] Victoria-Hernandez, J.; Yi, S.; Bohlen, J.; Kurz, G.; Letzig, D.:
The influence of the recrystallization mechanisms and grain growth on the texture of a hot rolled AZ31 sheet during subsequent isochronal annealing
Journal of Alloys and Compounds, Vol. 616, pp. 189–197, 2014

[VOLK10] Volk, W.; Hora, P.:
New algorithm for a robust user-independent evaluation of beginning instability for the experimental FLC determination
International Journal of Material Forming, Vol. 4, pp. 339–346, 2010

[VOLK12] Volk, W.; Hoffmann, H.; Suh, J.; Kim, J.:
Failure prediction for nonlinear strain paths in sheet metal forming
CIRP Annals – Manufacturing Technology, Vol. 61, pp. 259–262, 2012

[WAGN03] Wagner, L.; Hilpert, M.; Wendt, J.: Küster, B.:
On methods for improving the fatigue performance of the wrought magnesium alloys AZ31 and AZ80
Materials Science Forum, Vol. 419–422, pp. 93–102, 2003

[WATA04-1] Watari, H.; Davey, K.; Rasgado, M.T.; Haga, T.; Izawa, S.:
Semi-solid manufacturing process of magnesium alloys by twin-roll casting
Journal of Materials Processing Technology, Vol. 155–156, pp. 1662–1667, 2004

[WATA04-2] Watanabe, H.; Mukai, T.; Ishikawa, K.:
Differential speed rolling of an AZ31 magnesium alloy and the resulting mechanical properties
Journal of Materials Science, Vol. 39, pp. 1477–1480, 2004

[WATA07] Watanabe, H.; Mukai, T.; Ishikawa, K.:
Effect of temperature of differential speed rolling on room temperature mechanical properties and texture in an AZ31 magnesium alloy
Journal of Materials Processing and Technology, Vol. 182, pp. 644–647, 2007

[WAYC14] N. N.:
Linear Potentiometers LRW
Datasheet of WayCon Positionsmesstechnik GmbH (http://www.waycon.biz), 2014

[WEI04] Wei, Q.; Cheng, S.; Ramesh, K.T.; Ma, E.:
Effect of nanocrystalline and ultrafine grain sizes on the strain rate sensitivity and activation volume: fcc versus bcc metals
Materials Science and Engineeing A, Vol. 381, pp. 71–79, 2004

[WU11] Wu, D.; Chen, R.S.; Han, E.H.:
Excellent room-temperature ductility and formability of rolled Mg-Gd-Zn alloy sheets
Journal of Alloys and Compounds, Vol. 509, pp. 2856–2863, 2011

[XIAO13] Xiaohui, L.:
Enhanced ductility of Mg alloys containing rare earth elements
Ph.D. thesis, RWTH Aachen University, 2013

[YI05] Yi, S.:
Investigation of the deformation behavior and the texture evolution in magnesium wrought alloy AZ31
Ph.D. thesis, TU Claustahl, 2005

[YI09] Yi, S.; Schestakow, I.; Zaefferer, S.:
Twinning-related microstructural evolution during rolling and subsequent annealing of pure magnesium
Materials Science and Engineering A, Vol. 516, pp. 56–64, 2009

[YI10] Yi, S.; Bohlen, J.; Heinemann, F.; Letzig, D.:
Mechanical anisotropy and deep drawing behaivour of AZ31 and ZE10 magnesium alloy sheets
Acta Materialia, Vol. 58, pp. 592–605, 2010

[YOO02] Yoo, M.H.; Morris, J.R.; Ho, K.M.; Agnew, S.R.:
Nonbasal deformation modes of HCP metals and alloys: role of dislocation source and mobility
Metallurgical and Materials Transactions A, Vol. 33, pp. 813–822, 2002

[YOO81] Yoo, M.H.:
Slip, twinning and fracture in hexagonal close packed metals
Metallurgical Transactions A, Vol. 12, pp. 409–418, 1981

[YUAN04] Yuanyuan, L.; Datong, Z.; Weiping, C.; Ying, L.; Guowen, G.:
Microstructure evolution of AZ31 magnesium alloy during equal channel angular extrusion
Journal of Materials Science, Vol. 39, pp. 3759–3761, 2004

[YUKU03] Yukutake, E.; Kaneko, J.; Sugamata, M.:
Anisotropy and non-uniformity in plastic behavior of AZ31 Magnesium alloy plates
Materials Transactions, Vol. 44, pp. 452–457, 2003

[ZEIS14] N. N.:
ZEISS SIGMA Series
Datasheet of Carl Zeiss Microscopy GmbH (http://www.zeiss.com), 2014

[ZHIL08] Zhilyaev, A. P.; Langdon, T. G.:
Using high-pressure torsion for metal processing: Fundamentals and applications
Progress in Materials Science, Vol. 53, pp. 893–979, 2008

8.4 Standards and guidelines

[ASTM B275-05] ASTM B275-05
Standard Practice for Codification of Certain Nonferrous Metals and Alloys, Cast and Wrought
ASTM International, USA, (http://www.astm.org)

[DIN 10002-1] DIN EN 10002-1:2001
Metallic materials - Tensile testing - Part 1: Method of test at ambient temperature
Deutsches Institut für Normung e.V., Beuth-Verlag, Berlin, 2001

[DIN 50125] DIN EN 50125:2009-07
Testing of metallic materials - Tensile test pieces
Deutsches Institut für Normung e.V., Beuth-Verlag, Berlin, 2009

[ISO 10113] ISO 10113:2006
Metallic materials - Sheet and strip - Determination of plastic strain ratio
Deutsches Institut für Normung e.V., Beuth-Verlag, Berlin, 2006

[ISO 12004-2] DIN EN ISO 12004-2:2009
Metallic materials -- Sheet and strip -- Determination of forming-limit curves -- Part 2: Determination of forming-limit curves in the laboratory
Deutsches Institut für Normung e.V., Beuth-Verlag, Berlin, 2009

9 Appendix

Code letter	*Element*	*Code letter*	*Element*
A	*Aluminum*	*M*	*Manganese*
B	*Bismuth*	*N*	*Nickel*
C	*Cupper*	*P*	*Lead*
D	*Cadmium*	*Q*	*Silber*
E	*Rare earth*	*R*	*Chrome*
F	*Iron*	*S*	*Silicon*
G	*Magnesium*	*T*	*Tin*
H	*Thorium*	*W*	*Yttrium*
K	*Zircon*	*Y*	*Antimony*
L	*Lithium*	*Z*	*Zink*

Table 9.1: Designation of alloying elements [ASTM B2705-05]

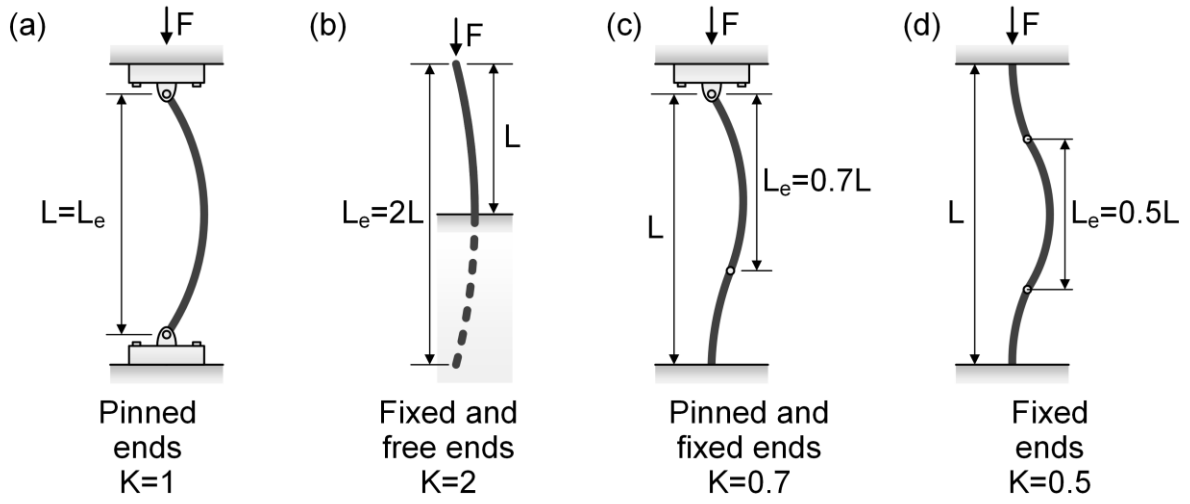

Figure 9.1: Effective length L_e of column in different Euler's buckling modes: (a) pinned ends (K=1), (b) fixed and free ends (K=2), (c) pinned and fixed ends (K=0.7), (d) fixed ends (K=0.5) [HIBB00]

Component	***Property***	***Value***	***Unit***
AZ31 Mg alloy	*Density*	*1.78*	*g/cm^3*
	Young's modulus at 20 °C	*44.7*	*GPa*
	Poisson's ratio	*0.29*	*-*
	Specific heat capacity	*1040*	*J/kgK*
	Thermal conductivity at 20 °C	*76.9*	*W/mK*
	Thermal expansion coefficient at 20 °C	*2,68*	*10^{-5} K^{-1}*
Insulation ceramic KV® 3 (heat protection plate)	*Density*	*2.0*	*g/cm^3*
	Young's modulus at 200 °C	*180*	*GPa*
	Poisson's ratio	*0.3*	*-*
	Specific heat capacity	*400*	*J/kgK*
	Thermal conductivity at 200 °C	*0.3*	*W/mK*
	Thermal expansion coefficient	*1.10*	*10^{-5} K^{-1}*
Cold work tool steel K890 MC (stamp)	*Density*	*7.85*	*g/cm^3*
	Young's modulus at 20 °C	*217.6*	*GPa*
	Poisson's ratio	*0.3*	*-*
	Specific heat capacity	*450*	*J/kgK*
	Thermal conductivity at 20 °C	*22.5*	*W/mK*
	Thermal expansion coefficient at 200 °C	*1.10*	*10^{-5} K^{-1}*
Cold work tool steel K390 MC (channel)	*Density*	*7.6*	*g/cm^3*
	Young's modulus at 20 °C	*217.6*	*GPa*
	Poisson's ratio	*0.3*	*-*
	Specific heat capacity	*450*	*J/kgK*
	Thermal conductivity at 20 °C	*21.5*	*W/mK*
	Thermal expansion coefficient at 200 °C	*1.07*	*10^{-5} K^{-1}*

Table 9.2: Physical properties of AZ31 sheet and tool materials for thermo-mechanical FE simulation

Determination of contact heat transfer coefficient

The heat transfer coefficient for the conduction between two materials is determined as follows:

$$h_C = \frac{1}{\frac{L_A}{\lambda_A} + \frac{L_B}{\lambda_B}} \tag{9.1}$$

where h_C is the overall heat transfer coefficient, L is the characteristic length and λ is the thermal conductivity.

Processing temperature [°C]	***Tensile direction***	***YS [MPa]***	***UTS [MPa]***	***ε_u [%]***	***ε_f [%]***	***r_{10} [-]***	***n [-]***
175	*RD*	*139*	*274*	*16.4*	*17.4*	*0.44*	*0.19*
	TD	*188*	*283*	*13.9*	*15.4*	*0.84*	*0.15*
200	*RD*	*143*	*271*	*18.4*	*23.3*	*0.56*	*0.21*
	TD	*185*	*280*	*15.4*	*21.8*	*1.36*	*0.15*
225	*RD*	*142*	*268*	*19.3*	*24.4*	*0.74*	*0.22*
	TD	*183*	*280*	*15.0*	*16.6*	*1.45*	*0.15*

Table 9.3: Influence of processing temperature on room temperature mechanical properties of ECAPed AZ31 sheets with Φ = 110°

Processing route	***Tensile direction***	***YS [MPa]***	***UTS [MPa]***	***ε_u [%]***	***ε_f [%]***	***r_{10} [-]***	***n [-]***
A	*RD*	*132*	*260*	*19.7*	*23.7*	*0.60*	*0.22*
	TD	*183*	*277*	*14.2*	*17.0*	*1.34*	*0.15*
C	*RD*	*140*	*265*	*20.1*	*24.1*	*0.69*	*0.24*
	TD	*184*	*277*	*14.2*	*17.4*	*1.26*	*0.15*
D	*RD*	*158*	*269*	*17.3*	*23.2*	*1.01*	*0.18*
	TD	*156*	*270*	*16.9*	*18.5*	*0.92*	*0.19*

Table 9.4: Influence of processing route on room temperature mechanical properties of ECAPed AZ31 sheets at 225 °C with Φ = 130°